UTC 2096-FR
24 September 1965

HEAT TRANSFER STUDIES OF SOLID ROCKET IGNITERS

Engineering Department
UNITED TECHNOLOGY CENTER
Division of United Aircraft Corporation
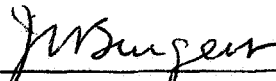Sunnyvale, California

Prepared for

National Aeronautics and Space Administration
Western Operations Office
Santa Monica, California
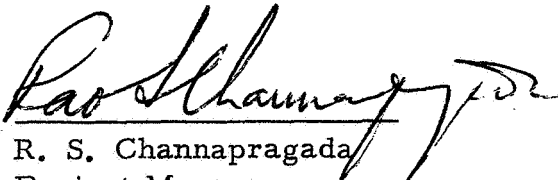Contract No. NAS 7-302

Report Submitted by:

B. J. Mullis (signature)

B. Mullis
Project Engineer

R. S. Channapragada (signature)

R. S. Channapragada
Project Manager

Report Approved by:

J. C. Burgess (signature)

J. C. Burgess
Branch Manager, Engineering
Sciences Branch

A. C. Keathley (signature)

A. C. Keathley
Manager, Engineering Department

X66 13240

FOREWORD

This is the final report on a study of heat transfer from solid rocket igniters conducted at United Technology Center (UTC) under Contract NAS 7-302. The work was administered through the Western Operations Office of the National Aeronautics and Space Administration with technical direction provided by Mr. Leon Strand of the Jet Propulsion Laboratory.

The work described in their report was conducted at UTC from July 1, 1964 through July 30, 1965. Mr. B. G. Mullis acted as project engineer and Dr. R. S. Channapragada as program manager. The effort was conducted under the supervision of Dr. J. C. Burgess, manager, Engineering Sciences Branch and Mr. A. C. Keathley, manager, Engineering Department.

SUMMARY

\13^{240}

Heat transfer from a solid-propellant igniter jet to a cold, nonreacting wall has been the subject of an experimental and theoretical study. The major emphasis in the program has been on obtaining experimental data for pyrogen igniters in several igniter configurations including both head-end and aft-end locations of the igniter. The effect of alumina in the exhaust stream was also experimentally studied. Measured values of total heat flux, radiant heat flux, and duct pressure are presented.

Correlation of convective data with a theoretical model has been successful for the head-end axial igniter in the region downstream of the impingement zone. Further analytical work is needed on the subjects of turbulent jet mixing and stagnation zone heat transfer in two-phase flow before correlation of the remainder of the data is attempted.

Trends in the radiation data are successfully predicted by an analytical evaluation of the duct emissivity. The magnitude of the radiation contribution does not match the data acquired. Some question exists regarding the validity of the magnitude of the radiation data. Some design improvements are contemplated for the radiation instrumentation prior to reuse in any future programs.

Author

CONTENTS

ILLUSTRATIONS

ILLUSTRATIONS (Continued)

ILLUSTRATIONS (Continued)

TABLES

SYMBOLS

M	Mach number
Nu	Nusselt number $= hD/k$
Pr	Prandtl number $= \dfrac{\mu C_p}{k}$
Re	Reynold's number $= \dfrac{GD}{\mu}$
St	Stanton number $= \dfrac{h}{C_p G}$
A	Cross-sectional area
C	Constant
D	Diameter
Fc	Radiation calorimeter calibration factor
G	Mass velocity $= \dot{w}/A$
G_n, $n = 0, 1, 2$	Constants in thermal entry length heat transfer solution
I	Image distance (schlieren system)
L	Object distance (schlieren system)
T	Temperature
X	Axial distance along duct measured from igniter exit plane
c_p	Specific heat at constant pressure
f	Focal length (schlieren mirrors)
h	Convective heat transfer coefficient
k	Thermal conductivity

l	Thickness
m	Mass of radiation calorimeter slug
p	Pressure
q	Heat flux
r	Radius
t	Time
$\dot{w}$	Mass flow rate
x	Axial distance along duct measured from end of duct
x'	Axial distance along duct measured from igniter jet impingement point
x''	Axial distance along duct measured from igniter jet exit plane
x^+	Nondimensional length

GREEK SYMBOLS

α	Thermal diffusivity
γ	Ratio of specific heats
ϵ	Emissivity
λ	Wavelength
λ_n	Eigen values in thermal entry length heat transfer solution
μ	Viscosity
ρ	Density

SUBSCRIPTS

aw	Adiabatic wall conditions
b	Bulk or stream conditions
c	Chamber conditions
e	Nozzle exit plane
ign	Conditions in the igniter or igniter exit
m	Average
rad	Due to radiation
w	Wall conditions
x	Conditions at axial location x (e. g. , Nu_x)
∞	Conditions at infinity (e. g. , Nu_∞)
o	Initial conditions
1, 2, . . .	Conditions at times t_1 , t_2 , . . .

1.0 INTRODUCTION AND BACKGROUND

Ignition of solid rocket motors is attained by conventional pyrotechnic igniters through heat transfer to the propellant surface by a variety of mechanisms. The combined heat transfer mechanisms raise the surface temperature of the propellant to its autoignition temperature where stable combustion can be sustained.

The ignition transient of a solid-propellant motor can be divided into three phases. The first phase of the ignition process consists of the igniter providing energy to the propellant surface in order to attain the autoignition temperature at some region of maximum heat transfer on the propellant surface. The initiation of combustion occurs when the autoignition temperature is reached and the first phase of the ignition process is completed. The time delay of the hypergolic ignition process is a function of the frequency factor and activation energy of the hypergolic reaction, the concentration of hypergolic oxidizer, and the propellant ignition temperature. For pyrotechnic igniters the first phase is controlled by the temperature and heat transfer characteristics of the environment.

In the second phase, the heating of the unignited portion of the propellant surface continues, promoting ignition of the remaining propellant surface and thereby propagating the flame front to the unignited area. The time delay in the second phase before the entire surface is ignited is determined by the heat transfer from the hot combustion products flowing across the unignited propellant surface, coupled with hypergolic heating by direct surface reaction. During this period, the mass discharge rate through the motor nozzle increases as the flame spreads over the propellant causing a rise in chamber pressure. The initiation of combustion over the entire propellant surface defines the completion of the second phase (as shown in figure 1). During the third phase the combustion products continue to fill the motor chamber until a steady-state pressure has been reached. The chamber pressure transients of the third phase have been described by Barrer et al.[1]*

The above three phases coupled together define the overall ignition process in a solid rocket motor.

---

* Superscript numbers denote references appearing on page 67.

DESIGN CHAMBER PRESSURE

ENTIRE SURFACE IGNITED

FIRST INDICATION OF
PROPELLANT RESPONSE

CHAMBER PRESSURE
DUE TO IGNITER

INITIATION

PRESSURE

PHASE I

PHASE II

PHASE III
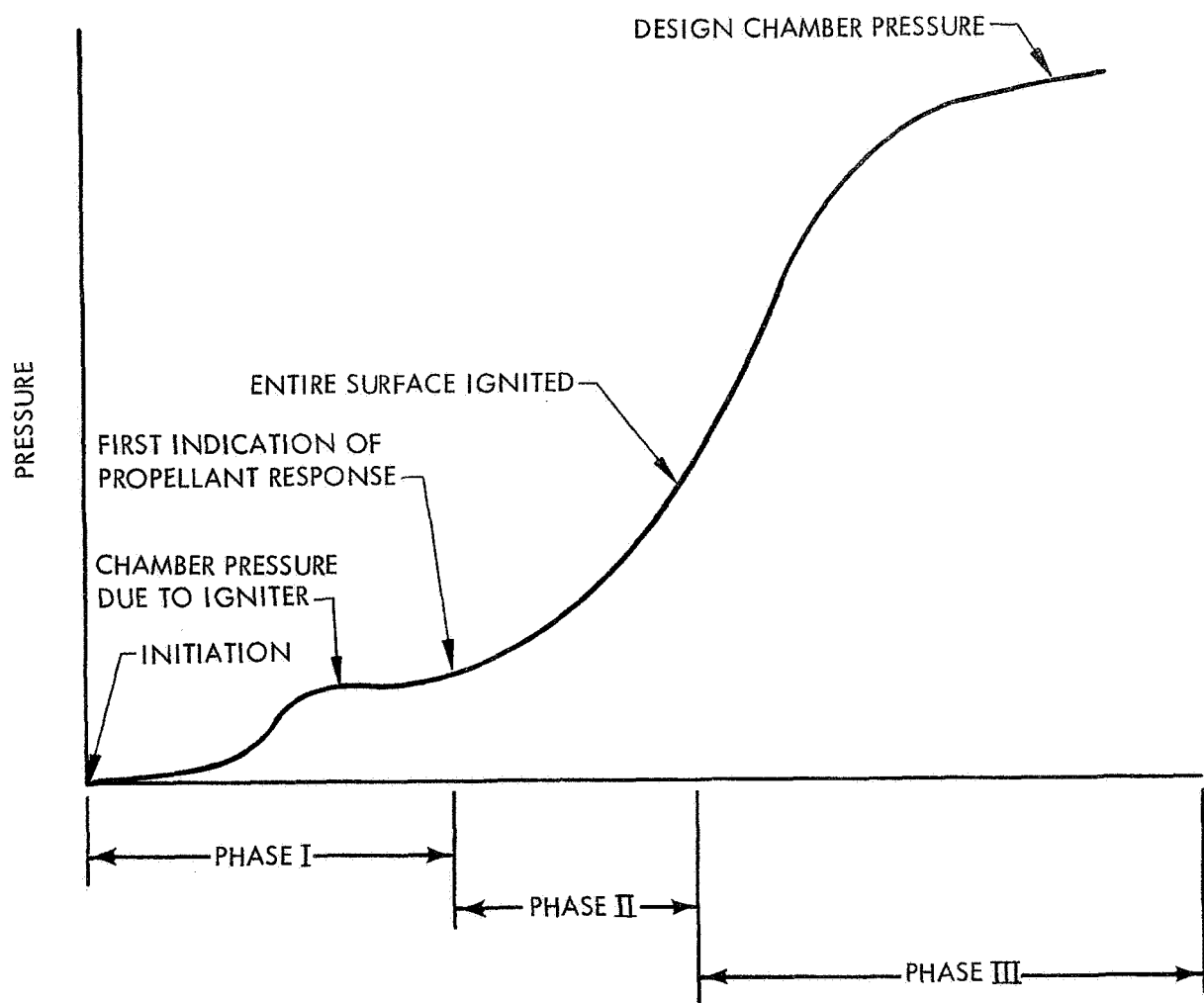
R-30968

Figure 1. Schematic Diagram of Chamber Pressure Transient
During Ignition

Recent work at United Technology Center (UTC) has been directed toward describing the basic hypergolic ignition process under nonflow conditions.[2,3]

Other studies by Anderson et al.[4] and Bear and Ryan[5] have been concerned with conditions defining the autoignition temperature of the propellant. The surface ignition temperature concept, as demonstrated by the above investigators, is a function of the heat flux and the ambient propellant temperature during studies of ignition of composite solid propellants at low flux levels.

Current studies in progress at UTC under NASA Contract NAS 7-329[6] have been devoted to the study of ignition propagation defined by the second phase.

The preignition or thermal induction period, defined as the first phase, is one of the most complex processes involved in the combustion of solid-propellant rocket motors. The ignition delay is a function of the autoignition temperature of the propellant and the gas dynamic heat transfer characteristics of the igniter exhaust impinging on the surface of the propellant.

Ducted igniter jet impingement heat transfer phenomena are analogous to the separated flow phenomena over a cavity or a step. In the case of igniter heat transfer, the problem of a sonic or supersonic jet issuing over a step or cavity is compounded by the addition of two-phase and ducted flow.

In view of the complexity of the several processes occurring simultaneously in the preignition phase, it is logical to gain an insight into the various heat transfer mechanisms separately. With a rational approach to the igniter design criteria of solid rocket propellants as a final objective, an experimental and theoretical study was conducted under Contract NAS 7-302 issued by NASA Western Operations.

The program was specifically directed toward establishing the region of maximum heat transfer and the parameters controlling the heat transfer rate in the preignition phase as delineated in the text of the final report.

3

2.0 TECHNICAL DISCUSSION

2.1 GENERAL

The ignition process of solid rocket motors by conventional pyrotechnic igniters is largely dependent on the modes of heat transfer and the detailed composition of igniter exhaust gases and the igniting atmosphere.

Analytical studies conducted at UTC have provided a heat transfer model of motor ignition that predicts the igniter flow rate requirements for a given lag time for rocket exhaust type igniters.[7] The lag time increment is the time from the start of igniter flow in the main motor chamber to the first indication of propellant burning in the main motor. This propellant ignition lag time is the most important variable available to the engineer for designing rocket-type igniters.

The main motor propellant is assumed to begin ignition in the region of highest heat transfer. The adiabatic wall temperature in this region is not accurately known but can be expressed as T_{aw} which has an upper limit approaching the stagnation temperature of the igniter gases. It will be assumed for the region behind the shock wave that the igniter flow rate and stream temperature are constant during the lag time period. This assumption is supported by evidence that the igniter chamber pressure rises rapidly (igniter flow rate is proportional to igniter chamber pressure), and almost all of the igniter flow crosses the shock wave area, as the storage volume ahead of the shock wave is small.

To solve for the lag time, it is necessary to consider the temperature-time history of the main motor propellant surface immediately behind the shock region. Figure 2 schematically illustrates the temperature-time history of the propellant surface immediately at the location of maximum heat transfer. Two phases or periods are readily defined: the period t_0 to t_1 when external sources are heating the propellant, and the period t_1 to t_2 when propellant chemical reaction is predominant.

Referring to figure 2, the assumption will be made that $t_2 - t_1 = 0$. Hence, the chemical reaction may be ignored and the actual ignition temperature can be replaced by T_i. It is experimentally observed that $t_2 - t_1$ is very small compared to $t_1 - t_0$. For most solid propellants, the ignition process may be described analytically by external heating rather than by propellant decomposition. Thus, the problem is reduced to determining
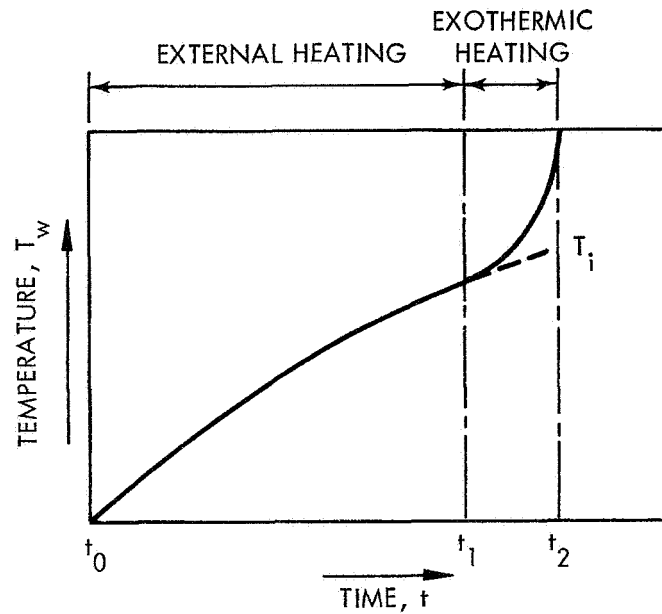
R-51408

Figure 2. Temperature-Time History of Propellant Surfaces

the time required to heat the main motor propellant from external heat sources to the temperature where spontaneous ignition occurs.

The differential equation for one-dimensional heat loss by conduction in the solid propellant is:

$$\frac{1}{\alpha} \frac{\partial T}{\partial t} = \frac{\partial^2 T}{\partial r^2}$$

where α is the propellant thermal diffusivity. Assuming T_{aw} = constant, $T_{aw} \gg T_w$. Thus, $q_{total\ in}$ is constant and the solution of this equation at $r = 0$ is given by:

$$T_w - T_o = \frac{2\ q_{total\ in}}{k} \left(\frac{\alpha t}{\pi} \right)^{\frac{1}{2}}$$

where k is the propellant thermal conductivity and T_o is the initial propellant surface temperature. By rearrangement:

$$t = \left(\frac{T_w - T_o}{2} \right)^2 \frac{k^2 \pi}{d\ q_{total\ in}^2} .$$

5

The solution yields the propellant surface temperature as a function of time during the transient period. The strong dependence of the ignition lag on the quantity q_{total} in makes an accurate knowledge of the heat flux mandatory for the designer to predict the ignition transient of a solid rocket motor. It is the purpose of this study to provide experimental heat transfer data for several igniter configurations.

2.2 PROBLEM AREAS REQUIRING INVESTIGATION

In determining the design requirements for a rocket-type igniter, the designer must predict the combustion chamber pressure transient. Since the entire propellant surface is not ignited simultaneously, determinations of the flow pattern and the heat transfer coefficient are interrelated. For example, the heat transfer is a function of the flow pattern, which is, in turn, a function of propellant ignition. The principal parameters controlling the ignition delay and propagation are:

A. Mass flux from the igniter

B. Composition and thermal properties of exhaust products flowing through the duct

C. Pressure ratio of the igniter exhaust

D. Motor port geometry.

In the present program two basic methods of hot-gas ignition, head-end ignition and aft-end ignition, are being investigated.

2.3 HEAD-END IGNITION

The forward rocket igniter is mounted on the forward closure and becomes a part of the mission. The propellant ignition process for the forward-mounted igniter generally may be characterized as described below.

Current designs of forward-end rocket igniters include three orifices oriented at an angle of 30° with the motor centerline so that the hot igniter gases expand from sonic orifices to a supersonic jet and impinge on the propellant surface near the forward end of the motor. The gases then go through a series of shocks, and a subsonic flow regime is established. Quasi-steady flow from the igniter is established immediately. The motor chamber is pressurized and heat is transferred to the propellant by radiation and convection until ignition takes place.

The point at which ignition initially occurs is a function of the heat transfer rate. According to the ignition lag theory described in the technical discussion a definite heat transfer rate is required to minimize ignition delay, indicating that rates can be too high and the fuel pyrolized.

2.4 AFT-END IGNITION

The aft-end ignition system is mounted on the launch pad directly below and independent of the motor. A single nozzle with a full expanding exit cone directs the hot igniter gases into the main motor chamber. The propellant ignition process for the pad mounted igniter (concluded from experimental data) may be generally characterized as described below.

The igniter gases enter the chamber by passing through the motor nozzle. As these gases flow through the port, the original air in the chamber is compressed until an equilibrium is reached between the stagnation pressure of the igniter gases and the pressure of the entrapped air. At this point, the igniter gases stagnate at a location depending on the mass and velocity of the hot gases. Quasi-steady flow conditions are established and the propellant surface is heated. When optimum heat for ignition has been transferred, inception of ignition occurs somewhere near the igniter, and the flame propagates rapidly up the port to the stagnation area. A chamber pressure proportional to the fractional burning surface area is established. At this point, the movement of the flame front is retarded while heat is transferred to the unignited propellant forward of the stagnation zone. Upon sufficient transfer of heat to the propellant surface, the flame front propagates rapidly over the remaining port surface until complete ignition is achieved.

2.5 TECHNICAL DISCUSSION SUMMARY

The determination of heating rates for head-end and aft-end ignition can be obtained as a function of position along the grain. This will facilitate prediction of the magnitude of heat flux for minimum ignition delay. Since the present experimental program uses identical grain-port dimensions and hot-gas characteristics as the above mentioned experimental tests, heat transfer rates should be identical (except for some adjustments for nonadiabatic effects in the copper tube).

A comparative study of ignition, ignition propagation, and design of head-end and aft-end ignition as a function of the flow properties is to be investigated.

To adequately define the ignition process, it is necessary to be able to completely characterize the flow field and heat transfer in ducted jets. Hence, an attempt has been made to conduct parallel experimental and theoretical programs to provide this fundamental knowledge on ducted jet mixing and heat transfer. The emphasis of this program has been on the following areas:

A. Measurement of static pressure in ducted jets

B. Measurement of local wall heat transfer coefficients along the duct

C. Measurement of radiative properties of ducted jets

D. Visualization of the flow and boundary layer development (nonreacting and reacting mixing fields) as described in the program plan.

3.0 APPARATUS AND INSTRUMENTATION

3.1 FLOW VISUALIZATION APPARATUS

A flow visualization apparatus was constructed to provide a means of visually observing the igniter jet plumes. This apparatus provides a tool to study the gas dynamics of the igniter jets to determine the shock locations and impingement points for typical configurations.

The duct configuration is shown in figure 3. This duct is designed such that two opposite sides hold 1/2-in.-thick quartz windows while the top and bottom surfaces are machined to hold inert propellant slabs, live propellant slabs, or a heat transfer surface. The inert propellant slabs are used to make approximate measurements of propellant erosion and to determine the extent of the propellant thermal decomposition under the action of the various igniters. A copper heat transfer surface was constructed to provide surface heat transfer data in a small-scale motor. The heat transfer surface is a 0.045-in. plate of pure copper, drilled to accept 30-gauge copper-constantan thermocouple junctions at the locations shown in figure 4. The thermocouple leads are peened into the plate. Not all of the thermocouples were read out because the data acquisition system is limited by galvanometer availability to 26 channels. Initially the visualizer duct had been drilled for a pressure reading at the exhaust end. After the test program had begun a head-end or "base" pressure reading was required and the duct was modified for this measurement.

One end of the duct is machined to accept a micromotor igniter (figure 3). Two nozzle configurations, modeling two typical igniter configurations, were tested in the micromotors. Shown in figure 3 is the two-port nozzle in which the ports are canted 30° from the duct axis. Also tested was an axial flow nozzle. All nozzles used in the flow visualization tests have sonic velocity at their exit plane. The nozzles and propellant samples are designed to maintain a 2000-psi chamber pressure. Both aluminized and nonaluminized micromotor propellants were used.

Cold-flow tests using nitrogen as the "igniter gas" were conducted to get some idea of shock locations, impingement points, and other flow characteristics. In these tests the gas is ducted through the micromotors into the visualizer chamber.
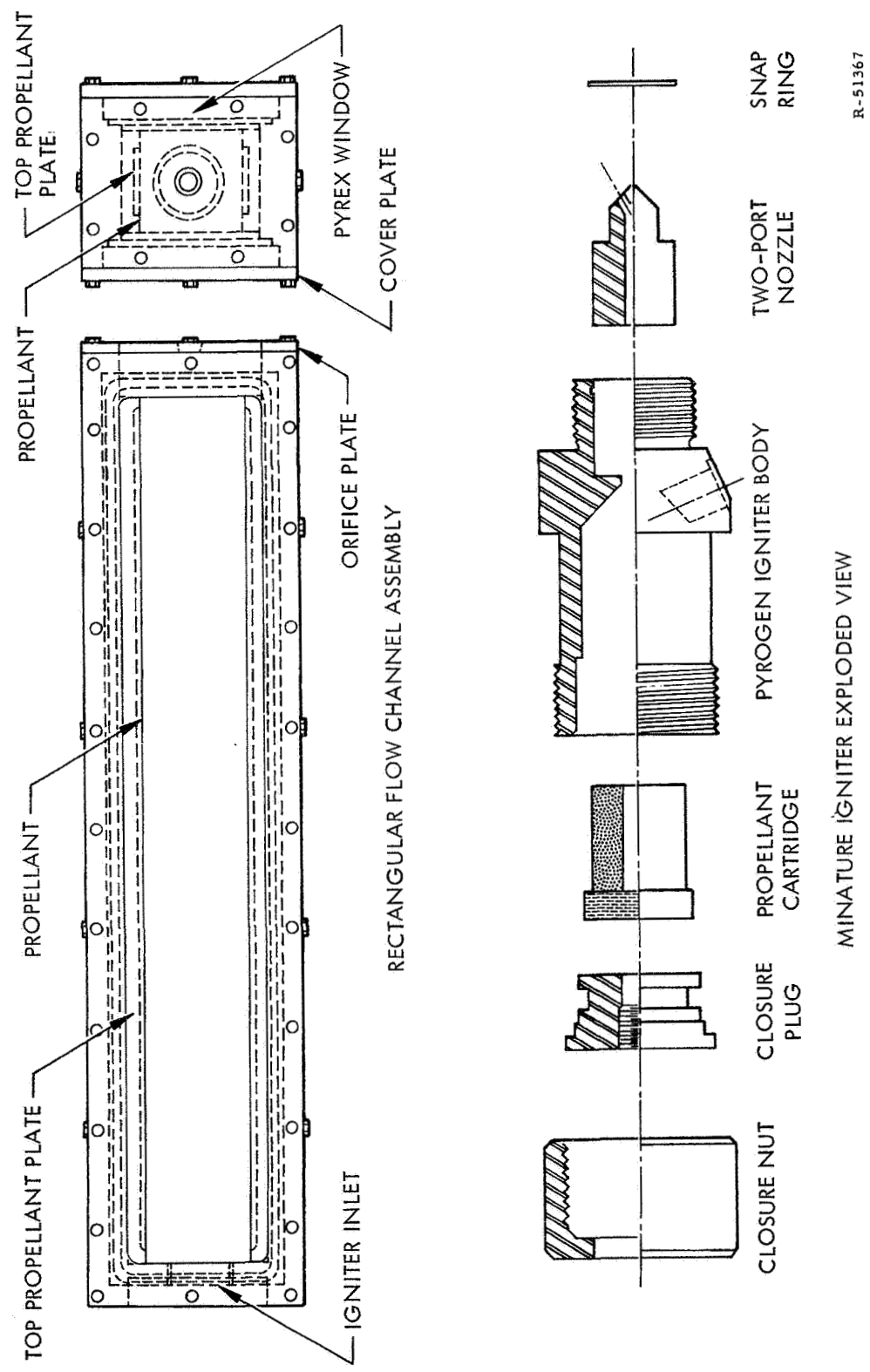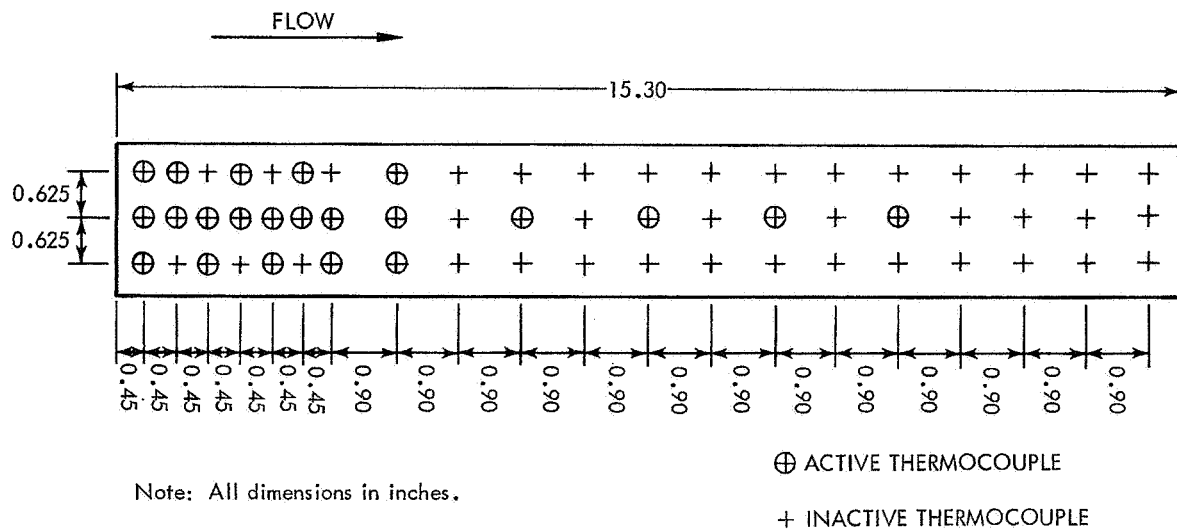
Figure 3. Flow Visualization Apparatus

R-51367

Figure 4. Thermocouple Locations in Copper Plate
Flow Visualizer Test

A schlieren system was purchased for this phase of the project and
set up for use as shown in figure 5. Two 12-in. parabolic mirrors having
a 60-in. focal length are mounted on tool stands. The light source is sup-
plied by a high-voltage xenon arc lamp. The transparent duct is placed
between the mirrors at a point such that the camera box, specially con-
structed for this project, can be placed to provide a large, sharply focused
image of the nozzle at the film plane. The shutter on the camera box is
set for 1/25 sec for all runs. Actuation of the shutter closes a set of con-
tacts which cause the xenon lamp to fire. In the cold-flow tests, the shutter
is operated by hand. In the hot-flow tests, the shutter is operated by a
pressure switch connected to the micromotor chamber. For most tests
a polaroid film was used. Very clear photos were obtained during the
cold-flow tests. Photos were also taken during the hot-gas tests, but they
are not as good due to clouding of the windows by soot and opacity and
radiance of the ducted gases.

Color motion pictures were taken of each of the miniature hot firings.
For the first hot firing the only available camera was limited to 64 frames/sec.
Movies of later firings produced better results due to higher frame rates
of 500 to 1000 frames/sec. Frames from the films of the axial igniter
firings using aluminized and nonaluminized propellants are shown in
figure 6.

CAMERA BOX LENGTH (l) IS ADJUSTABLE SUCH

THAT $1/f + 1/L = 1/l$ FOR PROPER FOCUS

AND IMAGE SIZE.

KNIFE EDGE

MIRROR

R-51324

FILM PLANE

CAMERA

MOVIE CAMERA

IGNITER AND
DUCT MODEL

ARC LAMP
LIGHT SOURCE

MIRROR
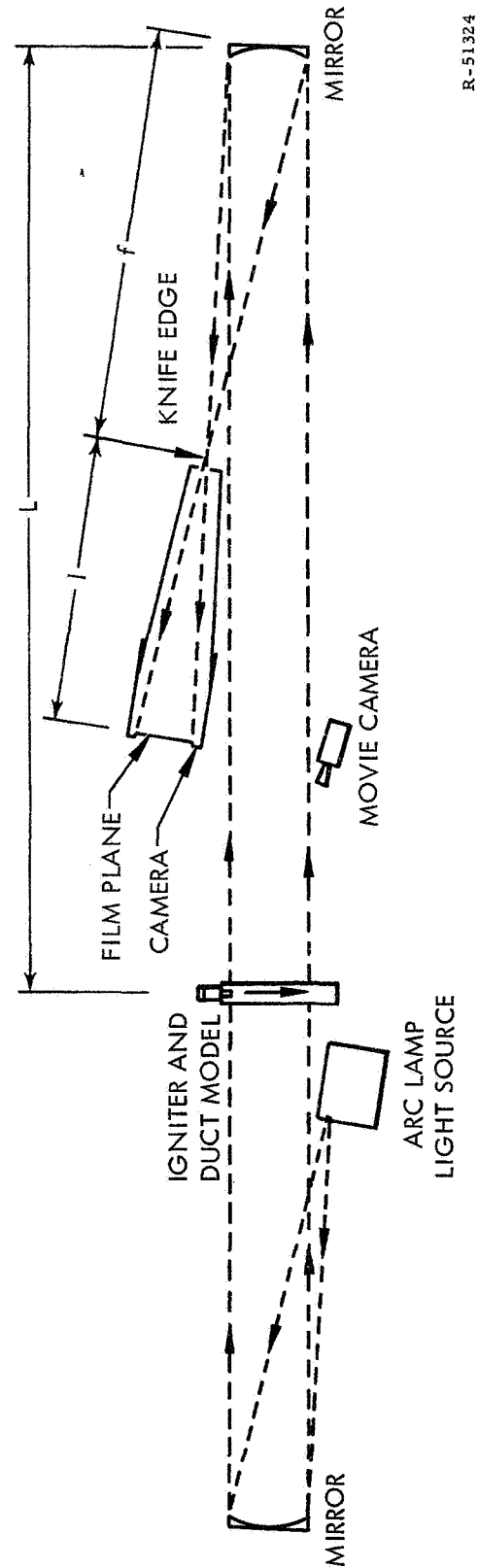
Figure 5.   Schlieren System Diagram
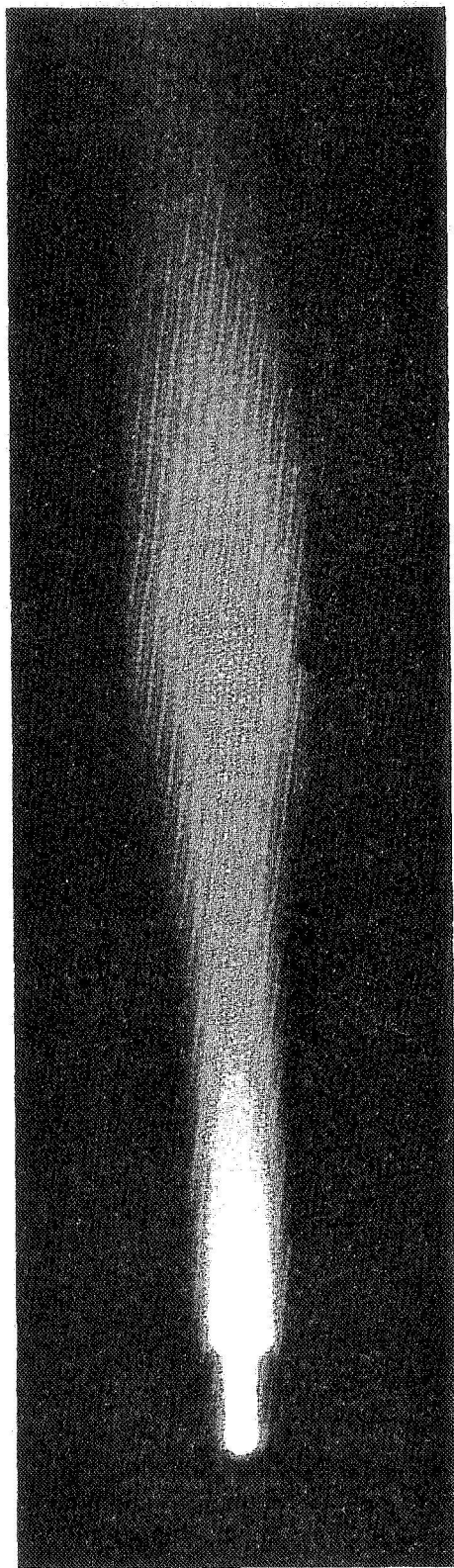
R-51402

A. Flow visualizer movie axial nozzle, nonaluminized propellant.

B. Flow visualizer movie axial nozzle, aluminized propellant.

Figure 6. Flow Visualizer: Axial Nozzle, Aluminized Propellant

The data produced by the copper plate thermocouples and the pressure transducers were recorded on two 18-channel CEC oscillograph recorders.

3.2 COPPER TUBE APPARATUS

An 8-in.-diameter, 96-in.-long pure copper duct with a 0.125-in. wall was purchased for use as a heat transfer model of a typical solid-propellant motor grain surface prior to ignition. This configuration was chosen because it is geometrically identical to the standard two-segment TM-3 (UTC test motor designation), and neither the design of basic igniter hardware nor ignition pyrotechnics had to be repeated. The duct is solidly clamped into the test stand as shown in figure 7. The igniter may be mounted either at the closed or open end of the copper duct to simulate head-end or aft-end ignition configurations. The igniter nozzles are sized to maintain a n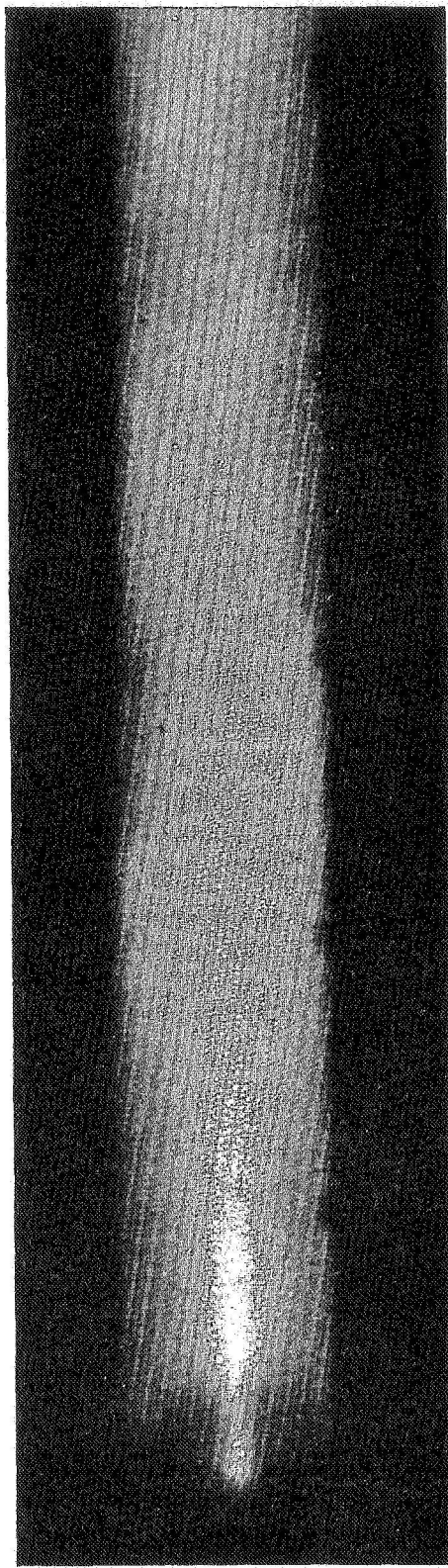ominal igniter pressure of 1000 psi for all copper duct tests. The head-end axial igniter has three available nozzle inserts to accomodate three flow rates. None of the axial head-end igniters used expansion cones. The axial head-end igniter configuration is shown in figure 8A.

For the head-end configuration the multiple-port igniter may be fitted with any of three sets of nozzles to accommodate three mass flow rates. The multiple port igniter configuration is shown in figure 8B. None of these nozzles has an expansion cone.

The aft-end igniter can be placed at the duct exit or partially inserted into the duct as shown in figure 9. Almost any nozzle expansion ratio can be accommodated, but only near optimum expansion and unexpanded (sonic) conditions were tested. Three sizes of aft igniter nozzles are available to provide three igniter flow rates. Orifice plates were attached to the open end of the copper duct to maintain the desired duct pressure for a study of the heat transfer mechanisms. Several tests were conducted with the igniter inserted approximately 10-1/2 in. into the duct. In these runs the duct pressure was regulated by adjusting the gap between the igniter and the duct end flanges. Photographs of the igniter in the aft end of the duct are shown in figures 7 and 10.

Batches of aluminized and nonaluminized propellant were mixed and cast into phenolic sleeves designed to fit into the igniter cases. The minimum propellant thickness which can be cast is about 0.4 in. The use of this propellant "web" thickness results in an igniter burning time of about 600 msec. This duration is much greater than is needed for a determination of the wall heat transfer. In addition, preliminary results from the copper plate measurements in the flow visualizer apparatus indicated that the melting temperature of the copper duct would be approached at the
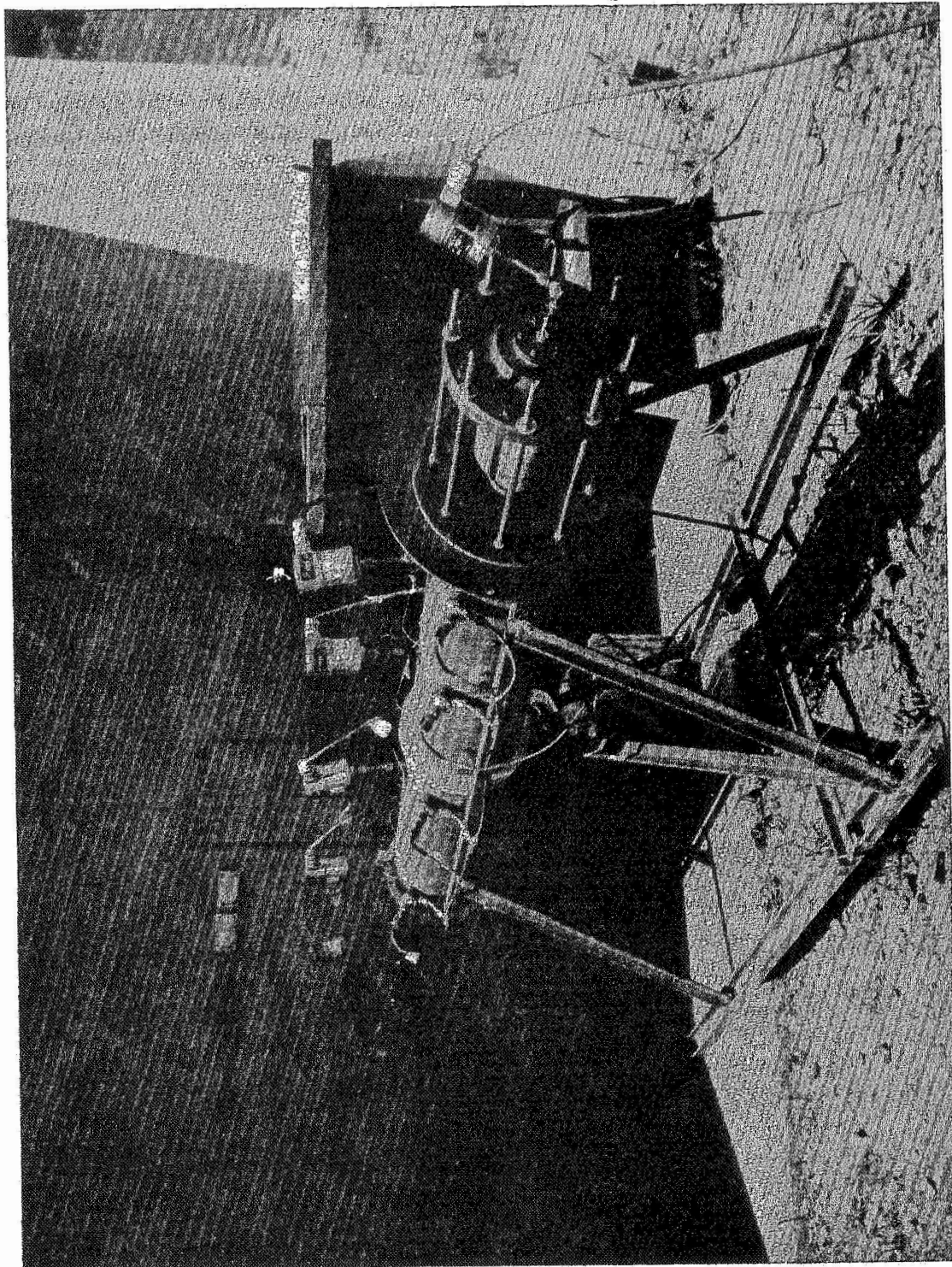
Figure 7. Copper Duct Apparatus

ELECTRIC IGNITION SQUIB

AXIAL JET
IGNITER

THERMOCOUPLE LOCATIONS

IGNITER PROPELLANT (0.2-IN. WEB)

COPPER DUCT

30°

120°

BPN PELLET BASKET

10 IN.

CANTED JET IGNITER
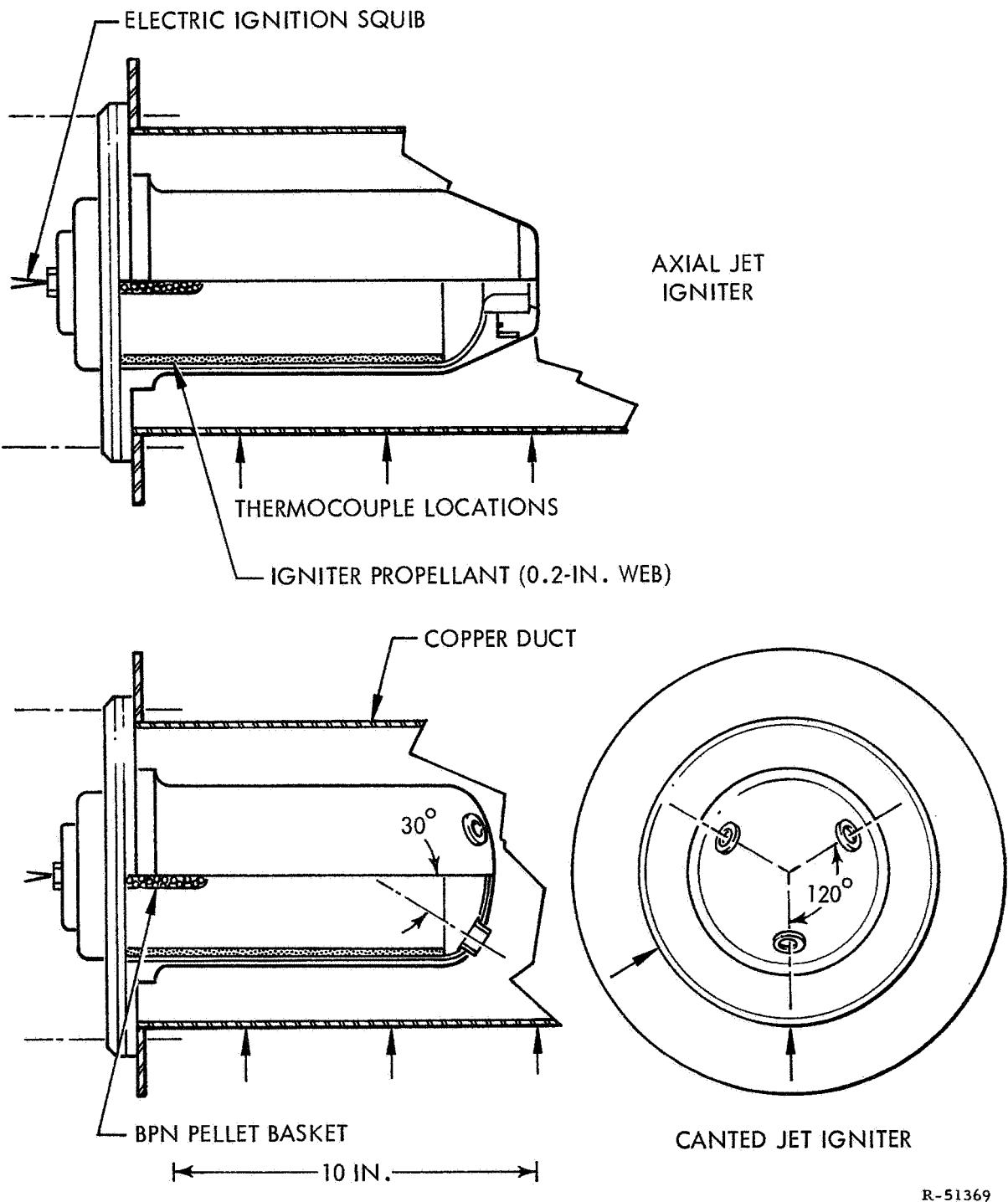
R-51369

Figure 8.   Head-End Igniter Configurations

NOZZLES WITH
1.0 AND 5.5 EXPAN-
SION RATIOS TESTED

0.50 IN., RUN 20 - 25 } GAP ADJUSTABLE FOR
0.70 IN., RUN 26 - 30 } DUCT PRESSURE CONTROL

93 IN.

10 IN.
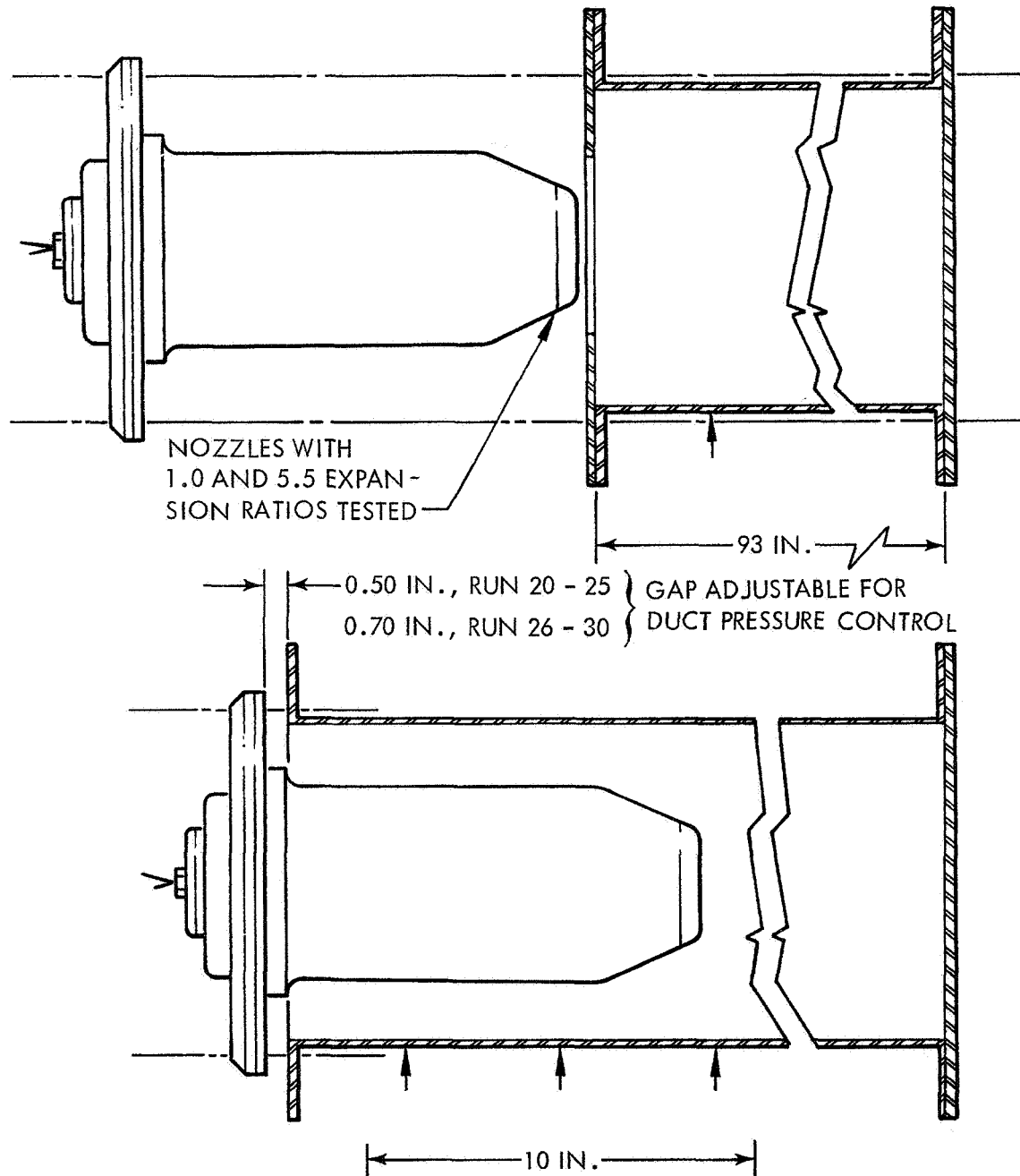
R-51360

Figure 9. Aft-End Igniter Configurations

17

Figure 10. Aft Igniter Installed in Copper Duct

igniter jet impingement points if this duration were used. The web thickness, therefore, was trimmed to about 0.20 in. in all motors, resulting in an acceptable igniter duration of about 300 msec. Equilibrium thermochemical calculations indicate that the temperature of the combustion products in the chamber will be about 4760° F for the nonaluminized propellant and about 5500° F for the aluminized propellant (18.5 moles of Al_2O_3 per 100 g of propellant in the chamber.)

After the runs using aluminized igniter propellant, the duct was observed to be coated with a frozen film of Al_2O_3 and the film was found to be heaviest in the vicinity of the jet impingement areas. It was easily removed with emery paper and the surface in the vicinity of the thermocouple instrumentation was carefully cleaned prior to each run.

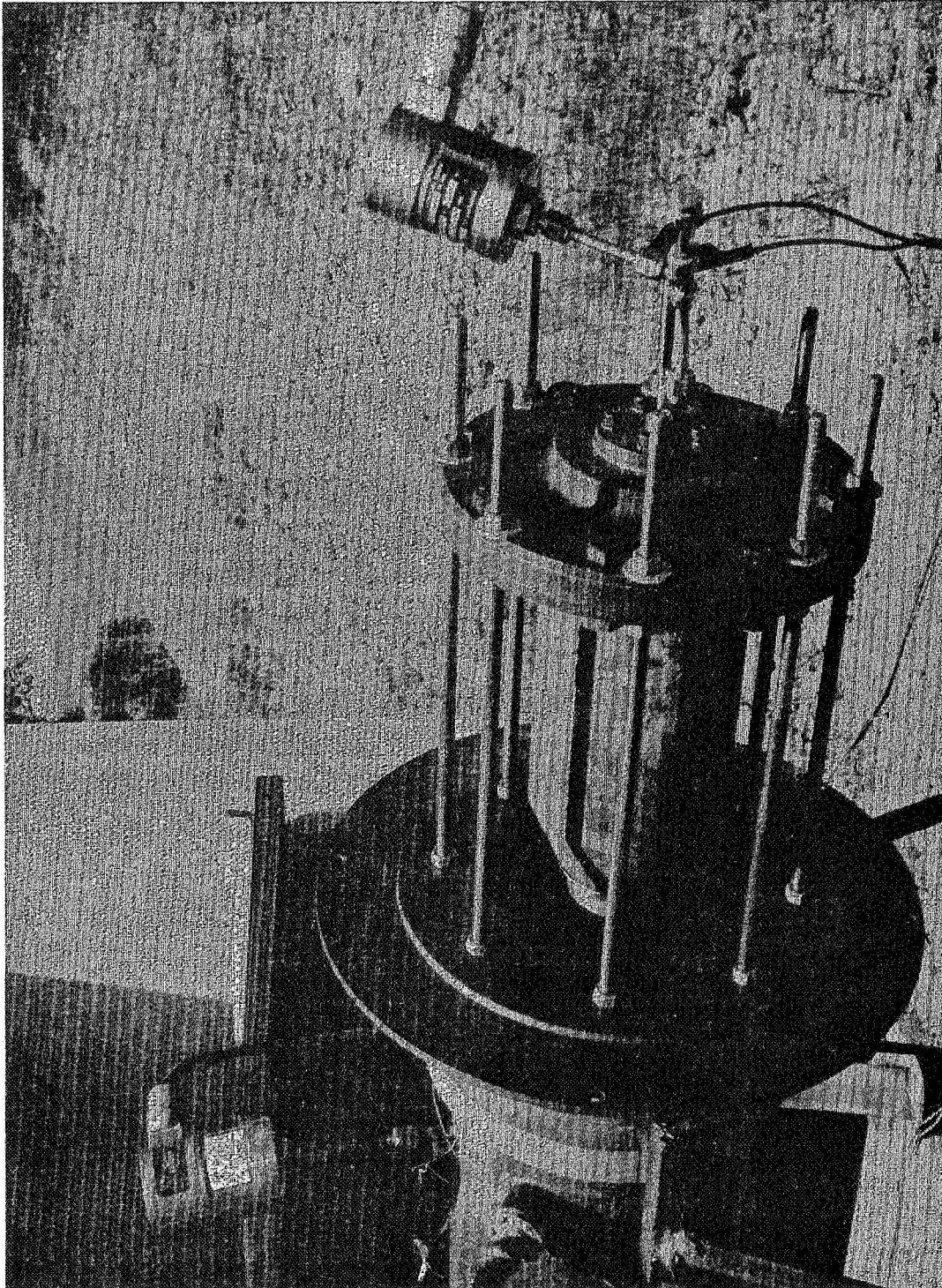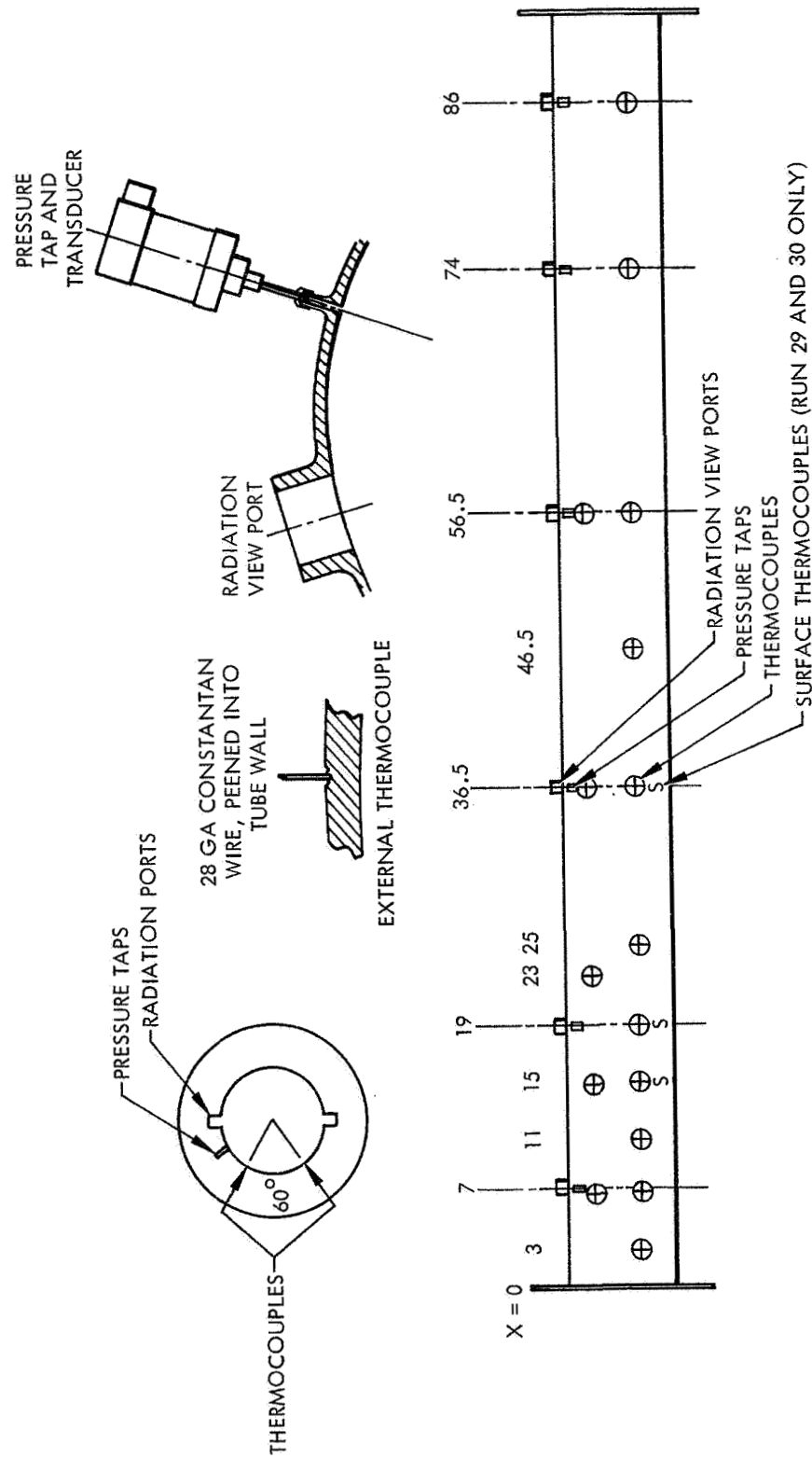The copper tube is instrumented to provide data on the spatial and time variation of total heat transfer, radiant heat transfer, and duct static pressure as shown in figure 11. Most of the total heat transfer data are obtained through the use of thermocouples peened into the outside surface of the duct. The junction of a constantan wire with the pure copper duct forms the thermocouple. The igniter duration is sufficiently short that errors produced by conduction away from the thermocouple junctions are not over 4%. (See appendix A.) Most of the data have roughly a 1% error due to conduction. Periodically the peened junctions were checked for electrical continuity and were always found to be intact. The constantan wires are bundled together and led away from the copper tube to an insulated reference junction box. Prior to each run, the temperature of the reference junction box was recorded.

Accurate determination of the transient heat transfer during igniter start-up requires an instrument with faster response and higher sensitivity than the "backside" thermocouple. Considerable time and effort were expended in the program to design and produce an instrument which was capable of accurately measuring the desired transient and yet could withstand repeated uses in the severe duct environment without major repairs. It is believed that the nickel-plated copper slug thermocouple[8] will provide such a measurement. Several attempts to manufacture this type of instrument were made, but no successful units were produced. The silicone monoxide insulator coating which is required over most of the copper slug surface must be deposited in its vapor state. Good high-vacuum equipment is available at UTC, but the technical problems of mounting and turning the slug and properly heating the silicone monoxide to its melting point were not solved. The apparatus suggested in texts on the subject was duplicated and tried, as well as new ideas. Although the units finally produced are much better in insulator uniformity and adhesion than the earlier units, the process still requires some improvement before the

Figure 11. Copper Tube Instrumentation

NOTE: Positions expressed in inches from end of tube.

nickel plating can be applied. To provide a rough check on the ability of the backside thermocouples to produce usable information about the transient heating, three internal-surface thermocouples were made which employed the simplified design shown in figure 12. Time limitations require that the analysis of this data be postponed until the start of the follow-on work.

The radiation heat flux calorimeters shown in figure 13 were developed at UTC. These instruments consist of a copper slug sensing element which has a thermocouple soldered onto the backside. The sensing element is approximately 0.020 in. thick and has a diameter of 0.35 in.

The thermocouple is a junction of 40-gauge chromel and constantan wire. The junction is silver soldered onto the back of the copper sensing element. Accurate measurements (four significant digits) of the mass of the slug, wire, and solder were made so that the proper heat capacity could be calculated for the finished slug. The slug is mounted in an aluminum holder and the thermocouple wires are led out to a standard two-wire electrical cannon connector. The surface of the copper slug is blackened with a very thin coating of flat black paint to minimize the reflectivity. By comparing the results of calibration runs using HyCal gages and UTC gages with no quartz windows installed, it is found that the UTC gage sensing element has an approximate 0.84 to 0.85 surface absorptivity.
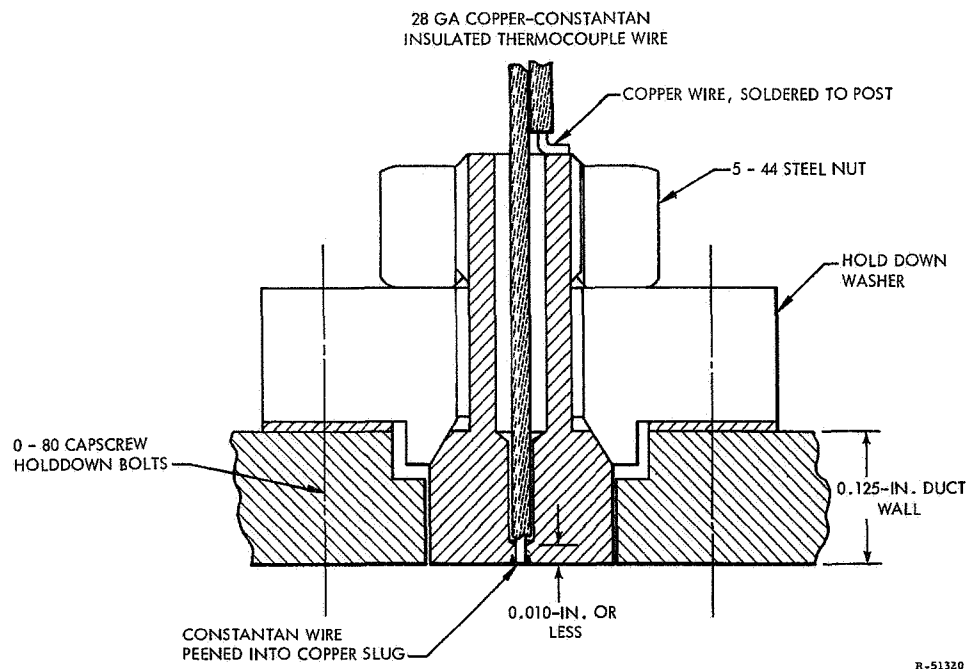

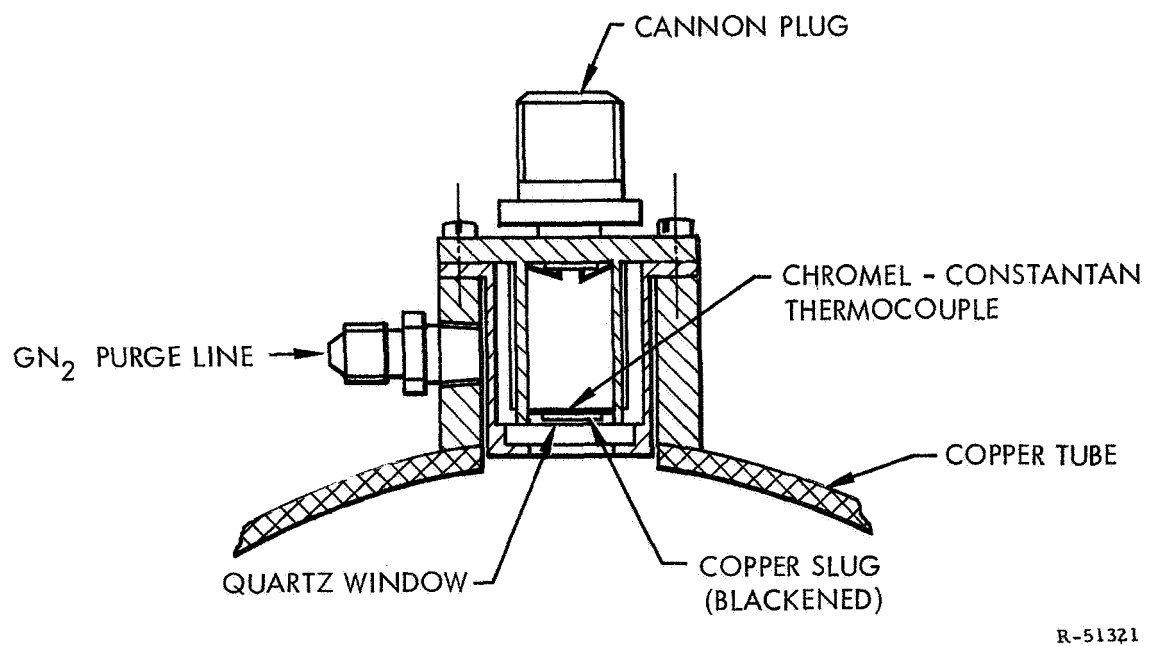Figure 12. Copper Constantan Internal-Surface Thermocouple

Figure 13. United Technology Center's Radiation Calorimeter

The holder is inserted into an aluminum case which contains an O-ring sealed quartz window approximately 0.10 in. thick. The sensing element is positioned within approximately 0.005 in. of the quartz window. The quartz window transmits approximately 90% of the incident radiant energy within the band 0.4 to 2.2μ. In other work at UTC,[9] it is shown that rocket exhaust clouds have a spectral radiation intensity distribution similar to that of a gray body. Therefore, the wavelength of peak radiation intensity may be calculated from classical thermal radiation relationships.

Hence, for gas clouds at 5960° R and 5220° R, one obtains peak radiation intensity at wavelengths of about 0.8 and 1.0 μ for the aluminized and nonaluminized propellants, respectively. This is well within the band of peak transmissivity of the quartz windows and it is concluded that not more than about 10% of the incident radiation is lost due to the absorptance and reflectance of the quartz windows. The radiometers are calibrated prior to the runs by comparing the heat absorption rate of the radiometers to that of the more sensitive (but more delicate) HyCal gage under the same incident radiation. By appropriate correction to the HyCal gage readings, the incident heat flux calibration for the UTC radiometers is obtained. More details of the calibration method are given in reference 10. The resulting calibration factors are shown in table I.

TABLE I

UTC RADIATION CALORIMETERS: HEAT CAPACITY
AND CORRECTION FACTOR

UTC Gage Serial No.	$\dfrac{mC_p}{A}$ $Btu/in^2 - °F$	$\dfrac{1}{F_c \cdot \epsilon_{HyCal}}$
1	6.85×10^{-4}	1.48
2	6.79	1.59
3	6.78	1.55
4	6.60	1.47
5	6.66	1.41
6.	6.56	1.47
7	6.77	1.54
8	6.70	1.46
9	6.71	1.44
10	6.64	1.51
11	6.59	1.39
12	6.64×10^{-4}	1.42

During the last stages of the experimental program, eight firings were made using a spectral radiometer sighted into one viewport to sense the radiant intensity at several wavelengths. The apparatus is capable of taking 16 samples during 1/3 sec and, therefore, is capable of obtaining several readings during the 300-msec igniter firing duration. The data obtained appear to be usable but a black body calibration of the apparatus, in which the window and positioning are reproduced, must be accomplished before the data are reduced. It is intended that this calibration be undertaken during a follow-on to the present contract. Further use of the radiometer will require that the duct viewports be enlarged so that larger windows may be installed. This is required since the radiometer is at the limit of its capability with the 1/2-in.-diameter window.

An electrical calibration of the recording circuit for every channel is made prior to each run. A sample thermocouple circuit is shown in figure 14. With the calibration switch in the down position, the galvanometer is subjected only to the output from the thermocouple. With the switch in the up position (shown), the thermocouple is taken out of the recording circuit and the calibration circuit is substituted. Measurement of the calibration voltage is made with a potentiometer capable of reading to within 0.001 mv. Two steps in calibration voltage were made prior to each run by varying the 0- to 1000-ohm helipot setting.

Most of the flow visualizer runs and all of the copper duct runs were conducted at the Development Center at Coyote, California.
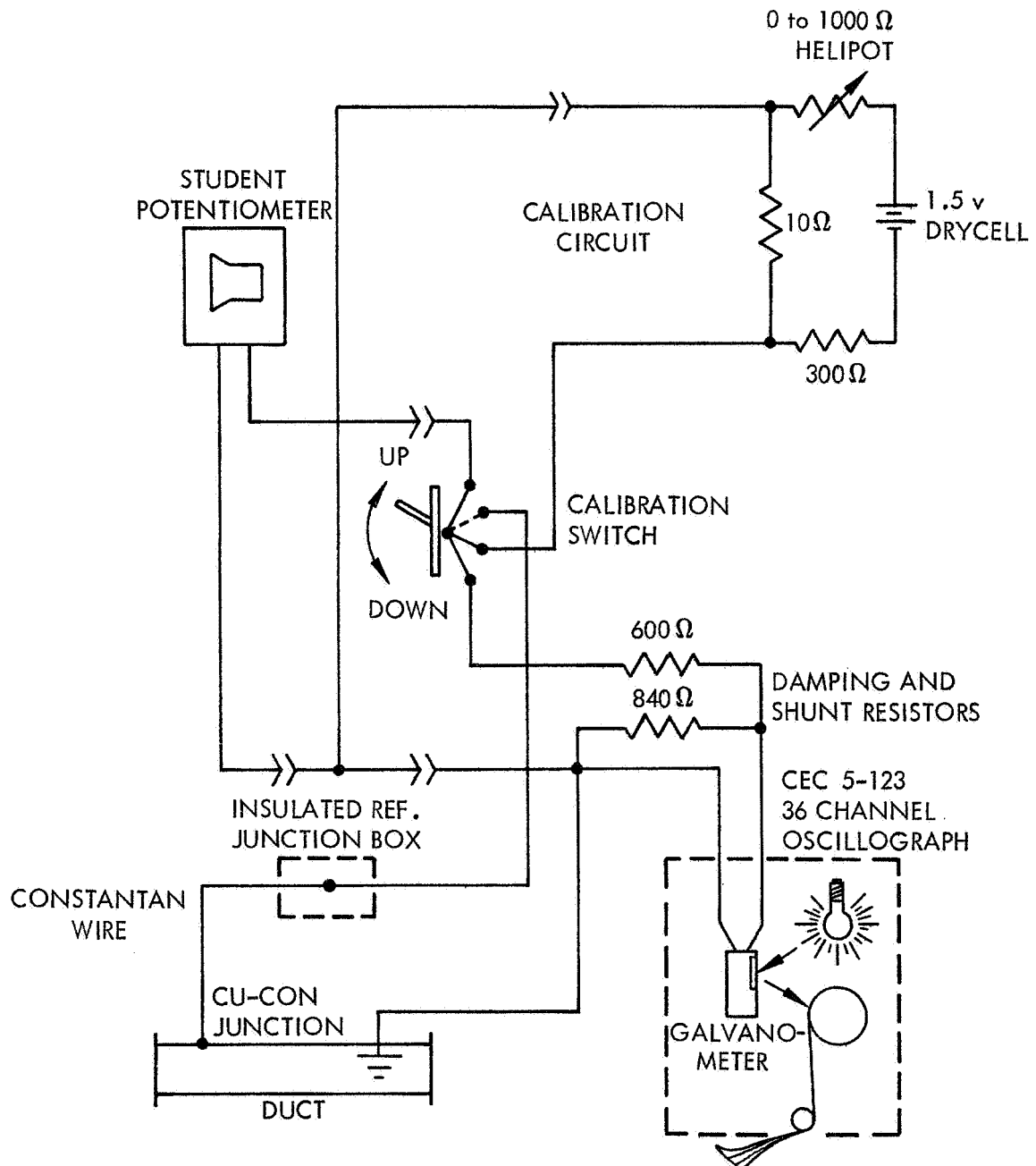
Figure 14.   Schematic of Typical Thermocouple Circuit,
Including Calibration Circuit

R-51368

4.0 TEST PROGRAM AND TEST RESULTS

4.1 FLOW VISUALIZATION TESTS

The flow visualizer apparatus was set up for the cold-flow tests at UTC's Engineering Laboratory. Several checkout runs were made to determine optimum settings for the schlieren system, camera, and duct. The schlieren pictures obtained in the early checkout runs were poor in quality due to surface defects in the glass which were not visible to the naked eye. New purchases of Parallel-O-Plate* glass were made. This is a higher quality (but more brittle) plate glass. The clarity of the photographs was greatly improved with the new glass. A hydrostatic test was conducted to determine the pressure capabilities of the duct with the new glass. No failure was observed in the 1/2-in.-thick windows until a pressure of approximately 100 psi was reached. This pressure was never approached, but the combined effects of pressure and high temperature gradients caused a failure during the hot-gas tests.

After final checkout runs the series of tests in table II were conducted. These cold-flow tests were undertaken to study the effects of pressure ratio on the location of shocks and flow impingement points for various igniter configurations. The effect of pressure ratio on the shock location is shown in figures 15, 16, and 17 for the three configurations tests. The empirical relation of Lewis and Carlson:[11]

$$\frac{x}{D_e} = 0.69 \, Me \left(\frac{\gamma \, P_e}{P_o} \right)^{\frac{1}{2}}$$

predicts the location of the first normal shock within about 10% for the axial-flow head-end igniter. For the aft-end igniter, the shock location is closer to the nozzle than predicted by the above relation or by the charts presented by Love and Grigsby.[12] This is probably due to the reversal in flow direction in the duct for the aft igniter configuration. The shock locations in the jets from the multiple-port igniter are also closer to the port than predicted by either reference 11 or 12. The difficulty involved in making measurements on photographs of this scale and the difficulty in calculating the nozzle pressure ratio due to unknown pressure

---

* A product of Cobbledick-Kibbe Glass Co., San Jose, Calif.
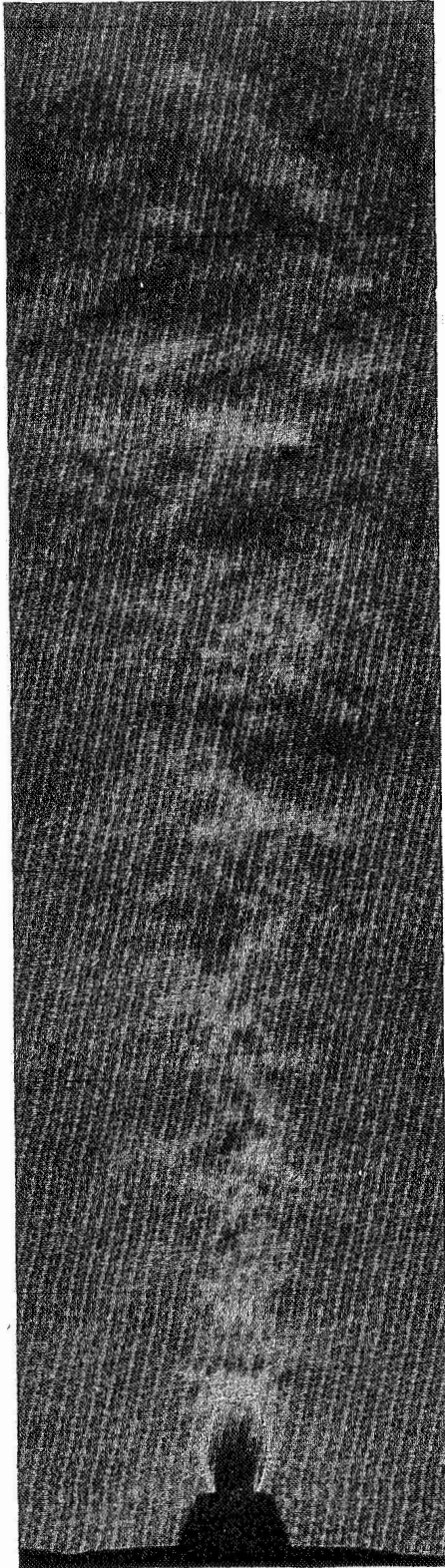
A. Head-end axial igniter, $P_{JET}/P_{DUCT} \approx 13.6$.
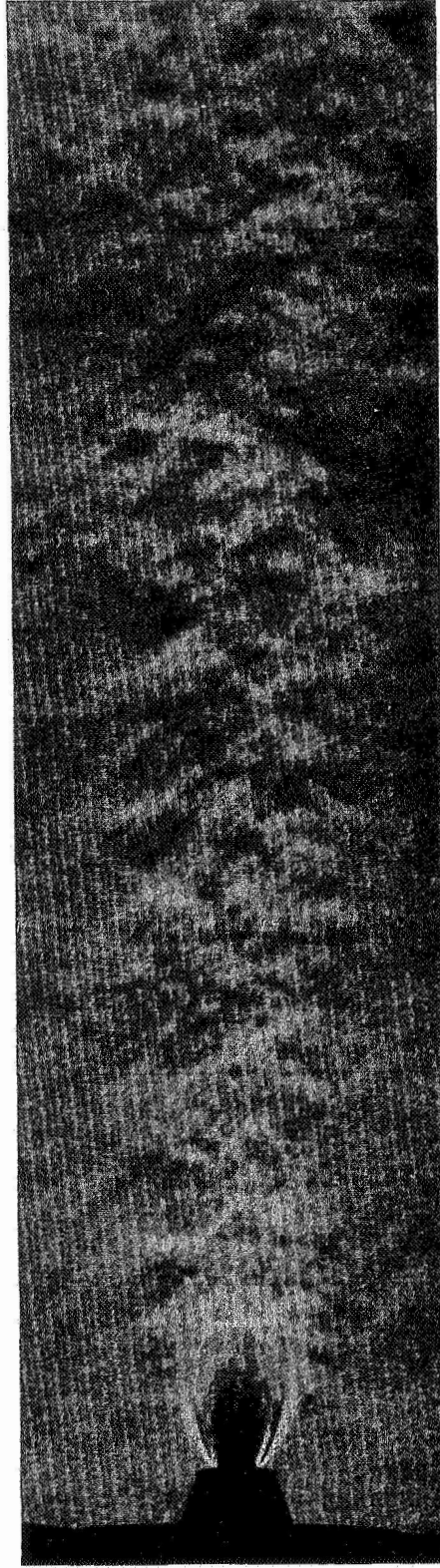
B. Head-end axial igniter, $P_{JET}/P_{DUCT} \approx 29.0$.

R-51403

Figure 15.   Head-End Axial Igniter

A. Aft-end igniter, P_{JET}/P_{DUCT} 11.2.
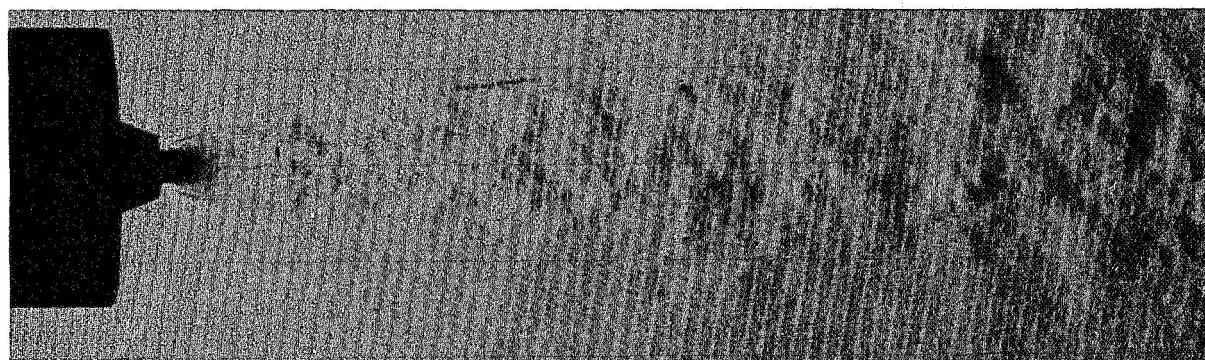
B. Aft-end igniter, P_{JET}/P_{DUCT} 24.2.
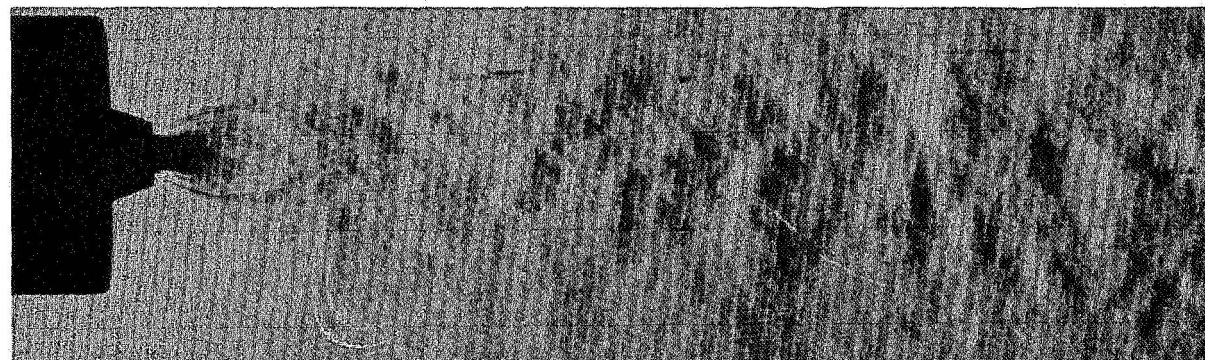
C. Aft-end igniter, P_{JET}/P_{DUCT} 37.0.
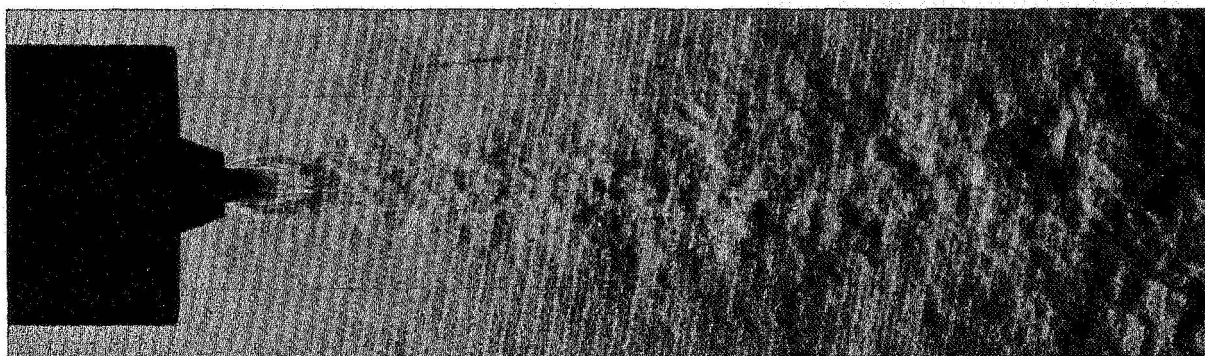
R-51404

Figure 16. Aft-End Igniter
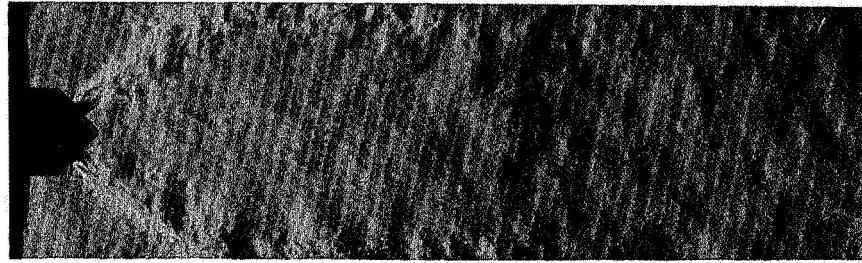
A. Two-port canted igniter, $P_{JET}/P_{DUCT} \approx 12.4$.
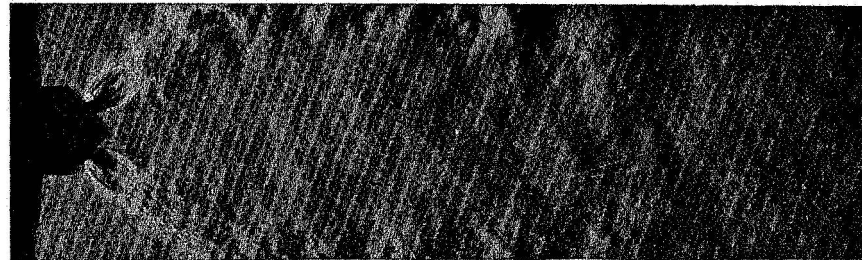
B. Two-port canted igniter, $P_{JET}/P_{DUCT} \approx 28.0$.

R-51405

Figure 17. Two-Port Canted Igniter

TABLE II

COLD-GAS FLOW VISUALIZER TESTS

Run	Duct Window Thickness	Igniter Nozzle	Schlieren Photo	Jet/Duct Pressure Ratio
A	1/4-in.	2-port	x	5.75
B	1/4-in.	2-port	x	5.75
C	1/4-in.	Axial	x	5.46
D	1/4-in.	Axial	x	12.03
E	1/4-in.	2-port	x	8.34
F	1/4-in.	2-port	x	11.62
G	1/4-in.	2-port	x	5.07
H	1/2-in.	Aft, axial	x	11.7
I	1/2-in.	Aft, axial	x	18.72
J	1/2-in.	Aft, axial	x	11.0
K	1/2-in.	Aft, axial	x	1.39
L	1/2-in.	Aft, axial	x	5.01

losses in the canted nozzle are responsible for this error. Impingement points for the axial head-end and aft-end igniters are not visible in the figures (15 and 16, respectively). However, the impingement points for the canted igniter are clearly visible in figure 17. Downstream of the impingement zone the high-velocity flow appears to stay attached to the wall in spite of the unfavorable pressure gradient. At the high pressure ratio (figure 17), there appears to be a shock extending from the wall at the impingement point and through the flow field, indicating that super-sonic flow may be reestablished after the first normal shock. Finally, it is noted that there are no indications of high velocity or turbulence in the separated "base" region, suggesting that the convective heat transfer measurements from the hot-gas tests should show little heat flux in this region.

The hot-gas tests were set up for checkout runs at the Engineering Laboratory at Sunnyvale but were later moved to the Development Center at Coyote, California, for the test program.

Four combinations of igniter configuration and propellant composition were tested as shown in table III. Although schlieren photos were taken of each of the flow visualizer tests, only one of the hot-gas firings produced good results. This photo was taken in run No. 2, a checkout run, and is shown in figure 18. The first normal shock location, indicated by the left side of the large triangular bright spot, is not correctly predicted by the method of Lewis and Carlson. Their equation predicts a shock loca-tion approximately 4.45 exit diameters from the exit plane while measure-ments show the actual location to be 6.25 exit diameters from the exit plane. There is no clear explanation at this time for the discrepancy. Schlieren photography of very hot radiating gases is difficult due to the schlieren light source being overpowered by light from the gas cloud, therefore becoming indistinguishable on the overexposed film.

The heat transfer data collected from the copper plate are shown in figures 19 and 20. These data are total heat flux determined from the rate of temperature rise of localized spots on the copper plate and averaged over the firing duration. The maximum heat flux for both the aluminized and nonaluminized propellant occurs at an axial location of about 2.5 in. from the forward-end igniter. Inspection of figure 18 shows the location of the normal shock to be at about 0.82 in. from the igniter exit plane. The outer edge of the mixing zone is not visible from the photograph but since the the normal shock is not more than one-half of the duct diameter, it may be concluded that the high-velocity mixing zone has not yet reached the wall. The probable location of this impingement zone is the location of maximum heat flux. Data from the canted-nozzle hot-gas tests are shown in figure 20. Alumina in the exhaust appears to cause a large change in the location and
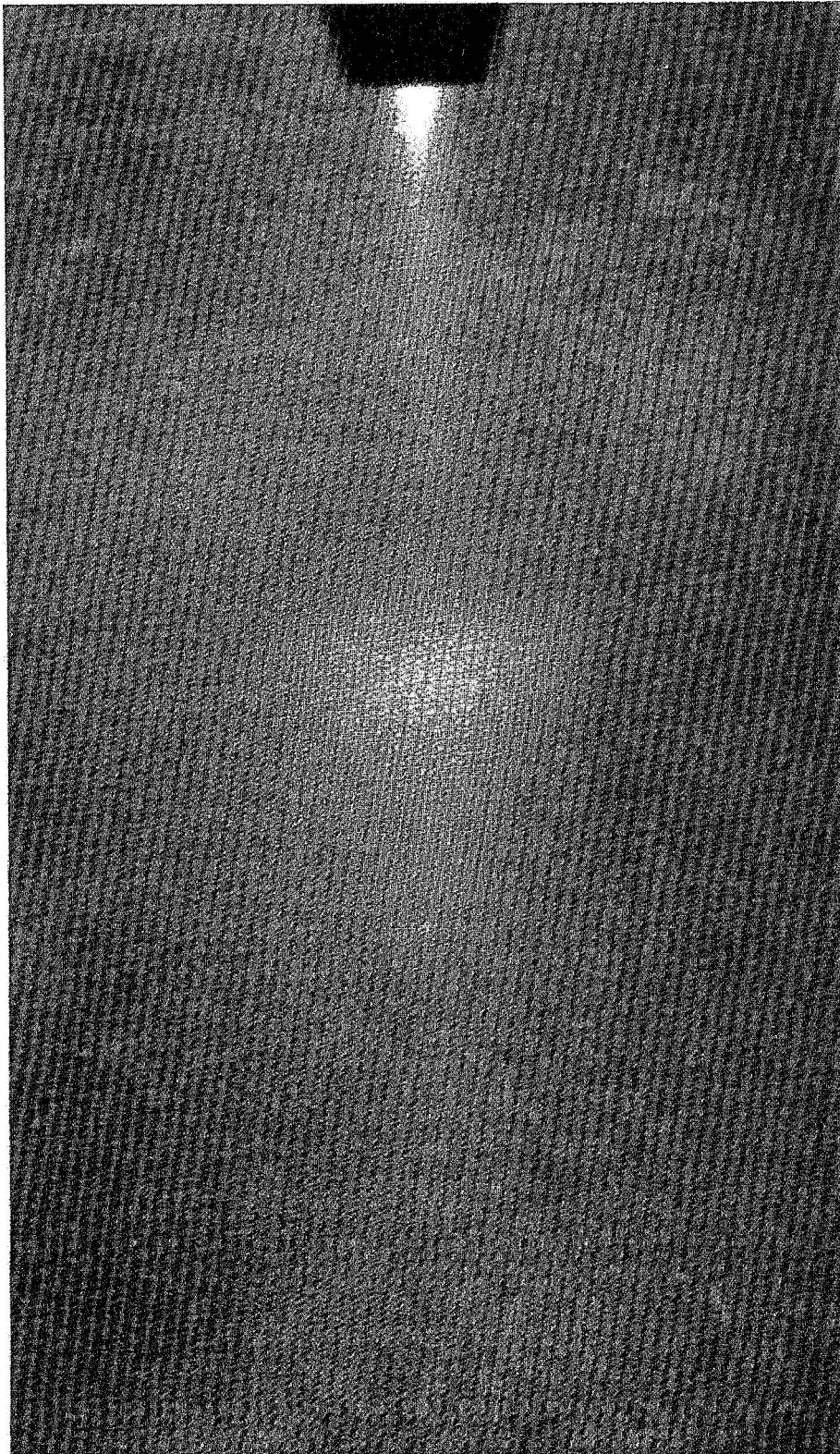
Figure 18. Head-End Axial Igniter Hot-Gas
Firing with Nonaluminized Propellant

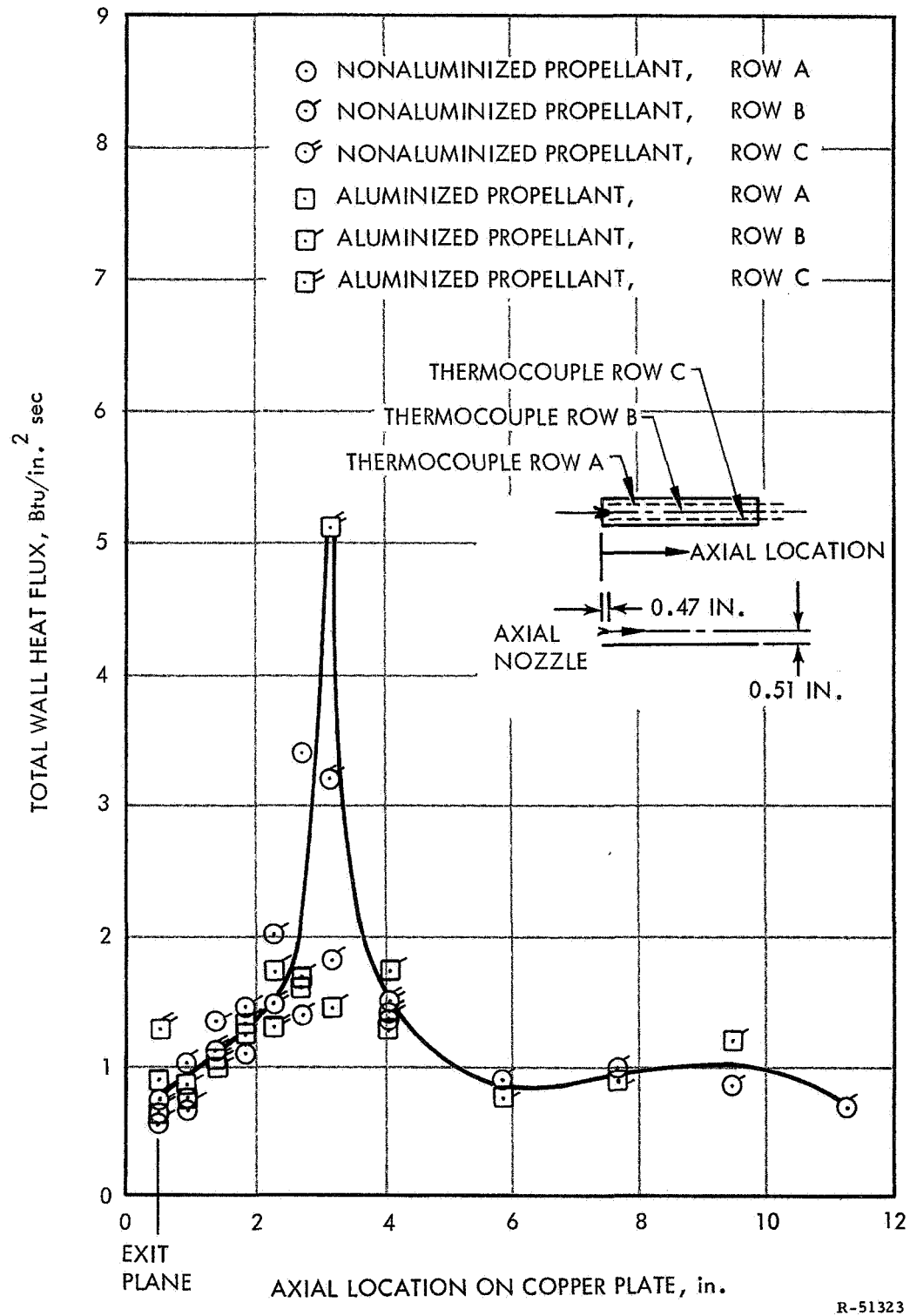Figure 19. Total Heat Flux to Copper Plate from Axial Nozzle
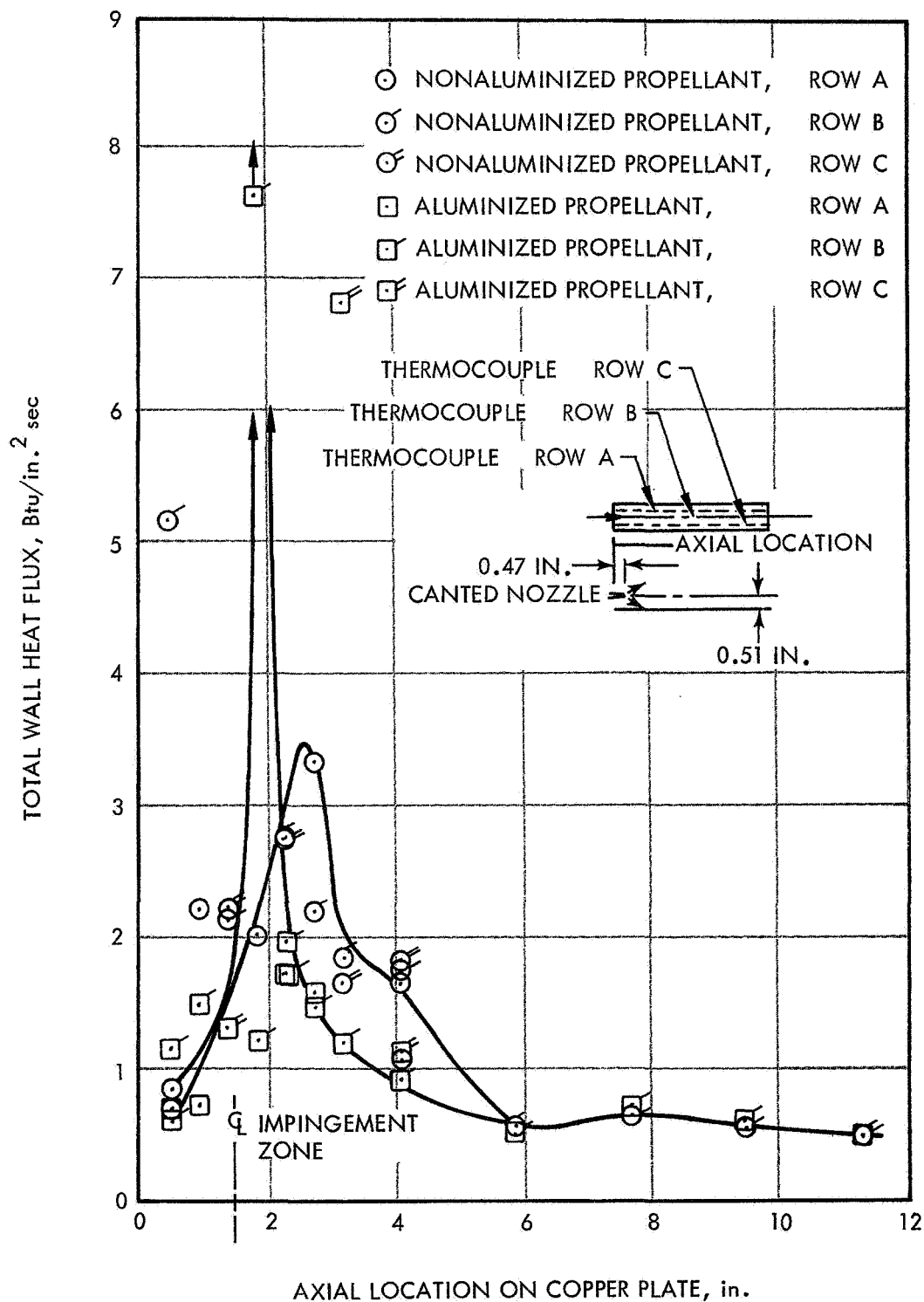with Aluminized and Nonaluminized Propellant

R-51323

Figure 20. Total Heat Flux to Copper Plate from 30° Canted Nozzles
with Aluminized and Nonaluminized Propellant
(Flow Visualization Apparatus)

TABLE III

HOT-GAS FLOW VISUALIZER TESTS

Run	Igniter Nozzle	Igniter Propellant	Schlieren Photo	Movies fr/sec	Copper Plate	Inert Slab	Live Slab
1	2-port	Nonaluminized	x				
2	Axial	Nonaluminized	x	64			
3	2-port	Nonaluminized	x	164	x	x	
4	Axial	Nonaluminized	x	~500	x	x	
5	2-port	Aluminized	x	~500	x	x	
6	Axial	Aluminized	x	~500	x	x	x

magnitude of the maximum heat flux. The location of maximum heat flux downstream of the projected orifice centerline (impingement zone) and the decrease in heat flux (between 2.2 and 5.8 in.) due to the aluminized exhaust, are not intuitively satisfying. The data from both of these runs were taken over a short igniter duration since both of the canted igniters failed early (110 msec and 40 msec) and all heat transfer data had to be read out prior to failure. Conclusions based on these data were withheld until after the copper duct tests. Data from the copper duct tests are presented later in this section. There is no evidence of a decrease in heat flux with the aluminized propellant, and the position of maximum heat flux for the canted igniters is always near the impingement point.

From the high-speed color motion pictures the axial variation of radiant intensity of the jet and gases contained in the duct may be qualitatively observed. The high-density jet core and gases directly behind the normal shock produce the most intense radiation. The remainder of the chamber produces less intense radiation which varies from a maximum at the center of the duct to lower values at the ends of the duct, as predicted by Kennedy (appendix B).

Propellant sample holding plates, cast with an inert propellant, were placed on the upper wall of the duct for three of the hot-gas tests. No measurable erosion was detected when the sample was subjected to the axial igniter with nonaluminized propellant.

The directly impinging canted igniter, however, produced significant erosion near the centerline of the impingement zone. Precise measurements

of total erosion were not possible due to the small scale and short duration; however, approximate measurements show erosion rates of 0.19 in./sec and 0.37 in./sec for the nonaluminized and aluminized jets, respectively. These values are felt to be accurate to within ±50%. It is noted that these erosion rates are similar to and higher than live propellant burning rates at the same chamber (duct) pressure. The maximum erosion did not occur at the intersection of the projected jet centerline with the propellant surface, but approximately 0.3 to 0.5 in. upstream of the impingement point instead. Propellant ablation and erosion during ignition must be investigated more thoroughly before an understanding of the controlling phenomena is obtained.

4.2 COPPER DUCT TESTS

Twenty-eight test runs were conducted using the copper duct apparatus and various igniter configurations as outlined in table IV. The first tests (runs 0 to 14) employed the head-end igniter configurations. (See figure 8.) Three variations of igniter mass flow rate are made in each configuration, with nonaluminized and aluminized propellants. (An exception was made in the runs utilizing canted nozzles and aluminized propellants because of possible thermal damage to the duct at the high flow rates.)

4.2.1 Total Heat Flux

4.2.1.1 Head-End Igniter

Figures 21 and 22 show the axial variation of total heat flux for the axial flow igniter. The thermocouple data are obtained in two longitudinal planes. Since for the axial igniter the flow is symmetrical about the duct centerline, no variations are expected around the duct periphery. Variations which do occur (represented by flagged symbols versus unflagged symbols) are due to data scatter.

The axial variation in heat flux from the multiple-port canted igniters is shown in figures 23 and 24 for nonaluminized and aluminized propellants at several mass flow rates. These data are jet centerline data only. Peripheral variations in total heat flux are expected in the regions near the stagnation point. These variations should disappear as the jets spread and coalesce. Figures 25, 26, and 27 show this variation for the nonaluminized multiple-port igniters, and figures 28 and 29 represent the variation for the aluminized multiple-port canted igniters.

TABLE IV
COPPER DUCT TESTS

| Run No.	Igniter Location	Igniter Type	Propellant Type	Nominal Flow Rate lb/sec	Nominal Duct Pressure psig	Radiation Calorimeters	Spectral Radiometer	External Thermocouples	Internal Surface Thermocouples	Duct Pressures
0	Head end	Axial	Nonaluminized	1.60	17	6	—	16	—	2
1	Head end	Axial	Nonaluminized	1.60	17	6	—	16	—	4
2	Head end	Axial	Nonaluminized	2.52	30	6	—	16	—	4
3	Head end	Axial	Nonaluminized	3.55	50	6	—	16	—	4
4	Head end	Axial	Nonaluminized	2.52	17	6	—	16	—	4
5	Head end	Canted	Nonaluminized	1.60	17	6	—	16	—	4
6	Head end	Canted	Nonaluminized	2.52	30	6	—	16	—	4
7	Head end	Canted	Nonaluminized	3.55	50	6	—	16	—	4
8	Head end	Canted	Nonaluminized	2.52	17	6	—	16	—	4
9	Head end	Axial	Aluminized	1.60	17	6	—	16	—	4
10	Head end	Axial	Aluminized	2.52	30	6	—	16	—	4
11	Head end	Axial	Aluminized	3.55	50	6	—	16	—	4
12	Head end	Axial	Aluminized	2.52	17	6	—	16	—	4
13	Head end	Canted	Aluminized	1.60	17	6	—	16	—	4
14	Head end	Canted	Aluminized	2.52	30	6	—	16	—	4
17	Aft end	Axial-Supersonic	Nonaluminized	1.60	17	5	—	16	—	5
18	External Aft end	Axial-Supersonic	Nonaluminized	2.57	30	6	—	16	—	5
19	Aft end	Axial-Supersonic	Nonaluminized	3.55	50	5	—	16	—	5
20	External Aft end	Axial-Supersonic	Nonaluminized	1.60	17	5	—	16	—	5
21	Aft end Internal (11/in.)	Axial-Supersonic	Nonaluminized	2.52	30	5	—	16	—	5
22	Aft end Internal (11/in.)	Axial-Supersonic	Nonaluminized	3.55	50	6	—	16	—	5
24	Aft end Internal (11/in.)	Axial-Sonic	Nonaluminized	2.52	30	6	—	16	—	5
25	Aft end Internal (11/in.)	Axial-Sonic	Nonaluminized	3.55	50	6	—	16	—	5
26	Aft end Internal (11/in.)	Axial-Supersonic	Aluminized	1.60	17	5	—	16	—	5
27	Aft end Internal (11/in.)	Axial-Supersonic	Aluminized	2.52	30	5	—	16	—	5
28	Aft end Internal (11/in.)	Axial-Supersonic	Aluminized	3.55	50	5	—	16	—	5
29	Aft end Internal (11/in.)	Axial-Sonic	Aluminized	1.60	17	5	—	16	3	5
30	Aft end Internal (11/in.)	Axial-Sonic	Aluminized	2.52	30	5	—	16	3	5
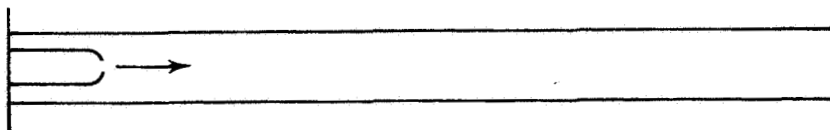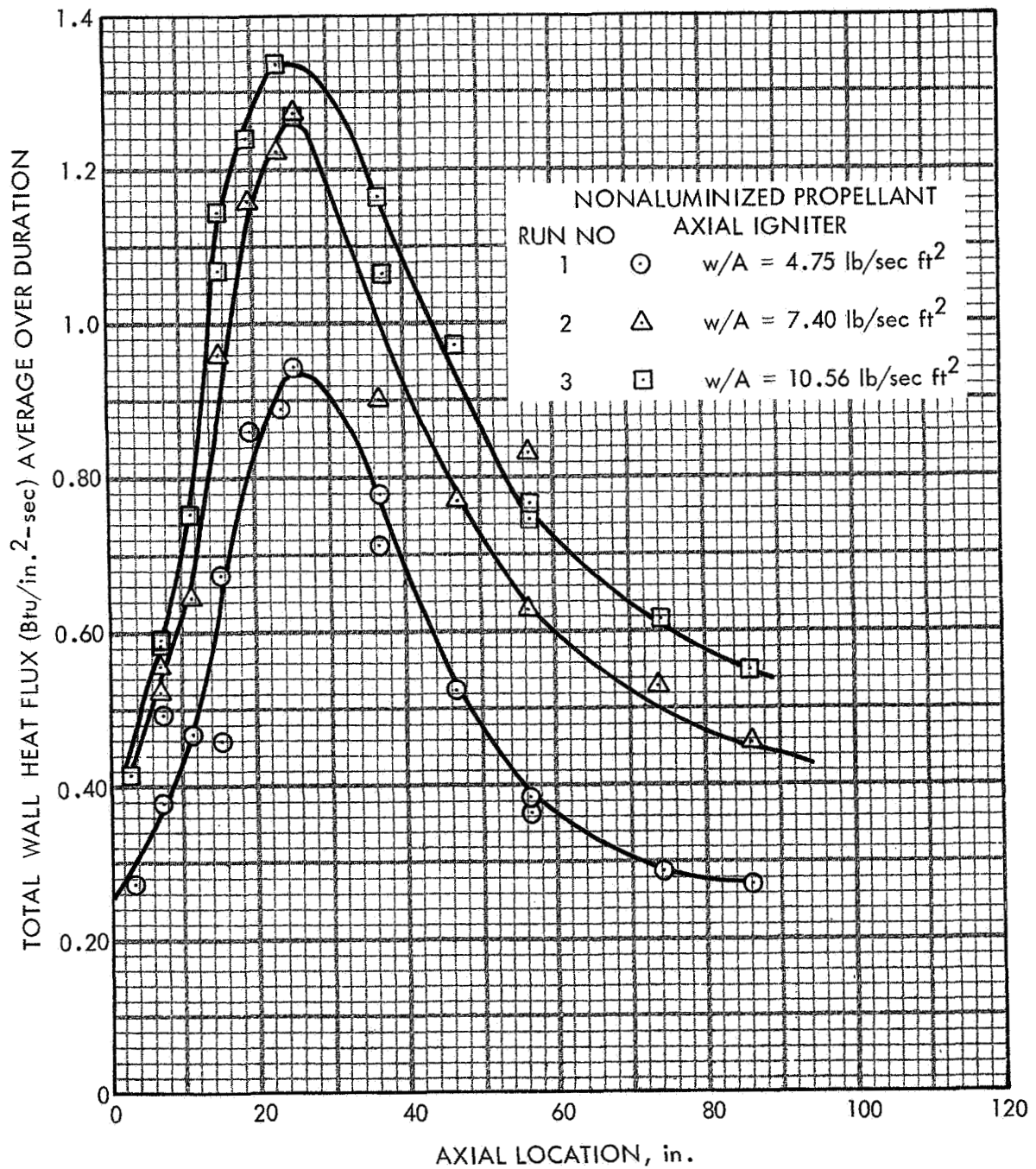
Figure 21. Average Wall Heat Flux in Copper Tube
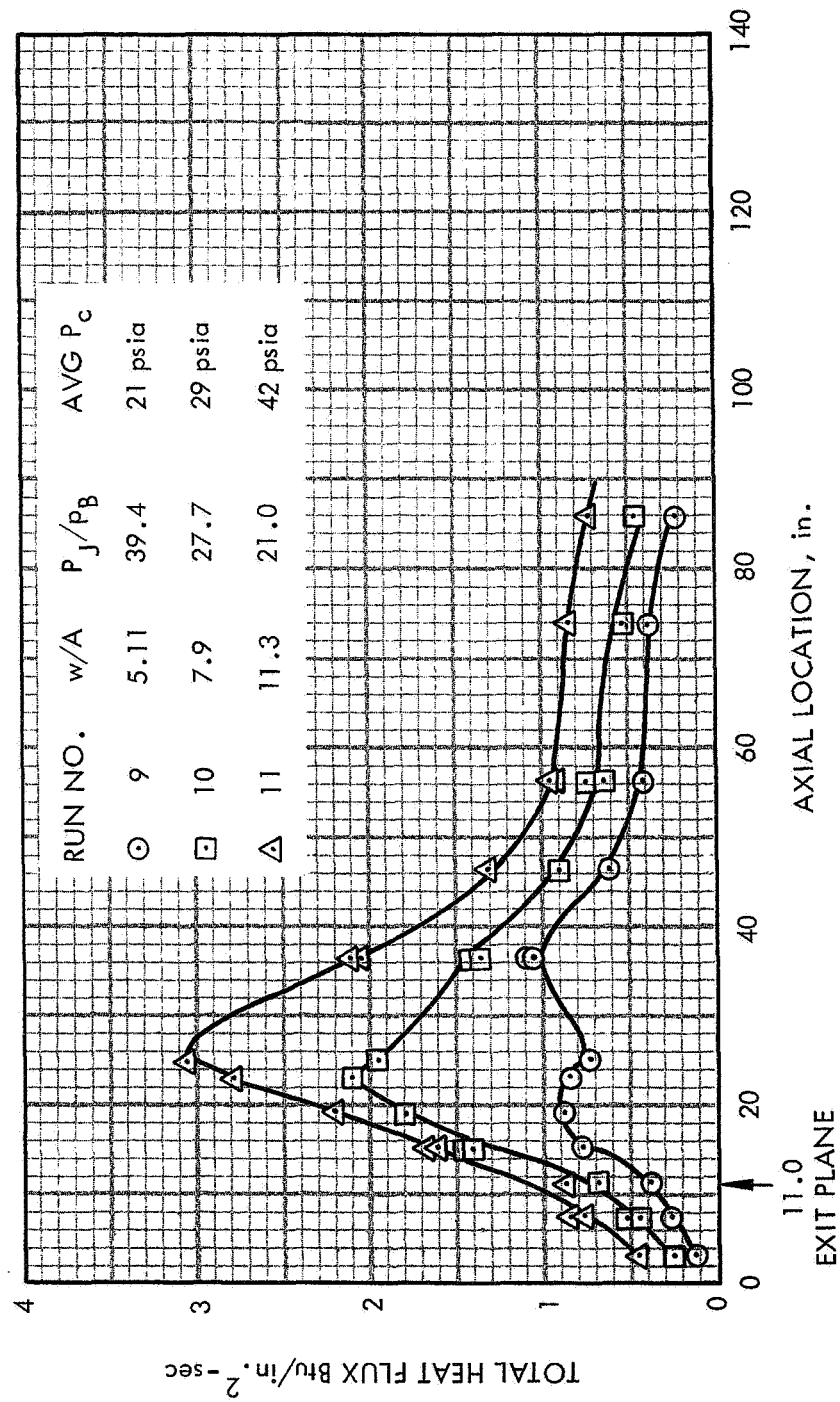
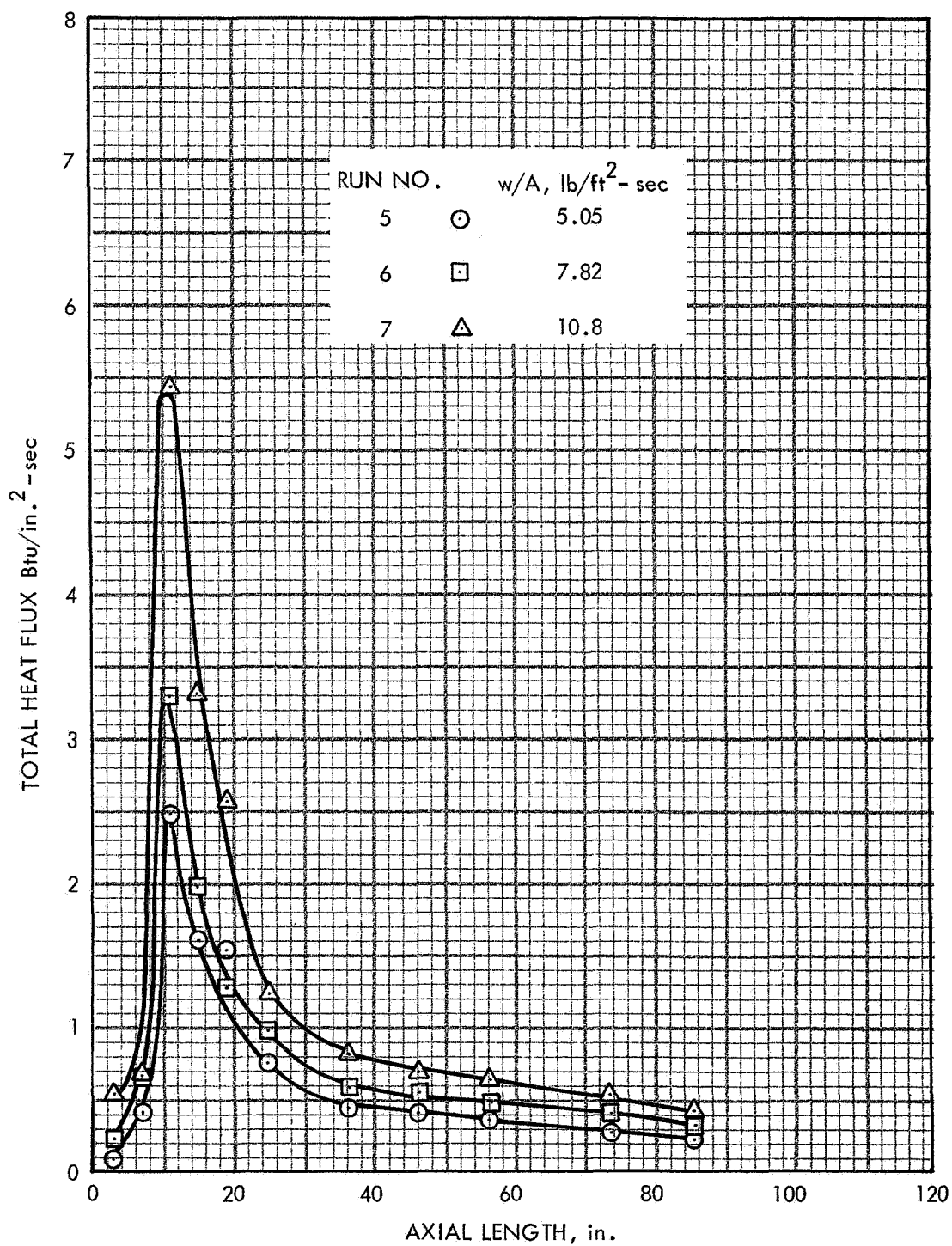Figure 22. Axial Igniter, Aluminized Propellant

R-51385

R-51370

Figure 23. Canted Igniter Nonaluminized Products
Jet Centerline Flux Only
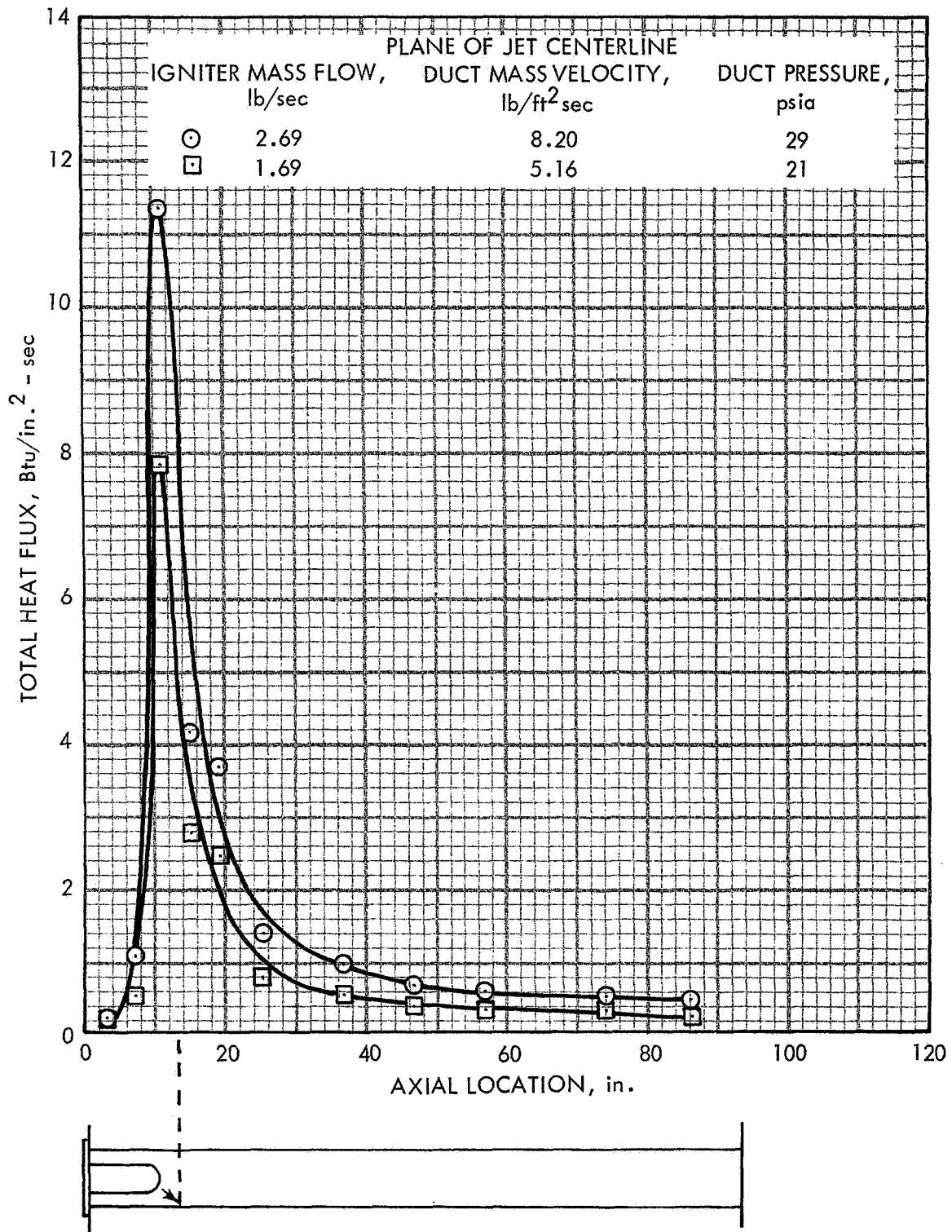
Figure 24. Multiple-Port Canted Igniter, Aluminized
Exhaust (18.9% Al_2O_3), Total Heat Flux vs Length

Figure 25. Multiple-Port Canted Igniter, Nonaluminized Propellant,
Total Heat Flux vs Length

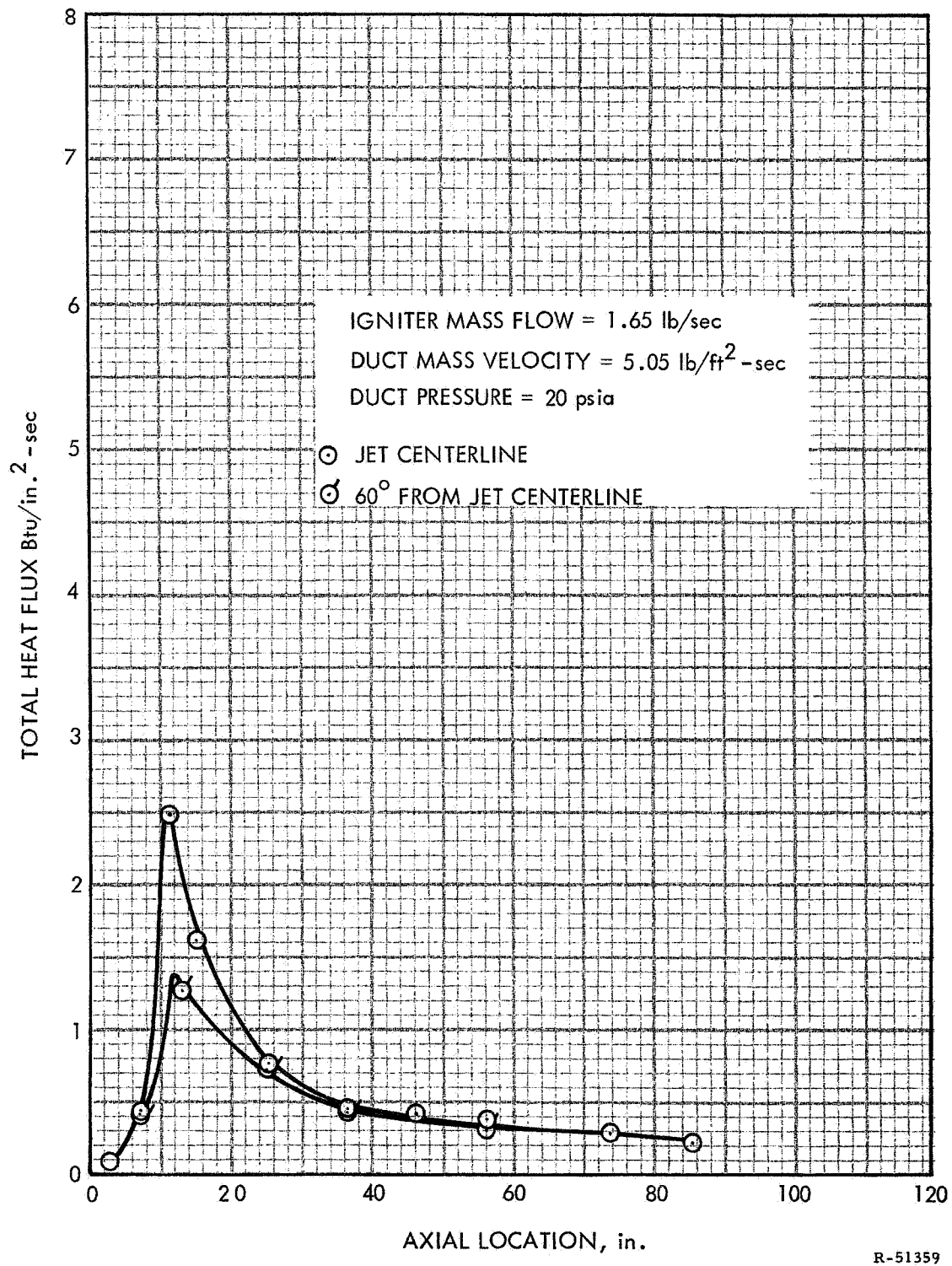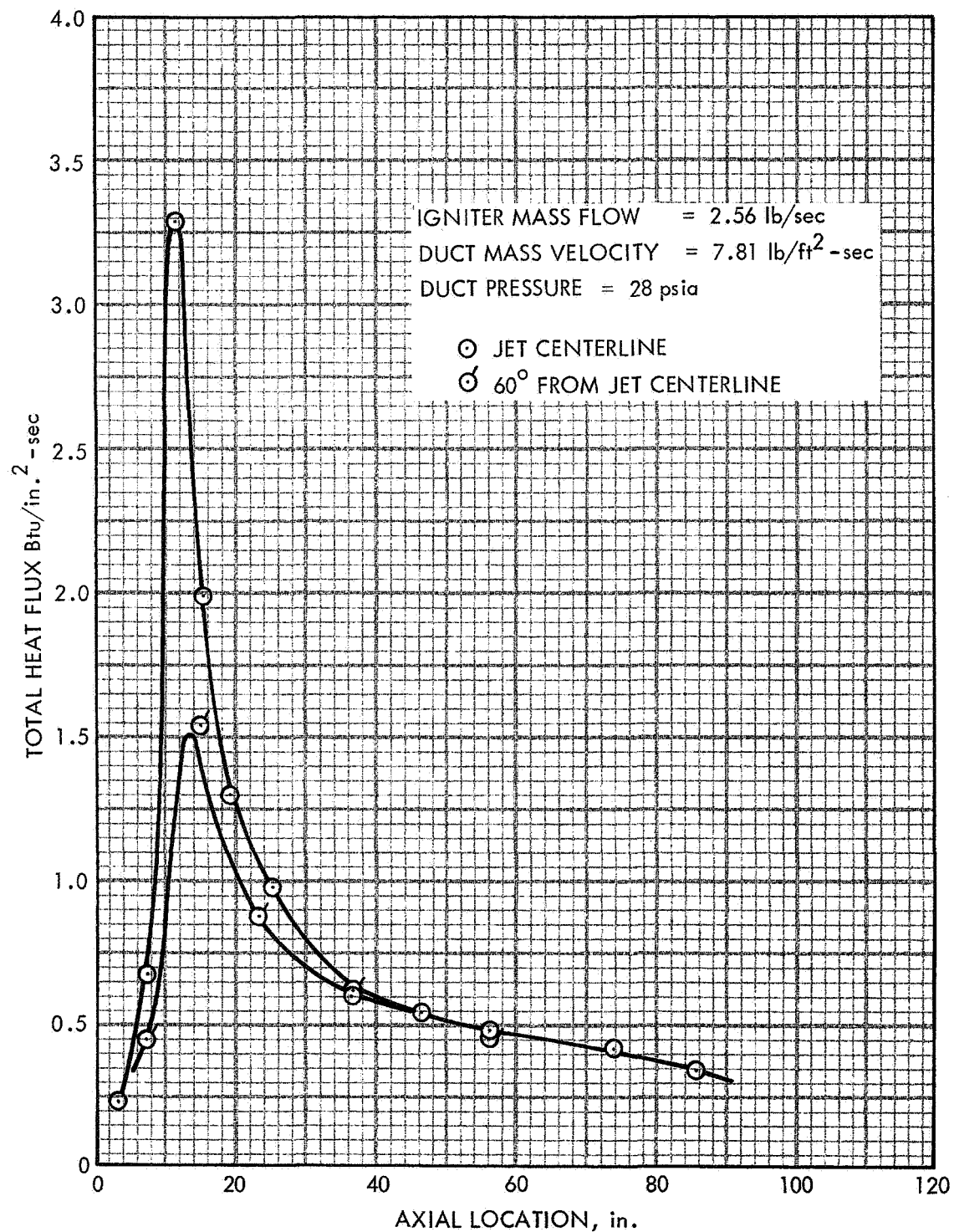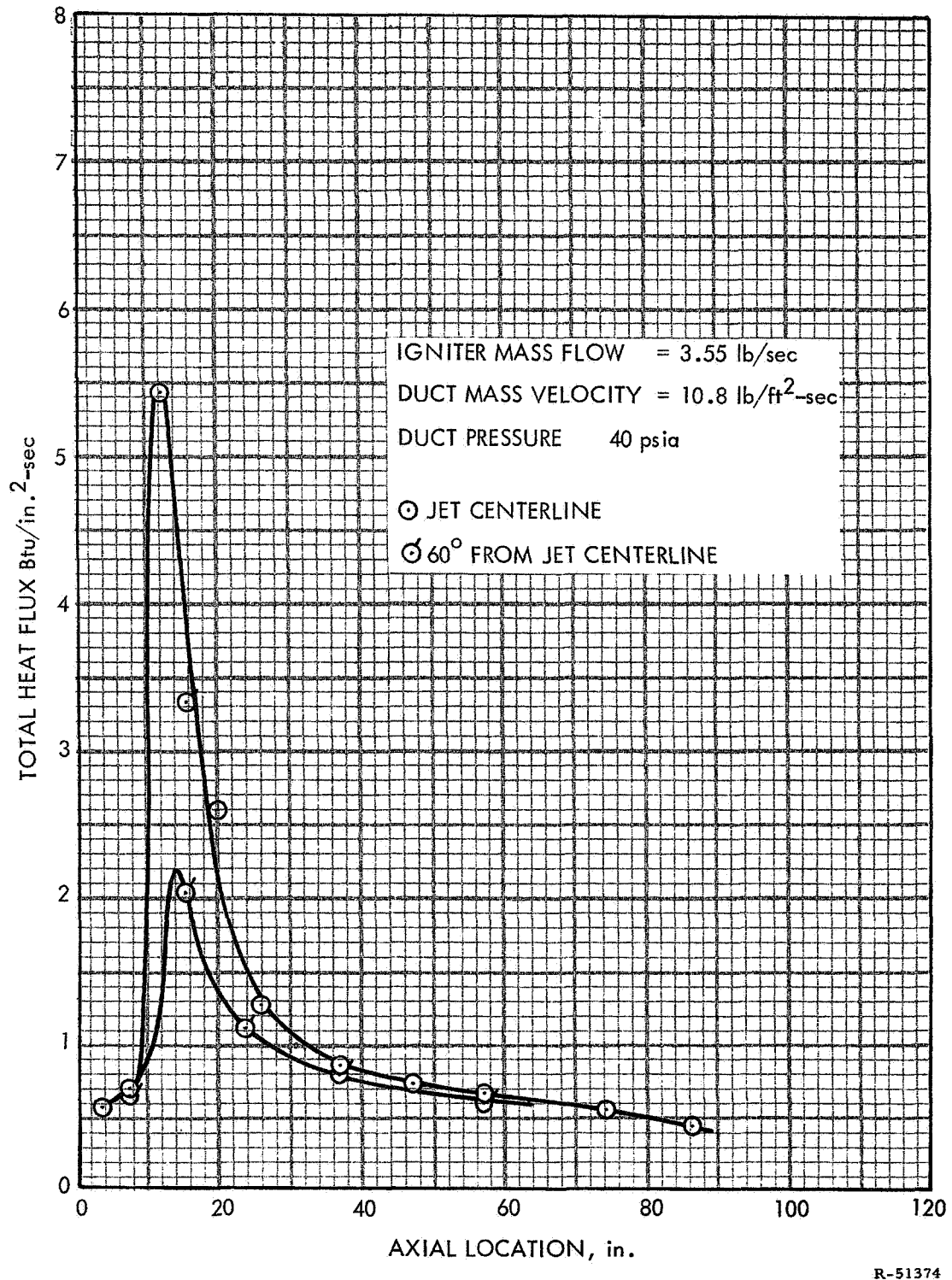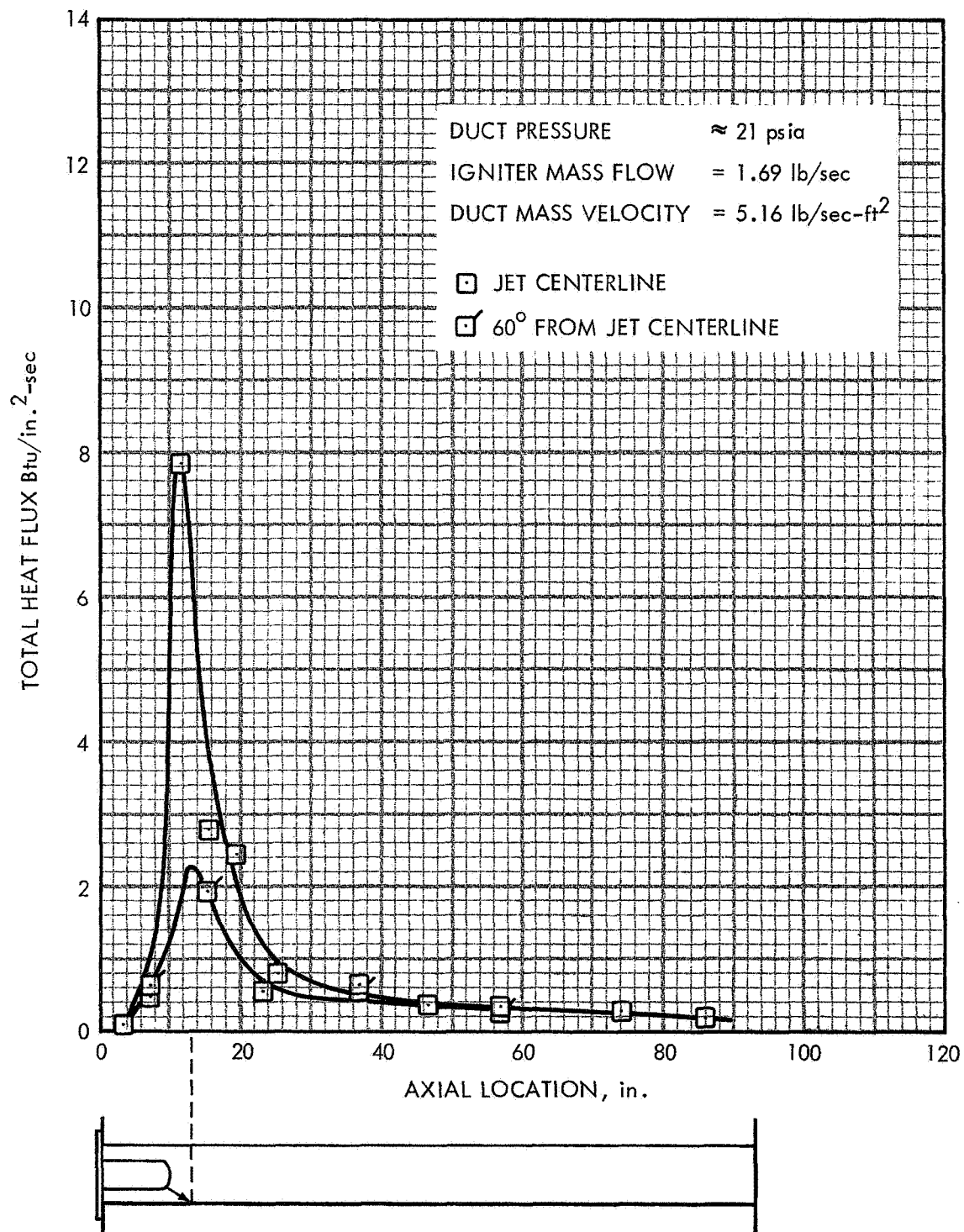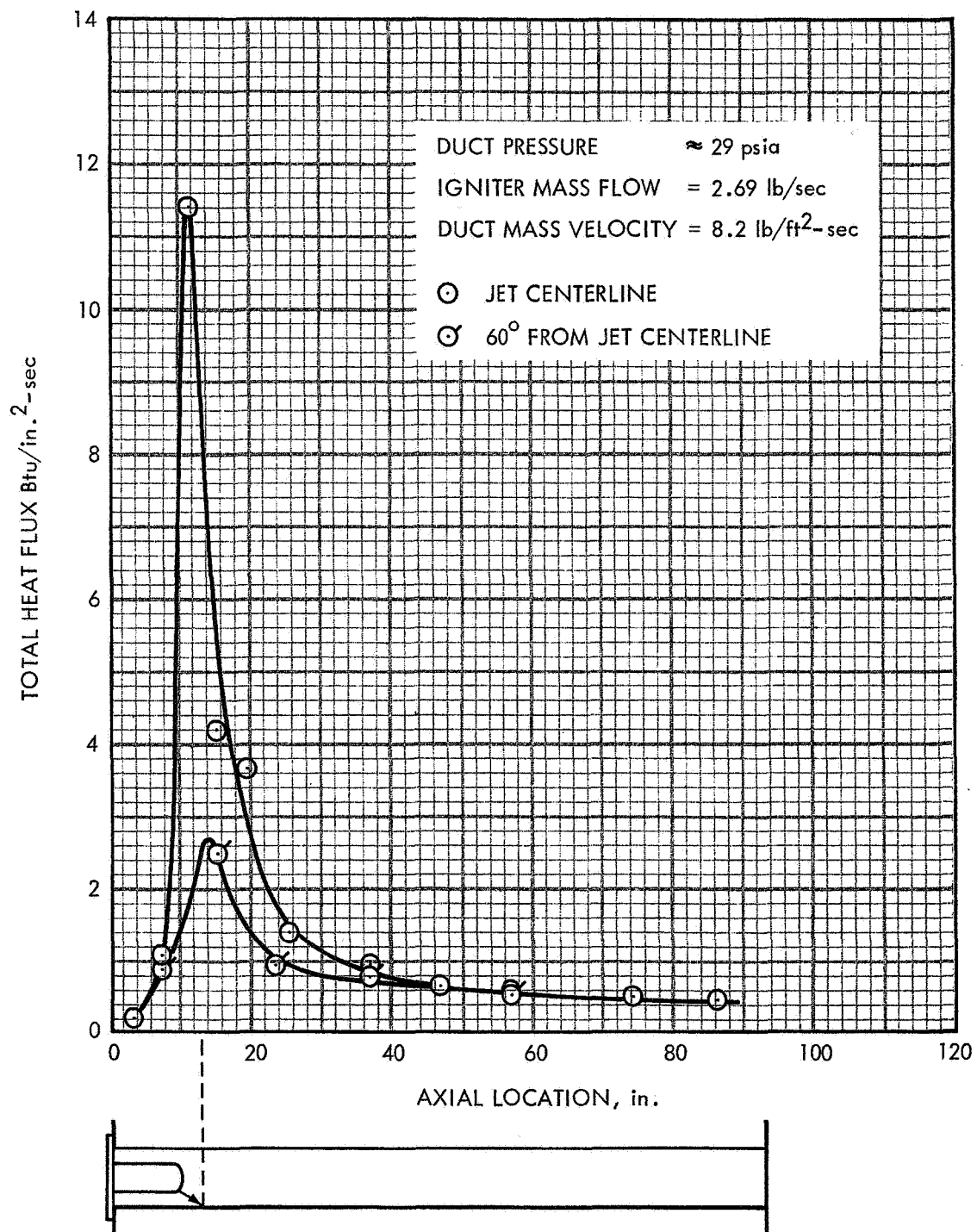Figure 26. Multiple-Port Canted Igniter, Nonaluminized Propellant,
Heat Flux vs Length

Figure 27.   Multiple-Port Canted Igniter, Nonaluminized Propellant,
Total Heat Flux vs Axial Location

Figure 28. Multiple-Port CantedIgniter, Aluminized Products
(18.9% Al$_2$O$_3$), Total Heat Flux vs Length

Figure 29. Multiple-Port Canted Igniter, Aluminized Products
(18.9% Al_2O_3), Total Heat Flux vs Length

4.2.1.2 Aft-End Igniters

The total heat flux data for the aft-end igniters are presented in figures 30 and 31. The variations due to igniter mass flow are shown in figure 30. These data are all for aluminized propellant products exhausting into the duct from a near-optimum expansion ratio supersonic nozzle. The steady-state location of the dividing line between igniter gases and entrapped air is very evident in this plot. Also the shift of maximum heat transfer point with igniter mass flow rate is evident. In figure 31 the effect of adding alumina to the exhaust products is shown. Due to time limitations, no more data on the aft-end igniter could be reduced. The quality of the results in figures 30 and 31 warrants further work in reducing and studying this data.

4.2.2 Total Heat Flux Data Reduction

The measured transient temperature data must be reduced from a time versus displacement form on the oscillographs to a time versus temperature curve which is smooth, has continuous derivatives, and accurately represents the actual temperature which was measured. The inverse heat conduction solution requires extremely accurate data, since any small error introduced by the data reduction process on the external boundary will be greatly magnified at the internal boundary by the inverse solution..

The use of automatic data readout equipment for transferring the temperature traces on the oscillographs onto punched cards produced a random scatter in the temperature data. The oscillograph traces themselves were smooth, but the readout produced the scatter. When these reduced curves were introduced to the data reduction computer program (appendix C), it was found that their derivatives were not continuous and the program was unable to reach a reasonable solution for the internal surface heat flux. As a result a smoothing technique was employed. The smoothing consisted of fitting the data to a fourth-degree polynomial using a least-squares technique. An example of the readout curve and the fourth-degree fit-curve is shown in figure 32. This example is taken from run 11, channel 20.

It is to be noted that the fit is quite good, but that the data scatter and resulting curve fit have introduced a gentle "valley" or "S" shape to the fitted curve. This curve should be nearly linear beyond about 50 msec with a slope which would indicate the steady-state heat flux. The oscillograph traces do show this portion of the curve to be nearly linear with no "S" curve and the pressure curves to be steady.
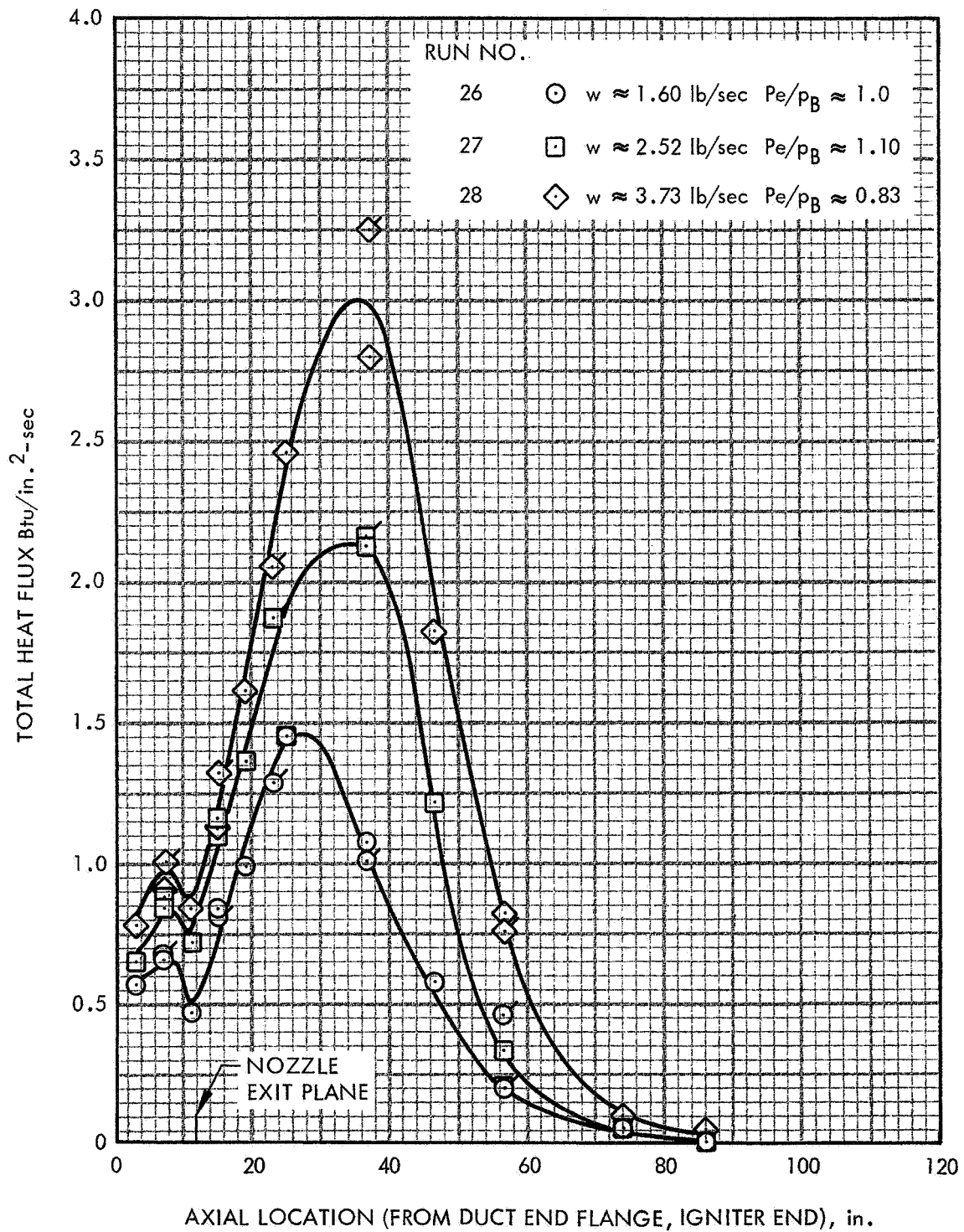
Figure 30. Aft Igniter - Supersonic Nozzle, Aluminized Exhaust
(18.9% Al_2O_3), Total Heat Flux vs Length
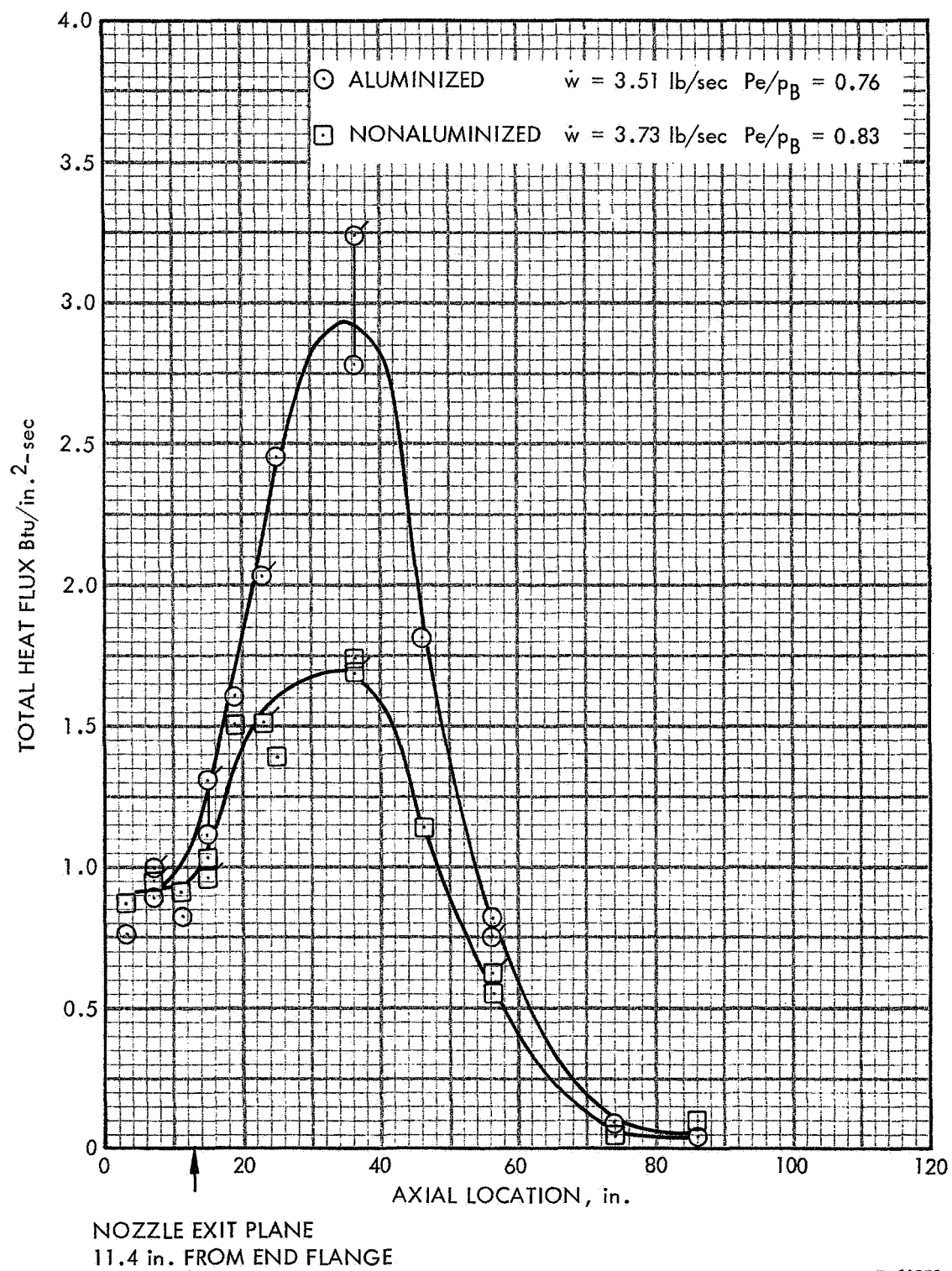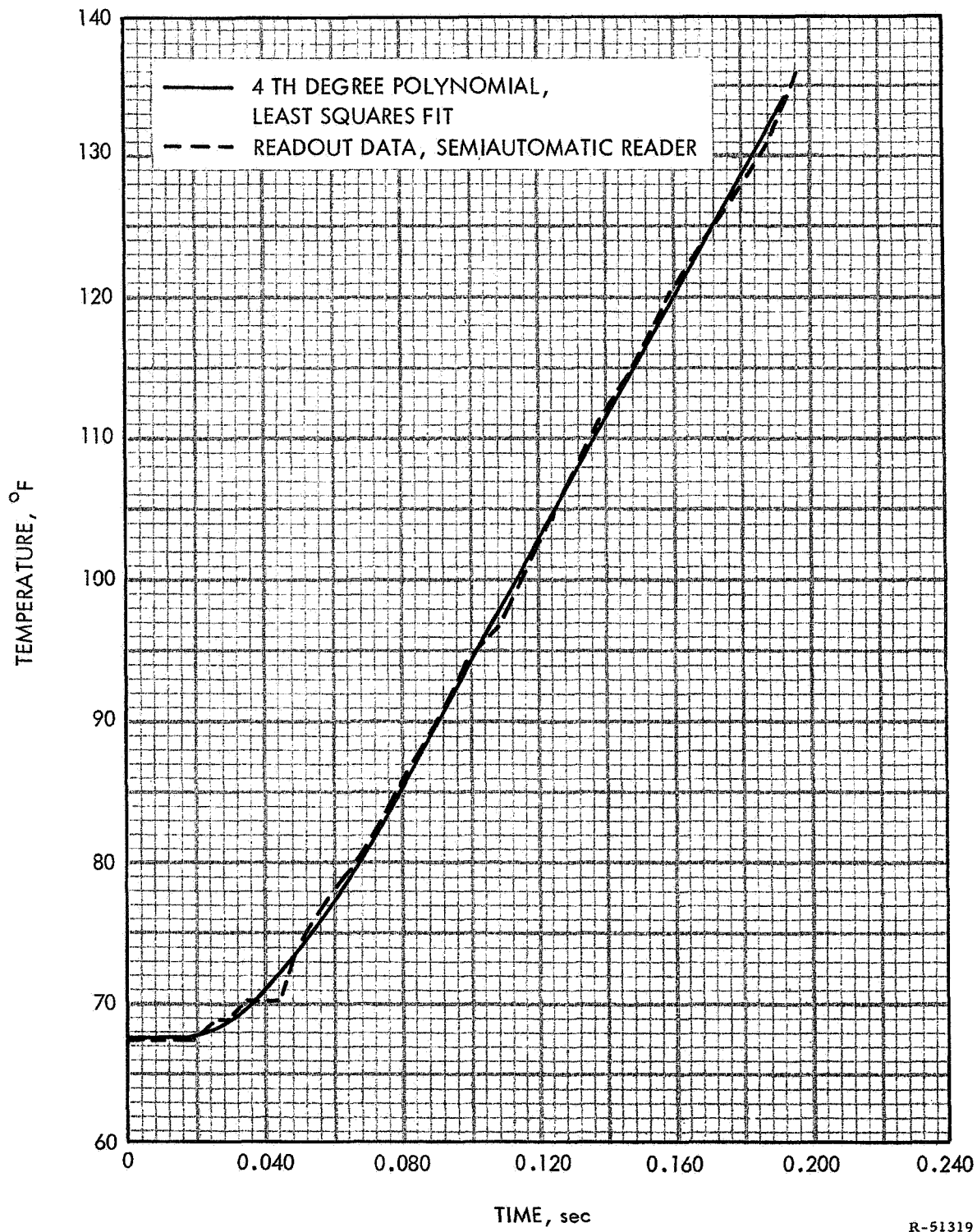
Figure 31. Aft Igniter, Supersonic Jet

R-51378

Figure 32. Run 11, Channel 20, Backside Temperature

R-51319

When this curve is introduced to the heat conduction program, the results, which are displayed in figures 33 and 34, illustrate the magnification produced by an invalid perturbation in external temperature. Note that the heat conduction program matched the external surface temperature quite well (figure 33), but that the large fluctuation in calculated heat flux rate after 60 msec is due to the almost unnoticed change in slope of the measured curve. If a straight line is fit along that portion of the temperature trace which should be linear, a steady-state heat flux of 1.62 Btu/in.^{2} -sec is calculated. This is seen plotted in figure 34 and appears to be a rough average of the results calculated from the transient curve.

These results imply that the steady-state portion may not have a unique error introduced to it, but that similar errors may exist in the transient portion of the temperature curves.

All of the data taken experienced this scatter phenomenon when read, and the fitted curves produced similar results as described above. Since these results are not satisfactory for producing a transient heat flux, only the steady-state solutions were determined for selected runs and channels. It should be pointed out that the computer program will yield a good solution but that a very careful job of data reduction must be done. Semiautomatic data reduction techniques are not satisfactory.

Future improvements which could be made to the data acquisition and reduction system are the following:

A. Redesign damping resistor circuit to obtain more galvanometer deflection per degree temperature rise on the oscillograph. The present system averages about 0.008 in./°F. This is adequate for the points of maximum heat flux when the canted nozzles are used but it is too insensitive for other regions.

B. Carefully hand reduce the measured data to reduce the scatter and error which are greater in a mass-data reduction effort using semiautomatic data readers.

C. Use a more sophisticated curve-fit routine which combines a straight line for the steady-state portion and a polynomial for the transient portion.

D. Make the temperature measurements near or at the inside surface. This would require perfecting the inside surface thermocouple discussed in section 2.0.

These improvements would most likely yield much better transient results, but would be more expensive per temperature channel.
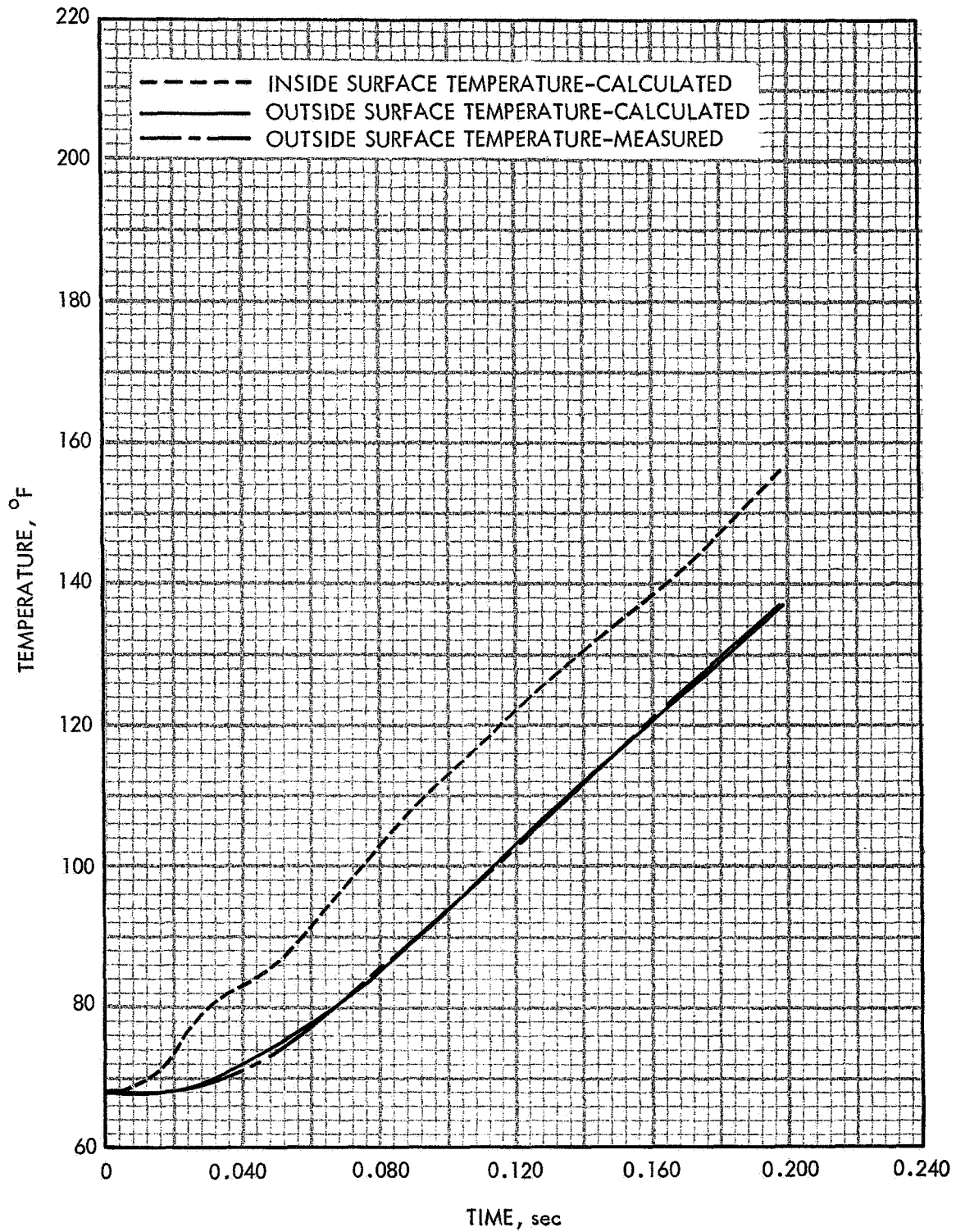
R-51318

Figure 33. Run 11, Channel 20, Calculated Inside and Outside Surface
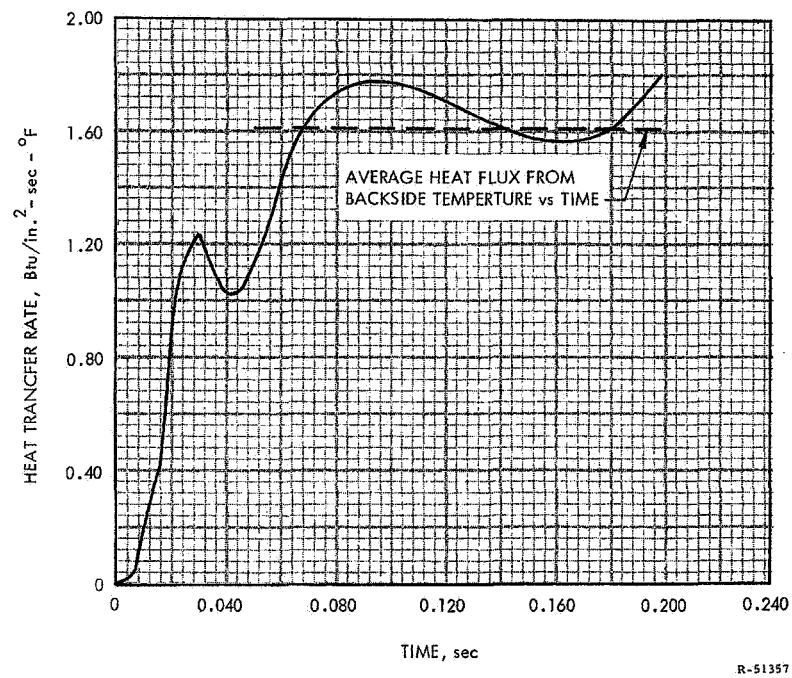Temperatures and Measured Outside Surface Temperature

Figure 34. Run 11, Channel 20, Calculated Heat Flux Rate
(Convection Plus Radiation)

4.2.3 Radiation Data and Results

Radiation data for the head-end, axial flow igniter are shown in figures 35 and 36. In figure 35, the axial variation in measured flux is plotted for the nonaluminized propellant. The axial variation is as expected for a radiating cloud in a duct. Two runs at the same pressure but different mass flow rates are included on the plot. The data for these two runs should have been nearly identical. The variance is attributable to the scatter obtained in this type of measurement. Considering the difficulty in obtaining this type of data the results are in general quite satisfactory. In figure 36 the data for the aluminized axial flow igniters are plotted. The relation of the data from figures 35 and 36 to one another is within the proper ratio for the temperature differences in exhaust products of aluminized and nonaluminized propellants.

The radiation data from the multiple-port canted igniters are shown in figures 37 and 38. Downstream of the impingement zone the level of radiation intensity should be very close to that of the axial igniter data at the same pressure. This is observed to be the case for the nonaluminized data (figure 37) but the scatter is so bad in the aluminized data (figure 38) that no conclusions may be drawn.

The axial variation of radiant heat flux for the aft-end igniter is shown in figures 39 and 40. Figure 39 shows the influence of duct pressure on the radiation intensity for the aluminized propellant. The abrupt dropoff in flux in the stagnation end of the duct is strong evidence that very little mixing occurs between the igniter exhaust and the entrapped air. The peak radiation intensity is approximately the same as that observed during the head-end igniter tests. Figure 40 compares the radiant intensity for the aluminized and nonaluminized aft-end igniters. The variation is about what would be expected based on previously observed effects in the head-end igniter tests.

4.2.4 Duct Pressure Data

Duct pressure data, after initial transients, are presented in figures 37 to 40 for all aft-end igniter configurations.

For each igniter-propellant combination, there was one run scheduled in which the duct orifice plate was changed to a larger size in order to obtain at least one variation of mass flow rate with no change in duct pressure as well as a variation in duct pressure with no change in mass flow rate. The similarity in duct pressure for corresponding mass flows noted through figures 41 to 44 is intentional and permits direct comparison of igniter configurations with minimal corrections for pressure and mass flow rate.
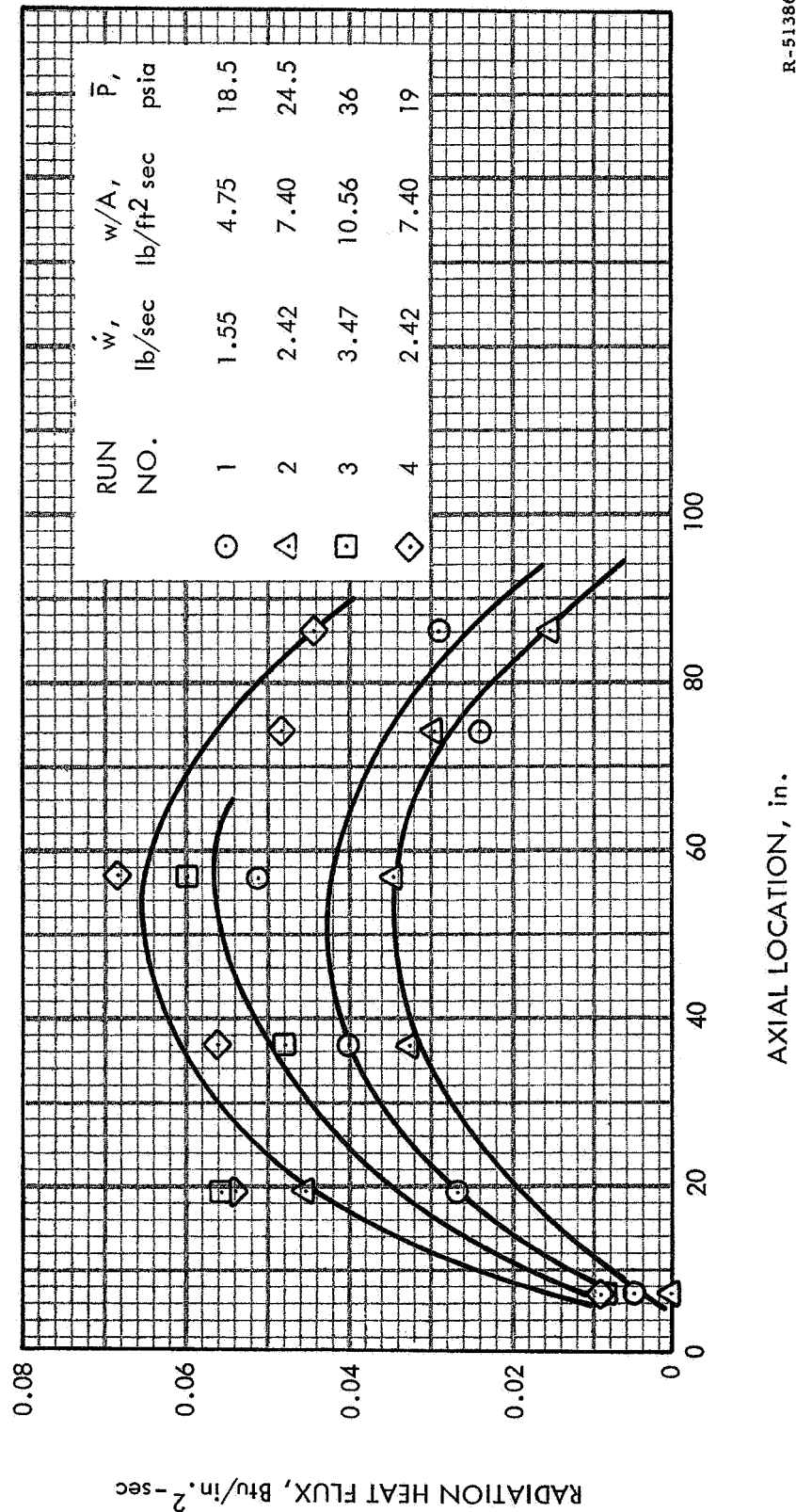
Figure 35.   Radiation Heat Flux, Axial Igniter, Nonaluminized Propellant
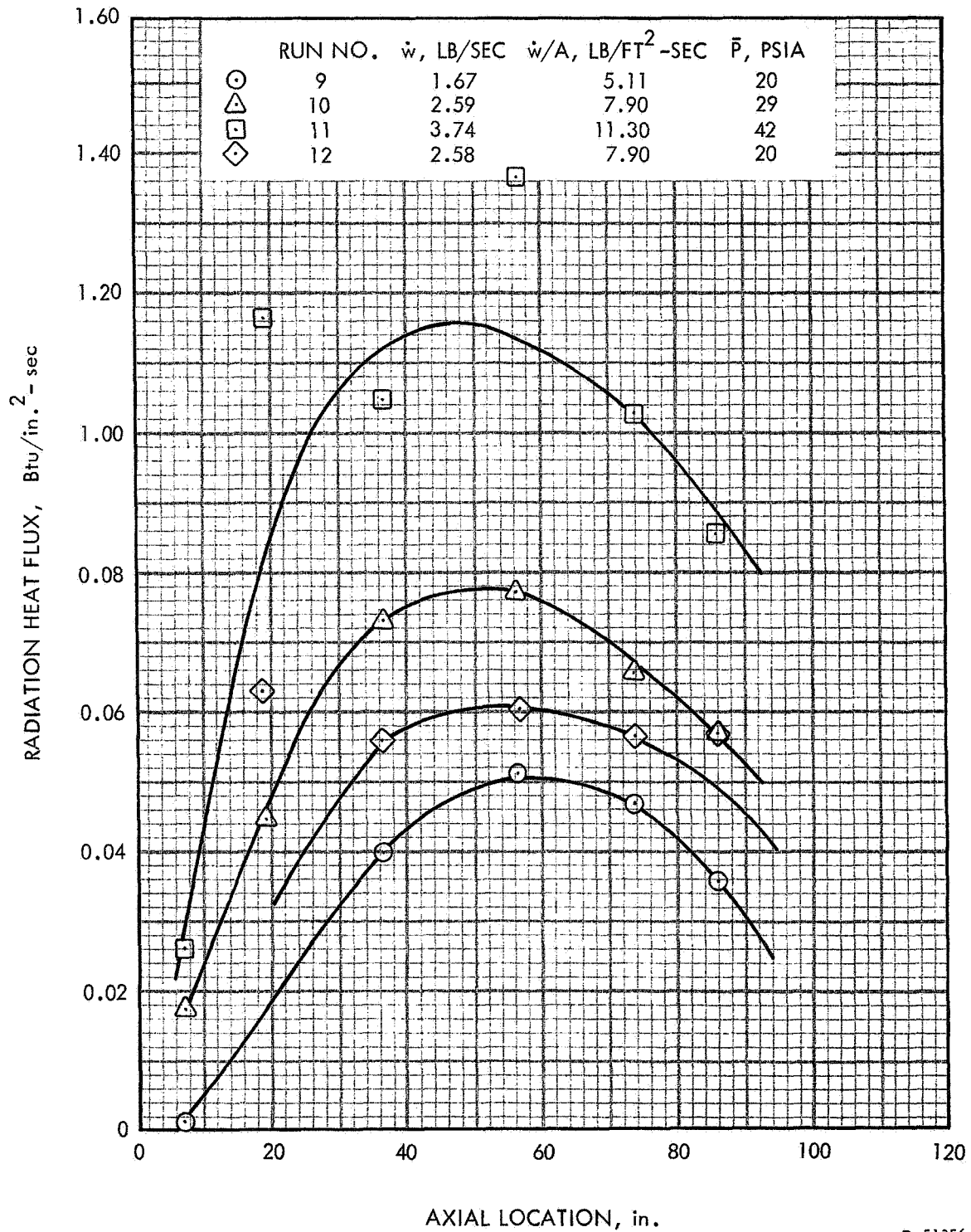
Figure 36. Radiation Heat Flux, Axial Flow, Head-End
Igniter, Aluminized Propellant
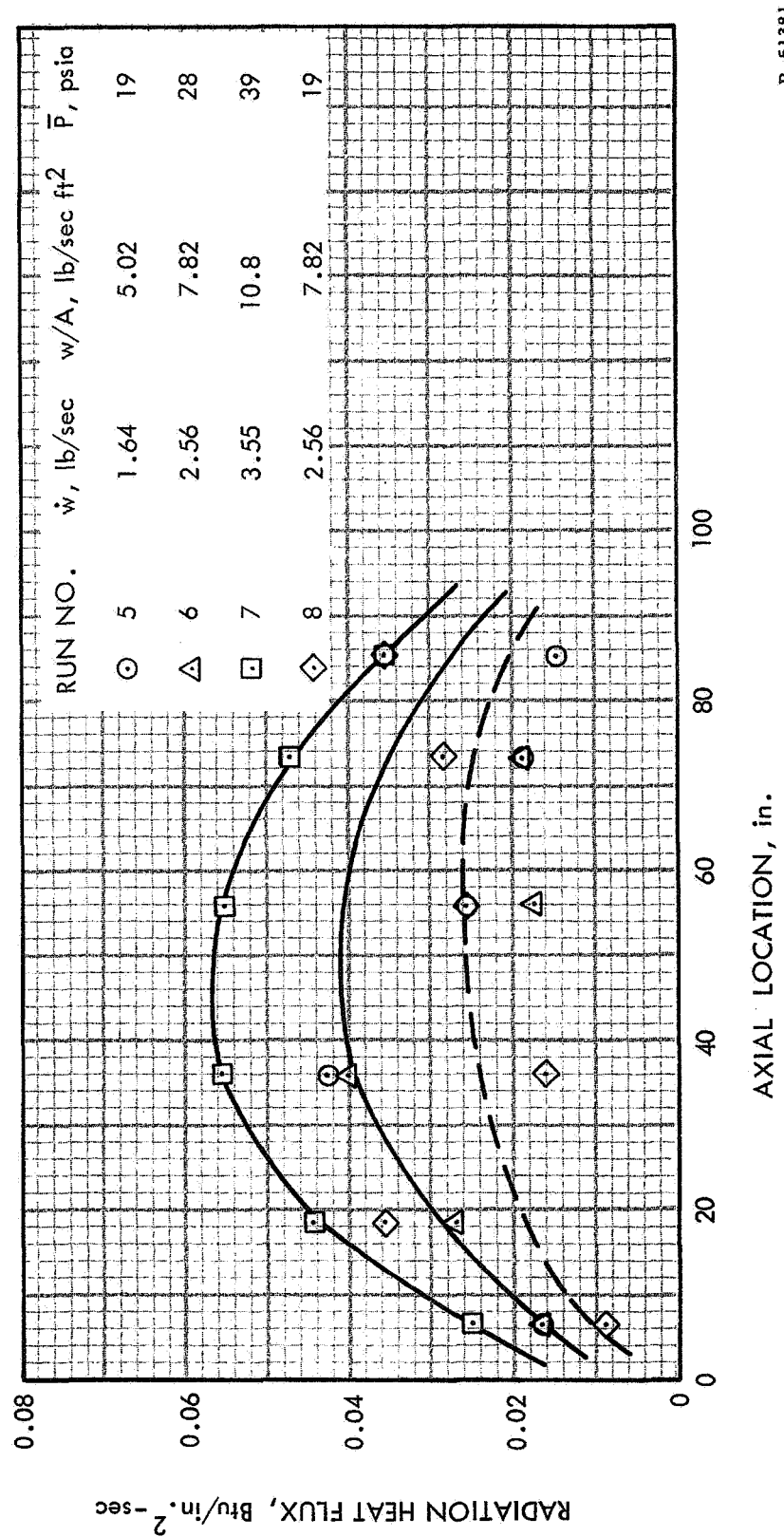
Figure 37. Radiation Heat Flux, Canted Head-End Igniter, Nonaluminized Propellant
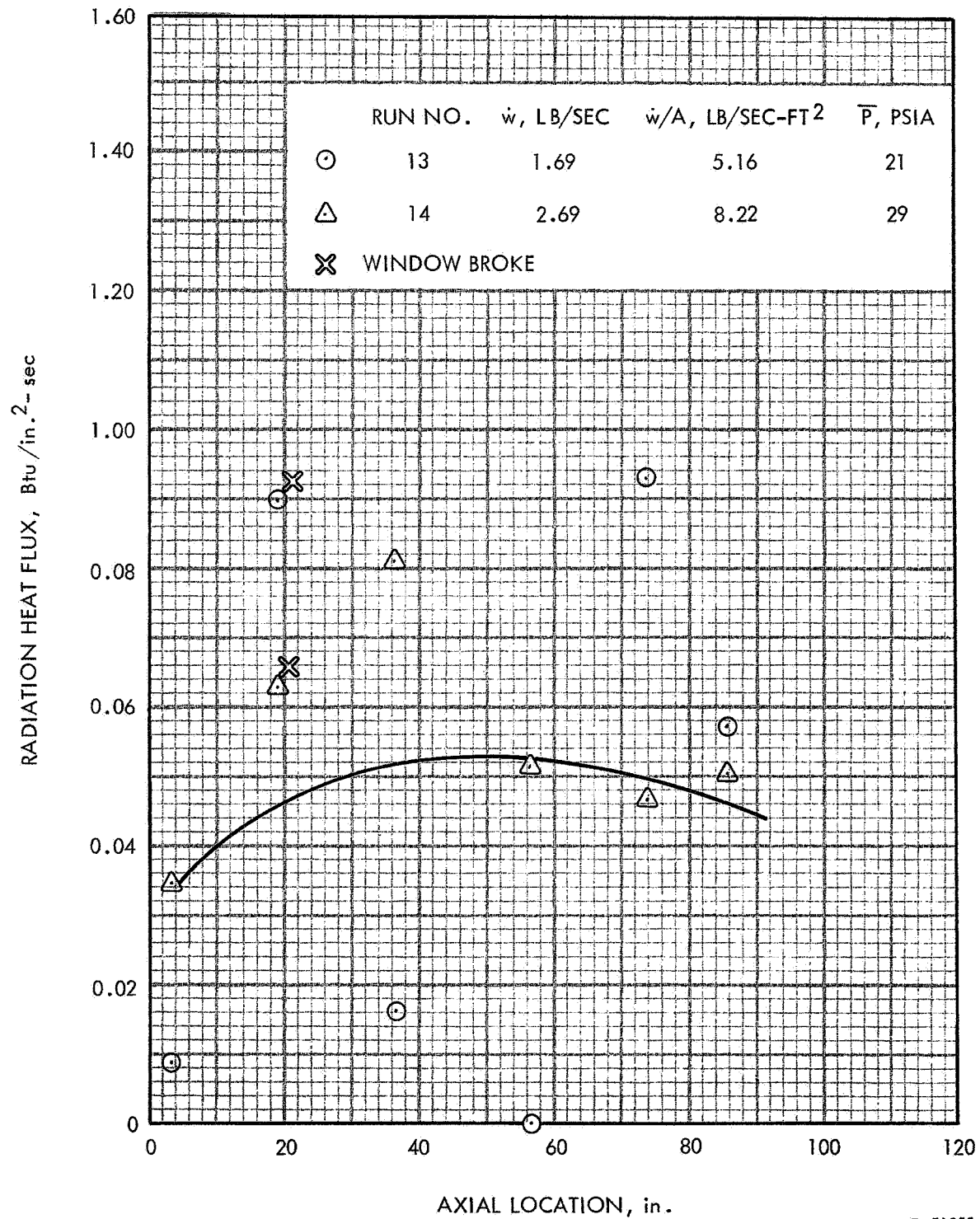
Figure 38. Radiation Heat Flux, Canted Head-End Igniter, Aluminized Propellant
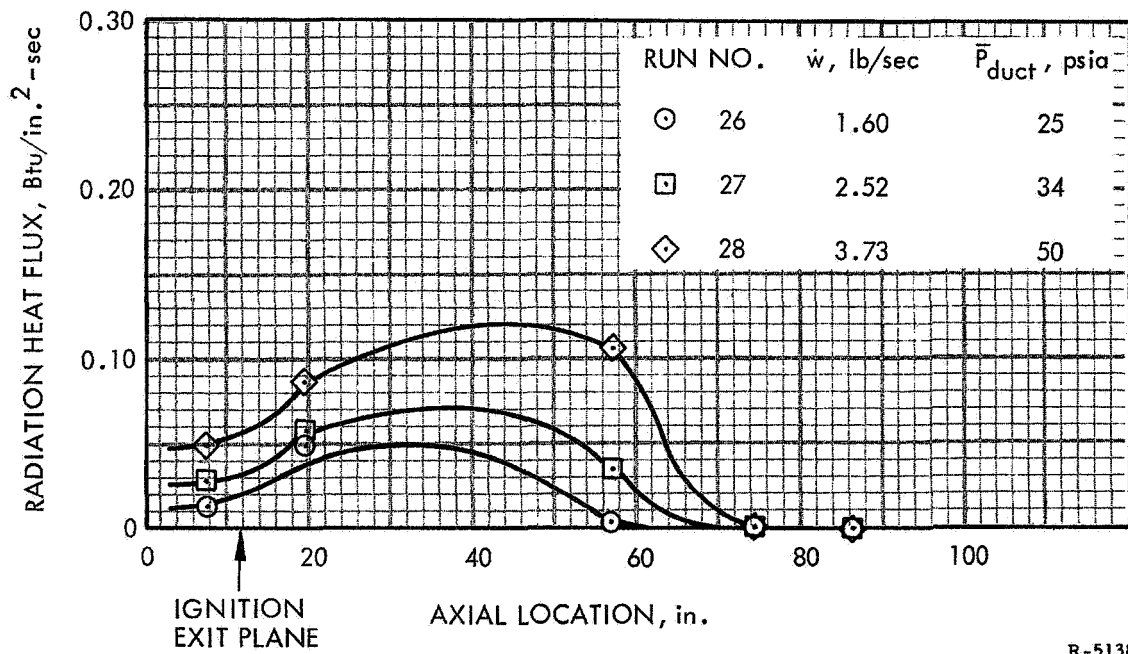
Figure 39. Radiation Flux, Aft Igniter, Aluminized Propellant
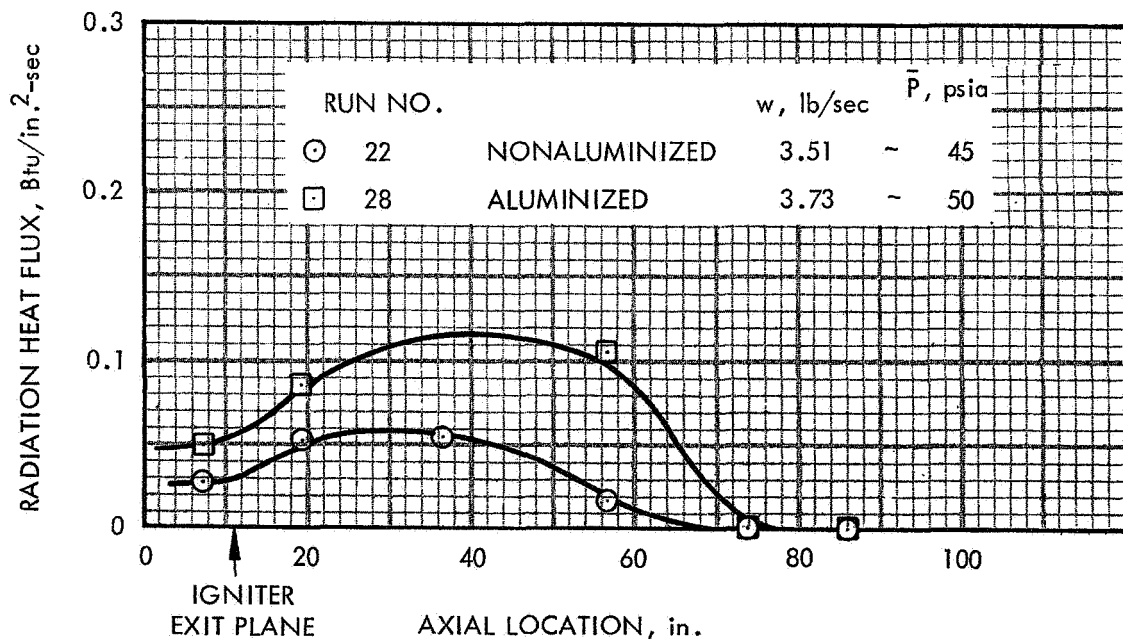
Figure 40. Aft Igniter, Supersonic Jet Radiation Flux
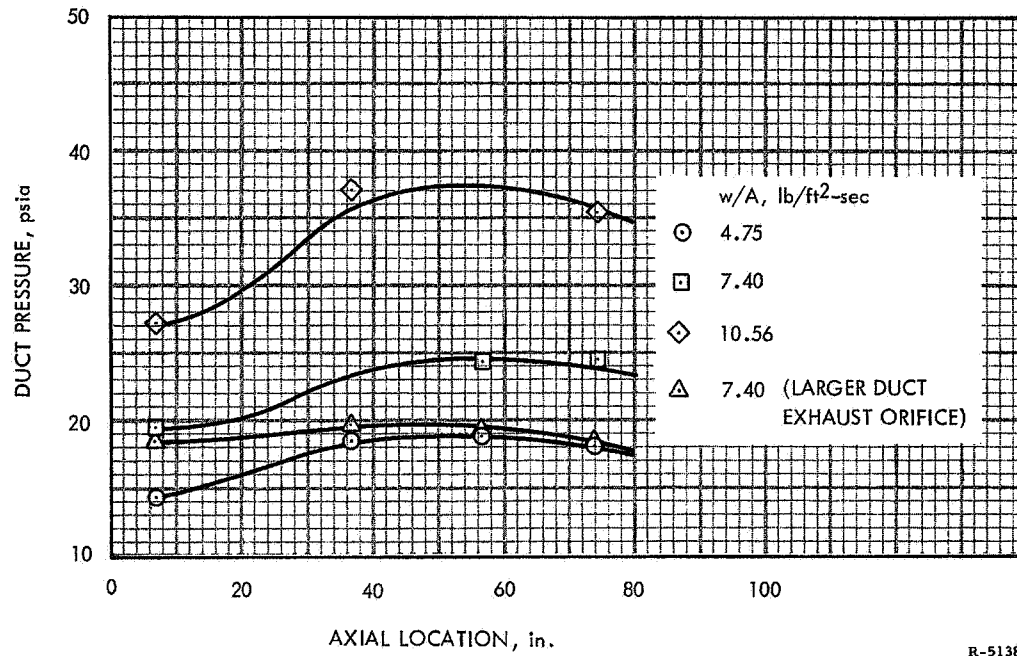
Figure 41. Axial Head-End Igniter Nonaluminized Propellant Duct Pressure
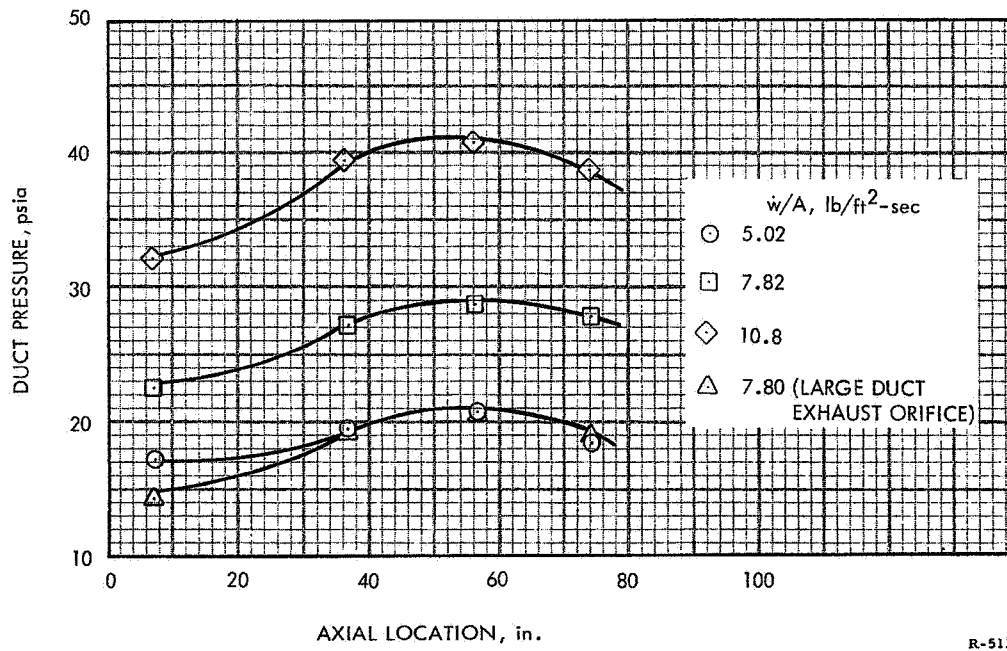
Figure 42. Multiple-Port Canted Igniter, Nonaluminized Propellant,
Duct Pressure
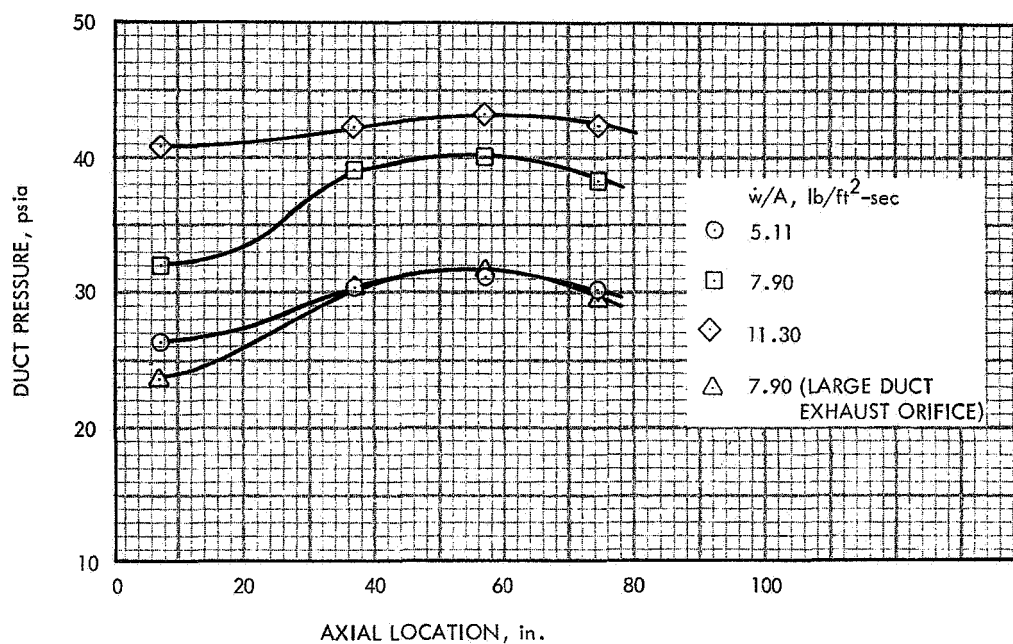
Figure 43. Axial Head-End Igniter, Aluminized
Exhaust (18.9% Al_2O_3), Duct Pressure
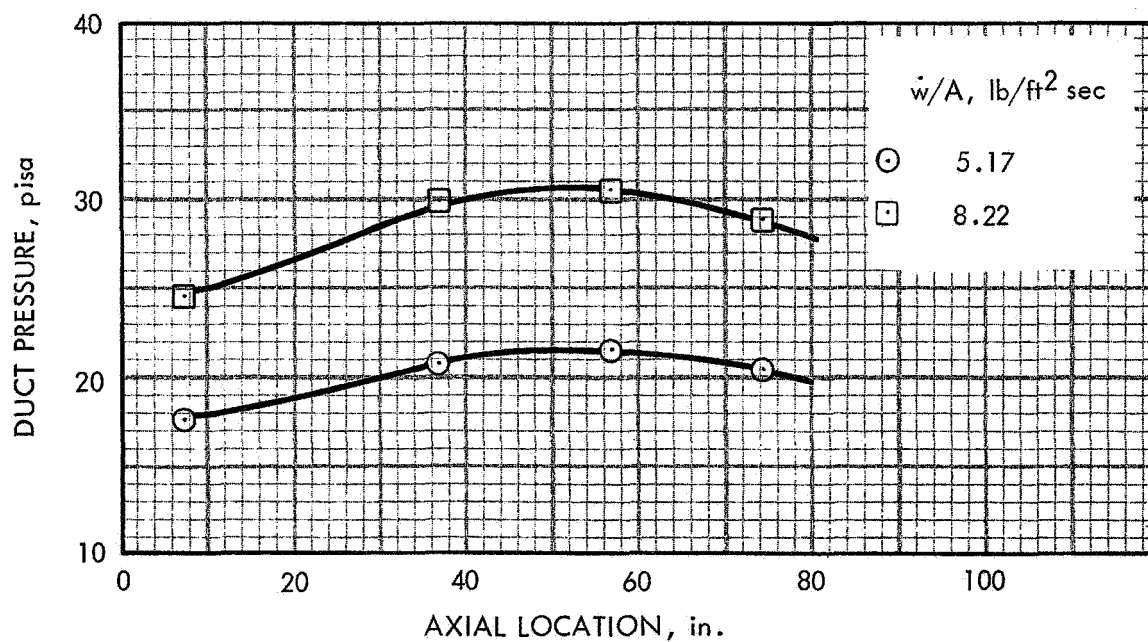
R-51380

Figure 44. Multiple-Port Canted Igniter, Aluminized
Propellant (18.9% Al_2O_3), Duct Pressure

5.0 DISCUSSION

The convective and radiative heat transfer are compared with theoretical models for the case of an axial igniter producing full flow in a duct. The flow is assumed to be highly turbulent as it leaves the impingement region. At the impingement point hydrodynamic and thermal boundary layers are started. The initial development of the boundary layer is strongly influenced by jet spreading. A complete analysis of the impingement zone for axial and canted igniters must therefore wait until the jet mixing problem is resolved.

Starting slightly beyond the mixing zone, however, a sufficiently simplified flow situation emerges so that existing information may be employed with only slight modifications. Kays[13] has obtained a series solution for the thermal entry length of fluids flowing in circular tubes. His general equation, for both laminar and turbulent flow, is:

$$Nu_x = \frac{\sum_n G_n e^{-\lambda_n^2 x^+}}{2 \sum_n \frac{G_n}{\lambda_n^2} e^{-\lambda_n^2 x^+}} \tag{1}$$

where G_n and λ_n^2 are constants and eigen values depending on whether the flow is laminar or turbulent and on the Prandtl and Reynolds numbers. These quantities have been calculated and are listed in reference 6 for $n = 0, 1, 2$. The quantity x^+ is the nondimensionalized axial location:

$$x^+ = \frac{\frac{x'}{r}}{Re\ Pr}$$

In this equation x' is to be measured from the flow starting point. For the data correlation contained herein, $x' = 0$ was assumed to be the axial location where the maximum heat flux was measured. For design calculations, the igniter exhaust attachment point should be used for the starting point ($x' = 0$). A mixing zone analysis method for underexpanded

axisymmetric jets is required so that this point may be predicted. To date this analysis method has not been devised. The results of equation 1 are plotted in figure 45 for the values of Reynolds and Prandtl numbers listed below:

$$Re = 7 \times 10^4, \; 11 \times 10^4, \; 14 \times 10^4$$

$$Pr = 0.84 \; \text{for} \; \gamma = 1.18. \; (\text{Reference 14})$$

Simultaneously with the development of the thermal boundary layer there is a developing momentum or hydrodynamic boundary layer. Kays[13] suggests a simple expression for the average Nusselt number in the developing momentum boundary layer:

$$\frac{Nu_m}{Nu_\infty} = 1 + \frac{C}{\frac{x'}{D}} \; . \tag{2}$$
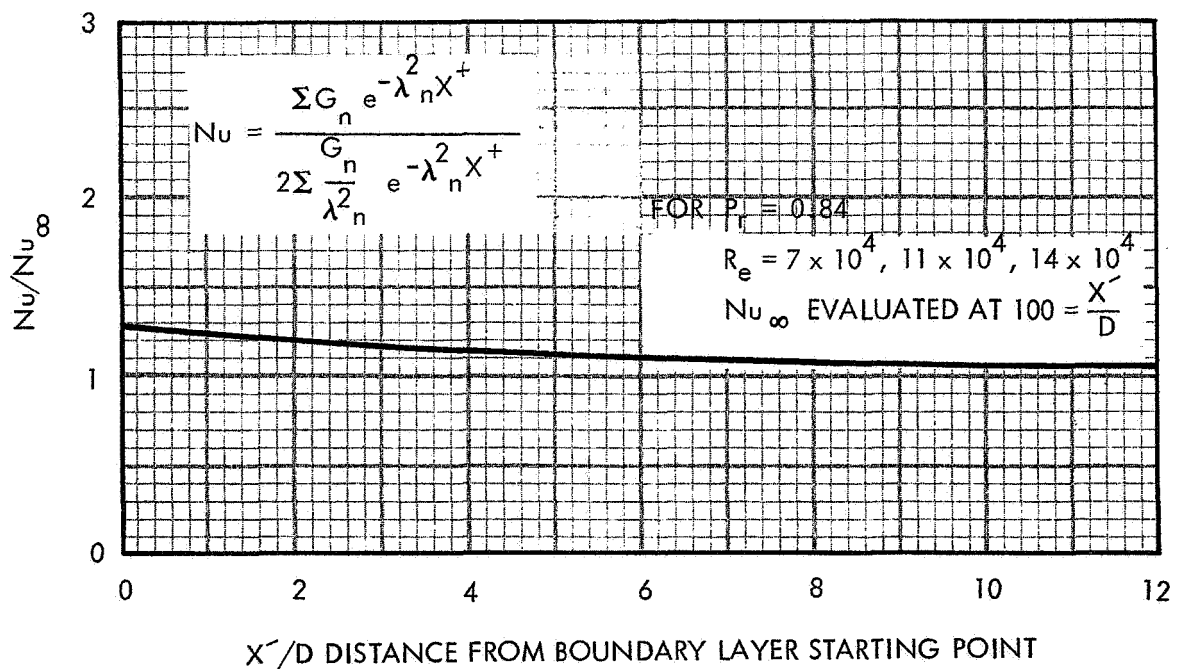
Figure 45. Nusselt Number Ratio (Local: Fully Developed)
for Thermal Entry Length Solution

A similar expression has been found to adequately represent the local Nusselt number of the developing hydrodynamic boundary layer. An additional factor is required to account for the effects of the development of the thermal boundary layer. The resulting expression is stated as:

$$\frac{Nu_x}{Nu_\infty} = \left(\frac{Nu_x}{Nu_\infty}\right)_{thermal} \cdot \qquad (3)$$

From the experimental data the constant C was determined to be 2. 0. The quantity $(Nu_x/Nu_\infty)_{thermal}$ is determined from equation 1 where Nu_∞ is evaluated at 100 diameters. The thermal starting point, discussed above, is assumed to be at the point of maximum heat transfer $x'/D = 0$ at $X/D = 1.9$. Equation 3 is plotted in figure 46 along with all of the average heat transfer data obtained from the head-end axial igniter, using both aluminized and nonaluminized propellants. The value of Nu_∞ used in the experimental data is determined from the Colburn[15] correlation equation for a fully developed turbulent boundary layer with large ΔT:

$$St\,(Pr)^{\frac{2}{3}} = 0.023\,Re^{-.2}$$

and from definitions;

$$Nu = \frac{Pr\,St}{Re} \cdot$$

A local Nusselt number was evaluated from the experimental data by use of the following assumptions:

A. The radiation heat transfer may be subtracted directly out of the total heat flux to obtain convective flux.

B. The heat transfer driving potential (temperature difference) is determined by making heat balances at axial stations and accounting for the gas temperature drop due to energy loss to the duct.

C. Transport properties are determined by the equations of Bartz.[14]
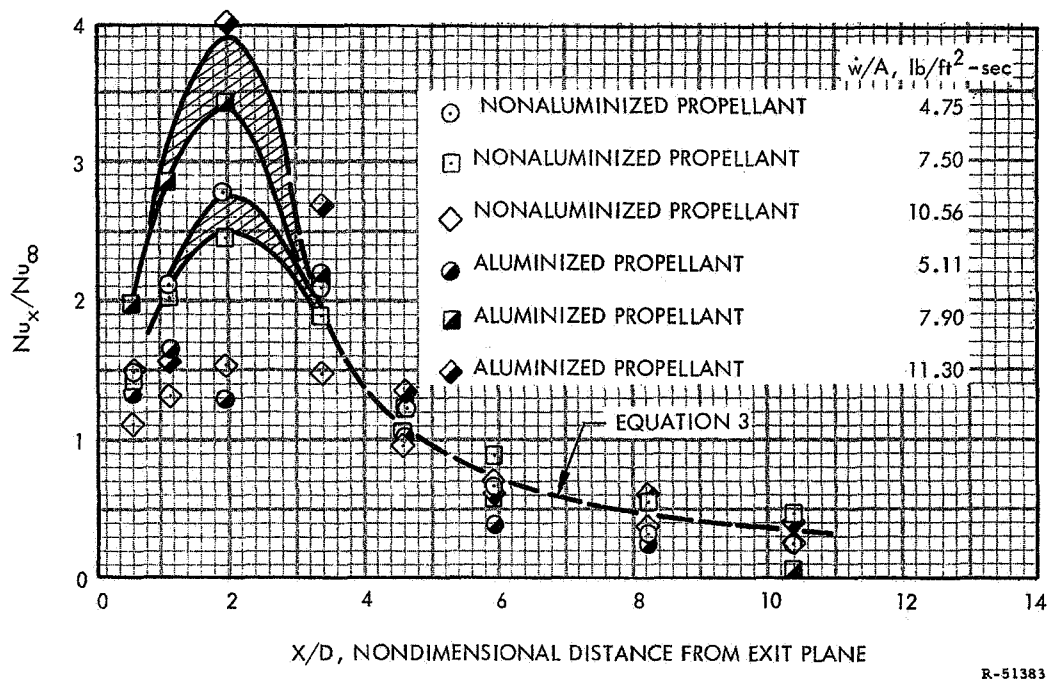
Figure 46. Axial Variation in Heat Transfer Coefficient,
Axial Head-End Igniters

The correlation (figure 47) is seen to be good from 4 diameters downstream of the nozzle exit plane onward. Between 3 and 4 diameters equation 3 adequately represents most of the data and it is questionable whether the discrepancies are phenomenological or due to data scatter. Between the impingement point (1. 9 diameters) and 3 diameters, the presence of the alumina seems to be controlling the heat transfer (shaded zones). At locations nearer the exit plane than 1. 9 diameters, the jet mixing zone has probably not approached the wall and considerable data scatter may be expected.

. A successful correlation of the heat transfer data under the impinging canted jet has not yet been worked out. It is believed that utilization of the jet mixing work suggested earlier, plus an extension of the work of Schauer and Eustis[16] to a three-dimensional stagnation zone will provide an adequate basis for correlating the results of the multiple-port canted igniters.

Very little analytical work has been accomplished in this program on the aft igniter. Reference 17 proposes work which should be undertaken in this area.
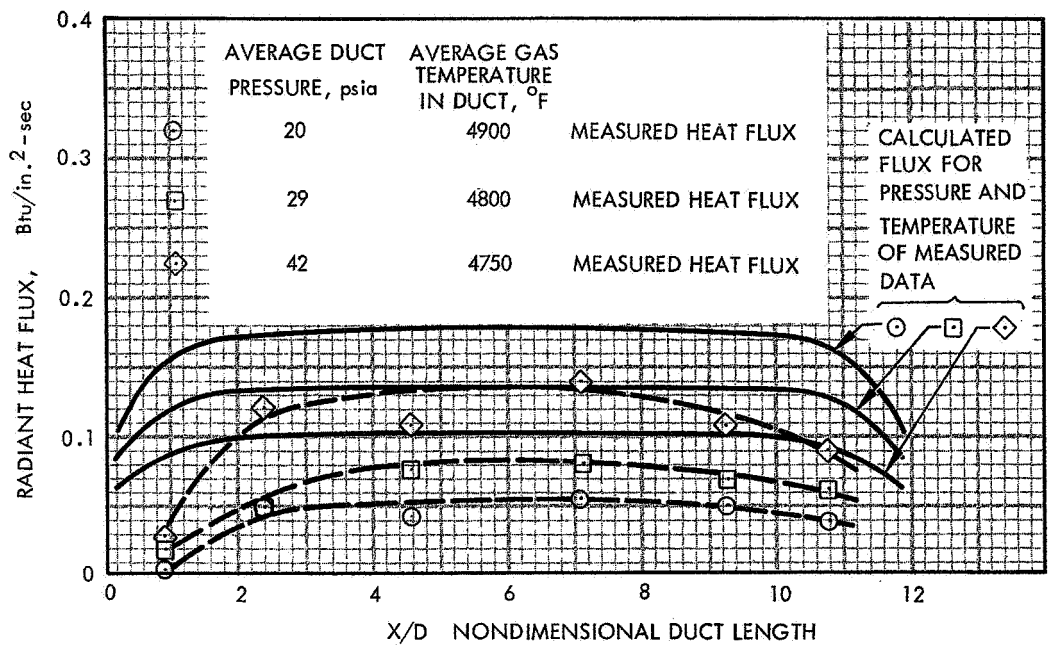
Figure 47. Comparison of Predicted and Measured Radiation Heat Flux, Head-End Axial Igniter, Aluminized Propellant

Radiation heat transfer is predicted from the information presented in appendix B for a series of head-end igniter runs in which the average duct pressure varied from 20 to 42 psia. The calculated values are shown in figure 47 along with data obtained from the radiation calorimeters. The calorimeter data is from 50% to 80% of the predicted value in regions where a reasonably uniform gas temperature may be expected. Since the trend of the data appears to be correct, it is concluded that the view that the sensing element has of the radiating cloud is partially restricted. Postfire examination of the calorimeters showed a sooty deposit on each window in spite of the gaseous nitrogen purge system. It was at first hypothesized that the clouding of the windows had occurred continuously over the igniter firing duration and that reading the data only during the early part of the test would give sufficiently accurate results. It now appears that there was probably a very sooty cloud upon initiation of the igniter due to the fast burning boron/potassium nitrate pellets, and that the nitrogen purge system was not able to keep up with the imposed demands. Before these calorimeters are again used in the copper duct, the nitrogen system will be improved to supply a greater flow rate.

Also the calorimeters will be altered to have a greater view angle since a portion of the radiation incident on an elemental wall area is never received by the radiometer.

All of the errors discussed above are cumulative and cause a reduction in measured radiation flux below the predicted value.

6.0 CONCLUSIONS AND RECOMMENDATIONS

Several significant conclusions may be drawn from the work done in this research program. Some of the more apparent conclusions, along with recommendations for areas of future study, are listed below:

A. In motors utilizing head-end igniters, convective heat transfer to the propellant downstream of the igniter jet impingement zone may be calculated by considering simultaneously developing hydrodynamic and thermal boundary layers. This heat transfer is independent of alumina content in the igniter gases.

B. Radiation heat transfer to a surface element may be estimated by calculating the emissivity of the gas cloud. This involves integrating the absorption equation over the cylindrical volume for each surface element.

C. Convective and radiative heat transfer downstream of the impingement zone may be separated and the components dimensionally scaled to estimate the total heat transfer for new designs using head-end igniters.

D. Heat transfer in the stagnation and impingement zones requires a more precise knowledge of the turbulent mixing process for free and ducted axisymmetric hot jets.

E. The propellant erosion rate under the stagnation zone of multiple-port canted igniters may exceed the propellant burning rate. More work in this area should be done to determine more precisely the erosion rates and the controlling parameters.

7.0 REFERENCES

1. Barrer, M., A. Jaunotte, and J. Vandenkerckhore, Rocket Propulsion. New York: Elsevier Publishing Company, 1960. p. 242.

2. Anderson, R., R. S. Brown, G. T. Thompson, and R. W. Ebeling, "Theory of Hypergolic Ignition of Solid Propellants," presented at the Palm Beach Meeting of the American Institute of Aeronautics and Astronautics, December 1963.

3. "Fundamental Investigation of Hypergolic Ignition for Solid Propellants (U)," Final Report under Contract NOw 62-1006-c. United Technology Center, December 1963. (CONFIDENTIAL)

4. Anderson, R., R. S. Brown, and L. J. Shannon, "Theory of Ignition of Solid Propellants," presented at the American Institute of Aeronautics and Astronautics Solid Propellant Rocket Conference, Palo Alto, California, January 1964.

5. Baer, A. D., and N. W. Rayan, "Ignition of Composite Propellant by Low Radiant Fluxes," presented at the American Institute of Aeronautics and Astronautics Solid Propellant Rocket Conference, Palo Alto, California, January 1964.

6. "Studies in Ignition and Flame Propagation of Solid Propellants," First Semiannual Report under NASA Contract NAS 7-329. United Technology Center, May 1965.

7. Fullman, C. H. et al., "Theoretical and Experimental Investigations of Ignition Systems for Very Large Solid-Propellant Motors (U)," Final Report UTC 2012-FR, Contract No. AF 04(611)-7559. United Technology Center, 1963. (CONFIDENTIAL)

8. Mullis, B. G., "Heat Transfer Studies of Solid Rocket Igniters." Fifth Monthly Progress Report, UTC 2096-MP5, 15 February 1965.

9. Lai, W., "Abort System Mission Effects of Saturn (Radiation Heat Transfer from Rocket Exhausts)" Final Report UTC 2105-FR September 1965.

10. Mullis, B. G., "Heat Transfer Studies of Solid Rocket Igniters," Seventh Monthly Progress Report, UTC 2096-MP7, 15 May 1965.

11. Lewis, C. H. Jr., and D. J. Carlson, "Normal Shock Location in Underexpanded Gas and Gas Particle Jets," AIAA J., (2) 776-777 (1964).

12. Love, E. S. and C. E. Grigsby, "Some Studies of Axisymmetric Free Jets Exhausting from Sonic and Supersonic Nozzles into Still Air and into Supersonic Streams." NACA RML54L31, 10 May 1955.

13. Kays, W. M., "Convective Heat and Mass Transfer." (Lecture Note Series", Stanford University.

14. Bartz, D. R., "A Simple Equation for Rapid Estimation of Rocket Nozzle Convective Heat Transfer Coefficients." Jet Propulsion, (27) 49-51 January 1957.

15. McAdams, W. H., "Heat Transmission" Third Ed. McGraw-Hill Book Company: New York, 1954.

16. Schauer, J. J. and R. H. Eustis, "The Flow Development and Heat Transfer Characteristics of Plane Turbulent Impinging Jets." Technical Report No. 3, Department of Mechanical Engineering, Stanford University. 30 October 1963.

17. United Technology Center Proposal No. 65-61, "Igniter Heat Transfer Studies of Solid Rocket Motors." Technical Proposal. 14 July 1965.

APPENDIX A
ERROR IN THERMOCOUPLE DATA DUE TO LONGITUDINAL
AND CIRCUMFERENTIAL HEAT CONDUCTION IN THE COPPER DUCT

A possible source of error in the thermocouple data produced in the copper duct heat transfer work is longitudinal and circumferential conduction of energy away from locations of very high heat transfer rates. The existence of this error requires the presence of the most unfavorable combination to produce temperature gradients in the tube; that is, all gradients must produce conduction of energy away from the point in question.

The magnitude of the error may be estimated as follows. Assume that a region containing a thermocouple of diameter D in the copper duct is subjected to very high heat transfer as pictured in figure A-1.

By referring to figure A-2, a heat balance is written as follows:

$$q_{absorbed} = q_{stored} + q_{out} \quad .$$
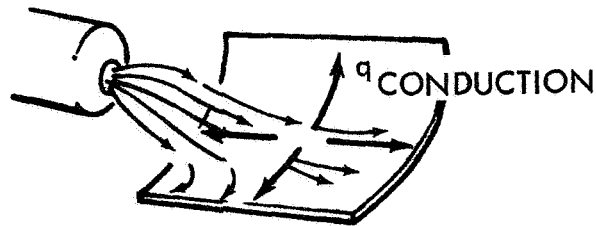
Figure A-1. Heat Transfer in Copper Duct

$$q_{absorbed} = q_{stored} + q_{out}$$
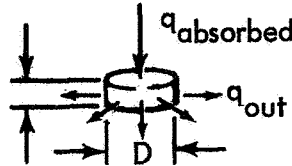
Figure A-2. Heat Balance in Cylindrical Coordinates

A measure of the error involved in the data reduced from this type of experiment is found by comparing the absorbed heat to the heat flux assumed to be correct. Thus:

$$\frac{q_{absorbed}}{q_{stored}} = \frac{q_{stored} + q_{out}}{q_{stored}} = 1 + \frac{q_{out}}{q_{stored}}$$

in which q_{out}/q_{stored} is the subject error. The term q_{out} is determined by the conduction equation:

$$q_{out} = kA \frac{\partial T}{\partial r} = k \pi D \ell \frac{\partial T}{\partial r} \qquad (1)$$

and q_{stored} is determined by the capacity of the element:

$$q_{stored} = \rho c \ell \frac{\pi}{4} D^2 \frac{\partial T}{\partial t} \qquad (2)$$

forming the ratio:

$$\frac{q_{out}}{q_{stored}} = \frac{k \pi D \ell \frac{\partial T}{\partial r}}{\rho c \frac{\pi}{4} D^2 \frac{\partial T}{\partial t}} = \frac{4\alpha}{D} \frac{\frac{\partial T}{\partial r}}{\frac{\partial T}{\partial t}} \cdot \quad (3)$$

For run No. 14 in the copper tube test, the following values were measured at the point of maximum heat flux:

$$\frac{\partial T}{\partial r} = 790° \text{ F/in. (occurs after 250 msec of firing)}$$

$$\frac{\partial T}{\partial r} = 3840° \text{ F/sec (nearly constant over 250 msec of firing) .}$$

The value of D should be approximately equal to the thermocouple spacing since $\partial T/\partial r$ is determined from adjacent thermocouples. Thus, D is approximately 4.0 in. For copper at about 900° F, the thermal diffusivity is approximately 0.16 in.^{2}/sec.

Substitution of numerical values into equation 3 yields:

$$\frac{q_{out}}{q_{stored}} = 0.036$$

or 3.6% error. This magnitude of error is produced only in the runs having the highest heat transfer and is present only in the late stages of the firing. All other conditions are less severe and produce less error.

APPENDIX B

AN ANALYSIS OF THERMAL RADIATION
TO A CYLINDRICAL SOLID PROPELLANT
GRAIN DURING IGNITION

1.0 INTRODUCTION

Ignition of a solid-propellant rocket motor is most reliably accomplished by firing a short-duration, small rocket into the cylindrical bore of the motor. Usually the secondary rocket, or igniter, is designed to operate up to 1 sec at a chamber pressure of 1000 to 2000 psia. The propellant of the igniter is often of the same basic type as the rocket motor. This discussion is concerned with the aluminized composite solid propellant which consists of an oxidizer such as ammonium perchlorate and a fuel and structural binder of some rubber-type polymer and powdered aluminum. The aluminum, usually about 15% by weight, burns to form Al_2O_3 which at the flame temperature of 6000° R is in the form of small droplets and at lower temperatures small solid particles. The mean particle size has been found to be of the order of 3 μ diameter.

The igniter, then, produces an environment inside the motor of a high-velocity, high-temperature gas with about 30% by weight of small particles. Heat transfer by gaseous convection, gaseous and particle radiation, and particle impact heats the solid-propellant grain to a point where its own combustion is self-sustaining (about 1200° R) and ignition has been accomplished.

Each mode of heat transfer must be considered in an analysis of ignition before any can be eliminated. It is the purpose of this appendix to consider, at least approximately, the radiation analysis of ignition by calculating the radiation flux from the solid particles and showing the gaseous radiation from water and carbon dioxide to be small by comparison.

2.0 PROBLEM STATEMENT

Figure B-1 shows a simplified version of a solid rocket motor during ignition. The igniter jet (an exit cone is rarely used) expands as a free jet under a large pressure ratio (p_{ign}/p_c = 50 to 100) and thus the Riemann shock is strong and large.[1]* This almost completely destroys the supersonic structure. Thus, after the Riemann shock, the flow may be considered subsonic.

---

* Superscript numbers denote references appearing on page B-16.
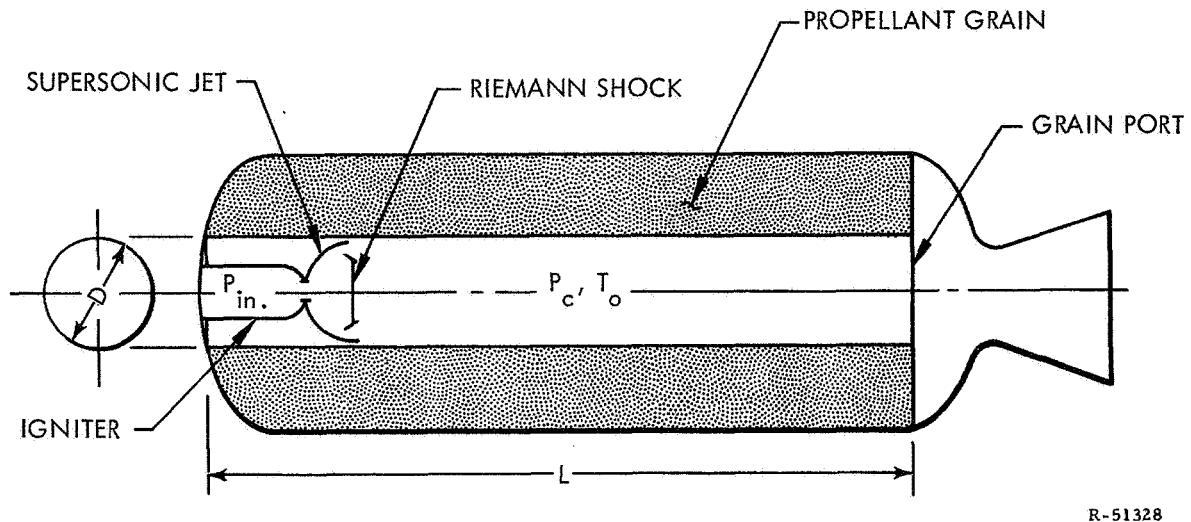
Figure B-1. Solid Rocket Motor During Ignition

If quasi-steady one-dimensional flow is assumed, then continuity of mass will dictate a value of p_c for a given value of p_{ign} assuming the flow adiabatic. (If the flow were adiabatic no ignition would occur, but the ratio of heat flux to the grain to energy flow through is usually small.) Typical values of equilibrium p_c due to igniter mass flow are 50 to 100 psi.

Radiation from the supersonic portion of the flow will be from a much lower temperature and is neglected. Radiation aft of the Riemann shock is assumed to be from the equilibrium pressure, p_c, and from the igniter stagnation temperature (since the Mach number of the subsonic flow is low as seen from typical grain port to nozzle area ratios). Flow behind the igniter will be recirculating subsonic and probably lower in pressure than p_c.

For the purposes of analysis, a cylindrical volume of length L and diameter D will be considered filled with the exhaust products at T_o and p_c. Radiation to the walls will be assumed totally absorbed[2] (ϵ_{rubber} = 0.86 - 0.94) and reradiation neglected since the walls are cold before ignition and not of interest after ignition.

3.0 ANALYSIS

The monochromatic radiant flux per unit time arriving at a unit area of a surface exposed to radiation from a gas above it (the gas emissive power) is given by:[3]

$$e_\lambda = \int i_\lambda \, dw \tag{1}$$

where dw is a differential solid angle looking into the gas from dA, and i_λ is the monochromatic radiation intensity, as shown in figure B-2. Thus:

$$i_\lambda = \epsilon_{\lambda,\beta} \, i_{b_\lambda} \tag{2}$$
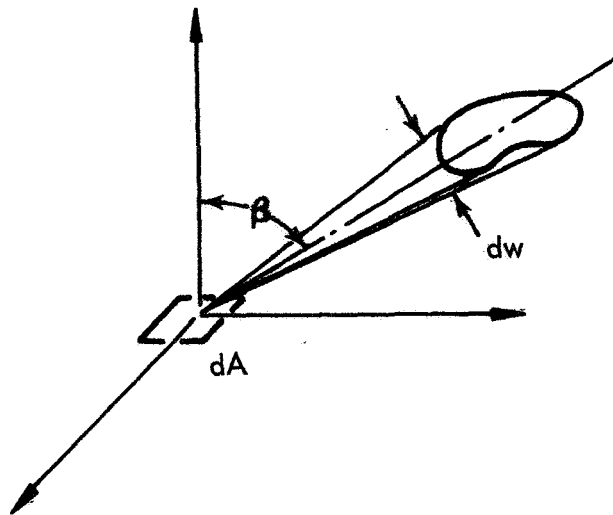

Figure B-2. Elemental Area and Solid Angle

where $\epsilon_{\lambda,\beta}$ = monochromatic emissivity of the gas for direction β

i_{b_λ} = monochromatic intensity of a black body for direction β .

If Kirchhoff's law is to hold, then:

$$\epsilon_{\lambda,\beta} = \alpha_{\lambda,\beta} = \left(1 - e^{-a_\lambda s}\right) \qquad (3)$$

where $\alpha_{\lambda,\beta}$ = monochromatic gas absorptivity for direction β

a_λ = absorption coefficient

s = gas depth in direction β.

Using Plank's law we obtain:

$$i_{b_\lambda} = \cos \beta \ \frac{C_1}{\lambda^5 \left(e^{C_2/\lambda T} - 1\right)} \qquad (4)$$

where $C_1 = 1.1905 \times 10^{-5}$ erg cm^2/sec

$C_2 = 1.4387$ cm - °K

λ = wave length

T = temperature.

Thus, by combining equations 1, 2, 3, and 4 we obtain:

$$e_\lambda = \int \frac{C_1 \cos\beta \left(1 - e^{-a_\lambda s}\right) dw}{\lambda^5 \left(e^{C_2/\lambda T} - 1\right)} \qquad (5)$$

Figure B-3 shows the limits of integration of equation 5.

Note that because of symmetry, the angle β is found to be the angle between line S and the inward normals of both dA and dA':

$$dw = \frac{dA' \cos \beta}{S^2} \qquad (6)$$

$$dA' = rd\,\xi\,d\,\psi \ . \qquad (7)$$
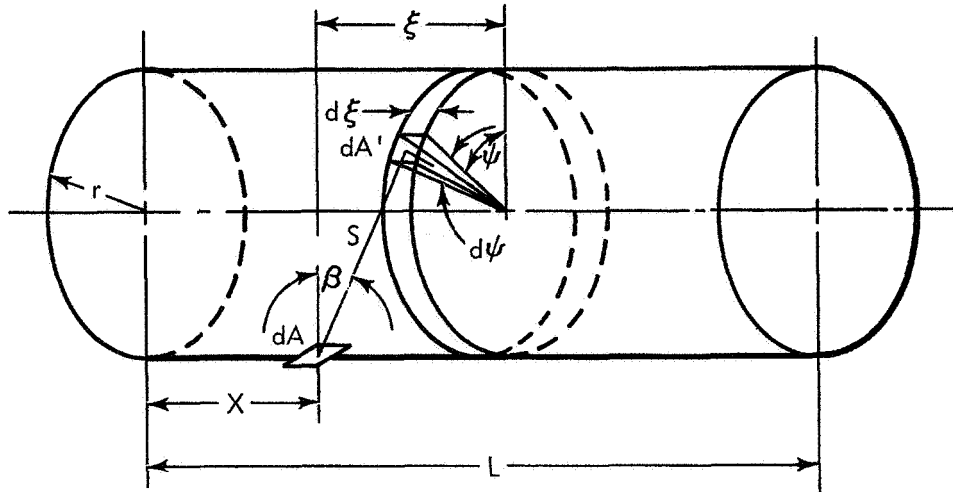
R-51327

Figure B-3. Integration Model for Equation 5

Also, the emissive power at any station X_1 can be generated from the $X = 0$ solution if e_λ $(X = 0)$ known as a function of ξ since:

$$e_{\lambda, X_1} = e_\lambda \ (\xi = X_1) + e_\lambda \ (\xi = L - X_1) \qquad (8)$$

and e_λ will hereafter represent the $X = 0$ solution.

Straighforward trigonometric operations result in:

$$\cos \beta = \frac{r}{s} \ (1 + \cos \psi) \qquad (9)$$

$$s^2 = \xi^2 + 2r^2 \ (1 + \cos \psi). \qquad (10)$$

Substitution into equation 5 yields:

$$e_\lambda(\xi') = 2 \int_{\psi=0}^{\psi=\pi} \int_{\xi=0}^{\xi=\xi'} \frac{C_1}{\lambda^5 \left(e^{C_2/\lambda T} - 1\right)} \frac{\left\{1 - e^{-a_\lambda \left[\xi^2 + 2r^2 (1 + \cos \psi)\right]^{\frac{1}{2}}}\right\}}{\left[\xi^2 + 2r^2 (1 + \cos \psi)\right]^2}$$

$$(1 + \cos \psi)^2 \, d\xi' \, d\psi \quad (11)$$

and

$$e(\xi') = 2 \int_{\psi=0}^{\psi=\pi} \int_{\xi=0}^{\xi=\xi'} \int_{\lambda=0}^{\lambda=\infty} \left\{ \frac{C_1}{\lambda^5 \left(e^{C_2/\lambda T} - 1\right)} \right\}$$

$$\frac{\left\{1 - e^{-a_\lambda \left[\xi^2 + 2r^2 (1 + \cos \psi)\right]^{\frac{1}{2}}}\right\}}{\left[\xi^2 + 2r^2 (1 + \cos \psi)\right]^2} (1 + \cos \psi)^2 \, d\lambda \, d\xi \, d\psi. \quad (12)$$

The form of a_λ is needed to proceed. The variation of a_λ with λ for Al_2O_3 particles from a solid propellant is not known and is currently under study in several areas.[4] Reference 3 discussed data for soot particles where it is concluded that a_λ varies with λ and "was representable by $K/\lambda^{0.95}$ in the infrared region down to $0.8\ \mu$." For this gross an assumption, little error is introduced by

$$a_\lambda = \frac{K}{\lambda} \quad (13)$$

This form is particularly desirable since it yields a closed-form integral over λ in equation 12 (using Wien's law).

Consider only the λ integral:

$$I_1 = \int_{\lambda=0}^{\lambda=\infty} \left\{ \frac{C_1}{\lambda^5 \left(e^{C_2/\lambda T} - 1\right)} \right\} \left\{ 1 - e^{-\frac{K}{\lambda} s} \right\} d\lambda \quad (14)$$

$$I_1 = \int\limits_{\lambda=0}^{\lambda=\infty} \frac{C_1}{\lambda^5 \left(e^{C_2/\lambda T} - 1\right)} \, d\lambda - \int\limits_{\lambda=0}^{\lambda=\infty} \frac{C_1 e^{-\frac{K_S}{\lambda}}}{\lambda^5 \left(e^{C_1/\lambda T} - 1\right)} \, d\lambda \quad . \tag{15}$$

Wien's law for the temperatures under consideration is sufficiently accurate and:

$$I_1 \cong \int\limits_{\lambda=0}^{\lambda=\infty} \frac{C_1}{\lambda^5 \, e^{C_2/\lambda T}} \, d\lambda - \int\limits_{\lambda=0}^{\lambda=\infty} \frac{C_1}{\lambda^5 \left(e^{1/\lambda \, (C_2/T + K_S)}\right)} \, d\lambda . \tag{16}$$

The second integral is identical in form to the first whose integral is known. [3] Thus:

$$\int\limits_{\lambda=0}^{\lambda=\infty} \frac{C_1}{\lambda^5 \left(e^{C_2/\lambda T}\right)} \, d\lambda \cong \frac{\pi^4 C_1}{15 \, C_2^4} \, T^4 = \frac{\sigma}{\pi} \, T^4 \tag{17}$$

and

$$\int\limits_{\lambda=0}^{\lambda=\infty} \frac{C_1}{\lambda^5 \left(e^{1/\lambda \, (C_2/T + K_S)}\right)} \, d\lambda \cong \frac{\pi^4 C_1}{15 \, C_2^4} \, \frac{T^4}{\left(1 + \dfrac{K_S T}{C_2}\right)^4} \quad . \tag{18}$$

Substituting equations 17 and 18 into equation 16 yields:

$$I_1 = \frac{\sigma T^4}{\pi} \left\{ 1 - \left(1 + \frac{K_S T}{C_2}\right)^{-4} \right\} . \tag{19}$$

Substitute equation 19 into equation 12 and define the "partial emissivity" as the ratio of $e(\xi')$ to $e_b = \sigma T^4$. The term partial is used to call attention

to the fact that $e(\xi')$ is for $\xi'>0$ and if one allowed $\xi' \rightarrow \infty$ and $r \rightarrow \infty$ in equation 12, $e \rightarrow 1/2\ e_b$. This is exactly as it should be since $e = e_b$ for the whole space integral. From equation 8 (integrated over λ):

$$\lim_{\substack{\xi \rightarrow \infty \\ r \rightarrow \infty}} e_{,x_1} = 2 \lim_{\substack{\xi \rightarrow \infty \\ r \rightarrow \infty}} e$$

$$= e_b \ .$$

Thus:

$$\epsilon' \equiv \frac{e(\xi')}{\sigma T^4} = \frac{2r^3}{\pi} \int_{\psi=0}^{\psi=\pi} \int_{\xi=0}^{\xi=\xi} \left[1 - \left\{ 1 + \frac{KT}{C_2} \left[\xi^2 + 2r^2 (1 + \cos \psi) \right]^{\frac{1}{2}} \right\}^{-4} \right] \cdot$$

$$\frac{(1 + \cos \psi)^2}{\left[\xi^2 + 2r^2 (1 + \cos\psi) \right]^2} \, d\xi \, d\psi \quad . \quad (20)$$

Letting $\qquad u \equiv \dfrac{\xi'}{r}$:

$$\epsilon'(u) = \frac{2}{\pi} \int_{\psi=0}^{\psi=\pi} \int_{u=0}^{u=\frac{\xi'}{r}} \left[1 - \left\{ 1 + \frac{KTr}{C_2} \left[u^2 + 2 (1 + \cos \psi) \right]^{\frac{1}{2}} \right\}^{-4} \right] \cdot$$

$$\frac{(1 + \cos \psi)^2}{\left[u^2 + 2 (1 + \cos \psi) \right]^2} \, du \, d\psi \quad . \quad (21)$$

At this point the integration was committed to the digital computer, the Burroughs B 5500, using a summation approximation:

$$\epsilon'(u) \cong \frac{2}{\pi} \sum_{i=1}^{N} \sum_{j=1}^{M} \left[1 - \left\{ 1 + \frac{KTr}{C_2} \left[u_i^2 + 2 (1 + \cos \psi_j) \right]^{\frac{1}{2}} \right\}^{-4} \right] \cdot$$

$$\frac{(1 + \cos \psi_j)^2}{\left[u_i^2 + 2 (1 + \cos \psi_j) \right]^2} \, \Delta u \, \Delta \psi \quad (22)$$

where u_i and ψ_j are evaluated at the midpoint of the (i,j) increment.

Note that $\epsilon'(u)$ is not a purely geometric factor since the term KTr/C_2 occurs within the integral. However, scaling of the results can be accomplished by varying K, T, and r such that their product is constant.

Finally, the "apparent emissivity," ϵ, is constructed for cylinder of given L/D for each station X for a given value KTr as:

$$\epsilon\left(\frac{X}{r}\right) = \epsilon'\left(u = \frac{X}{r}\right) + \epsilon'\left(u = \frac{L-X}{r}\right) \tag{23}$$

4.0 RESULTS

To ensure that a range of practical interest was covered in the graphs to be presented, it was necessary to know a representative value of K. This was obtained from solid-propellant free-jet radiation data. From total calorimeter measurements and the instrument's view factor to the jet, the surface emissive power was determined for several 120-in. solid motors. Red-brightness temperature measurements were used to find the jet temperature. These two quantities of emissive power and temperature result in an apparent emissivity. Assuming $a_\lambda = K/\lambda$ and performing an integration similar to equation 22 results in a value for K at the particle concentration of the free jet ($K \cong 3.75 \times 10^{-7}$ at $pj = 14.7$ psia and $T_j = 3500°$ R).

One further assumption is needed:

$$K = Ku' \, n \tag{24}$$

where

Ku' = a constant for a given particle type and size distribution

n = the number density of particles.

Since the propellant composition is constant, continuity requires

$$n \sim \rho$$

where ρ = the local gaseous density and

$$\rho = \frac{p}{RT} \quad .$$

Hence:

$$K = \frac{Ku \; p}{T} \quad . \tag{25}$$

Knowing the pressure and temperature of the jet, Ku was found. Typical values of P_C and T for the igniter were given as P_C = 50 psi and T = 6000° R. The grain bore diameter may range from a few inches to 50 in. The constant KTr was centered at:

$$K = \frac{Ku \; (50 \; psi)}{(6000° \; R)} \quad .$$

The temperature was 6000° R and the diameter was 8 in. and varied above or below to cover cases of practical importance.

A second source of data exists for Ku[5] where throat radiation data were taken as described above. The term Ku from this source is in approximate agreement with the jet data.

Figures B-4 through B-7 are the "apparent emissivities" for cylinders of L/D = 5, 10, 12, and 15 for the values of KTr.
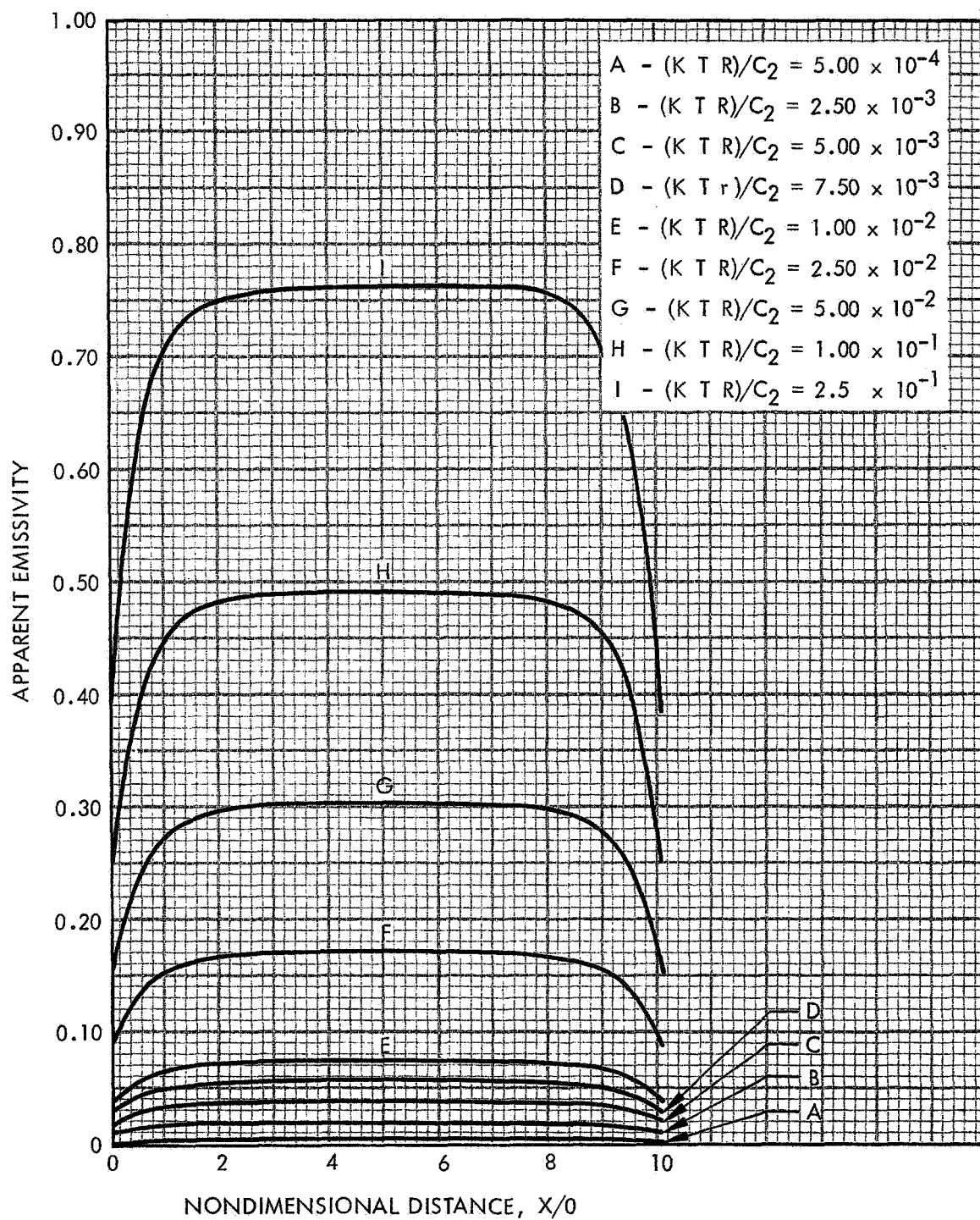
5.0 DISCUSSION

A comparison of the water radiation from this stream can be made with the above results. Let the effective spherical radius be D. Typical water concentrations are 10%, or a partial pressure of:
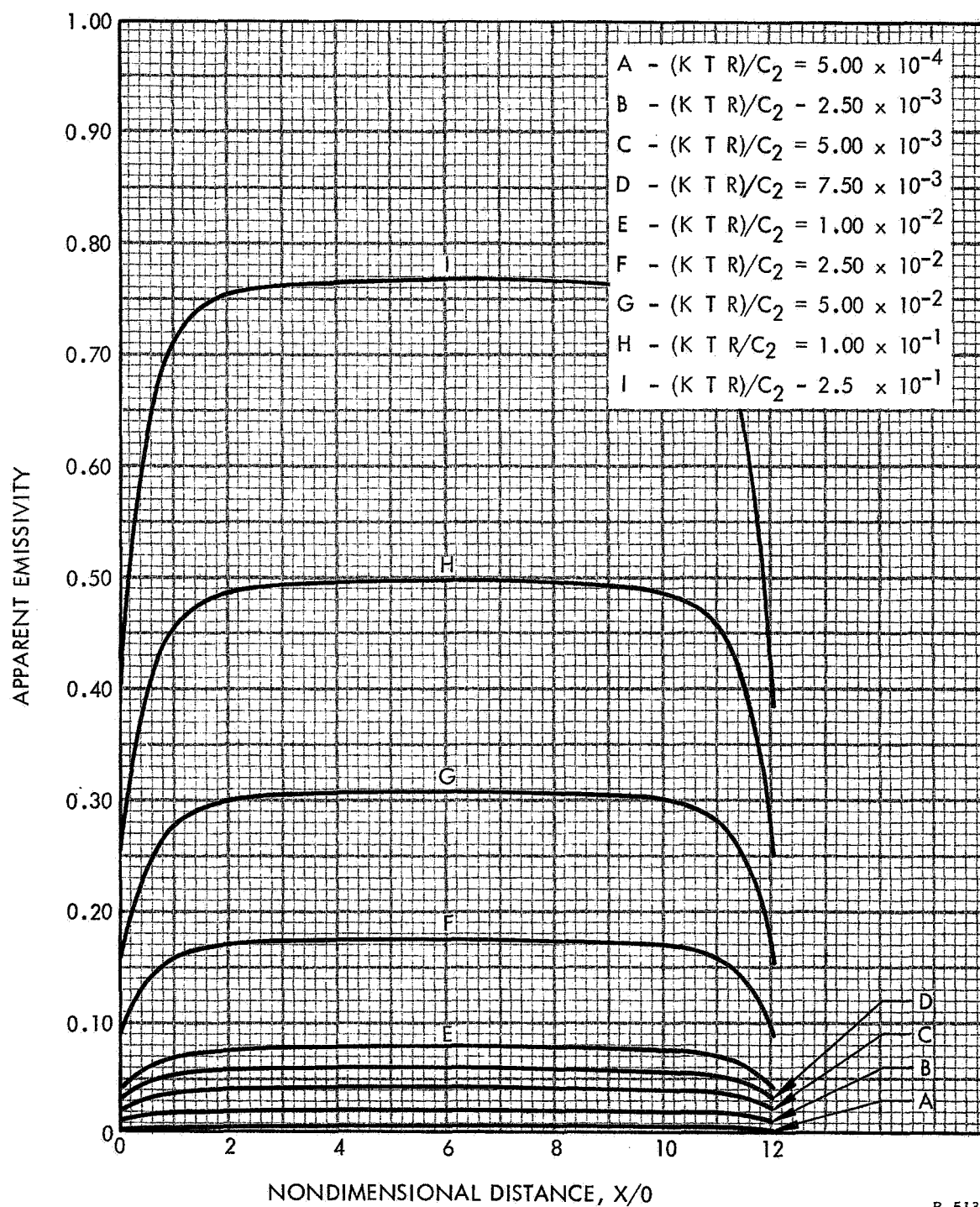
$$P_{H_2O} = 0.1 \; P_c$$
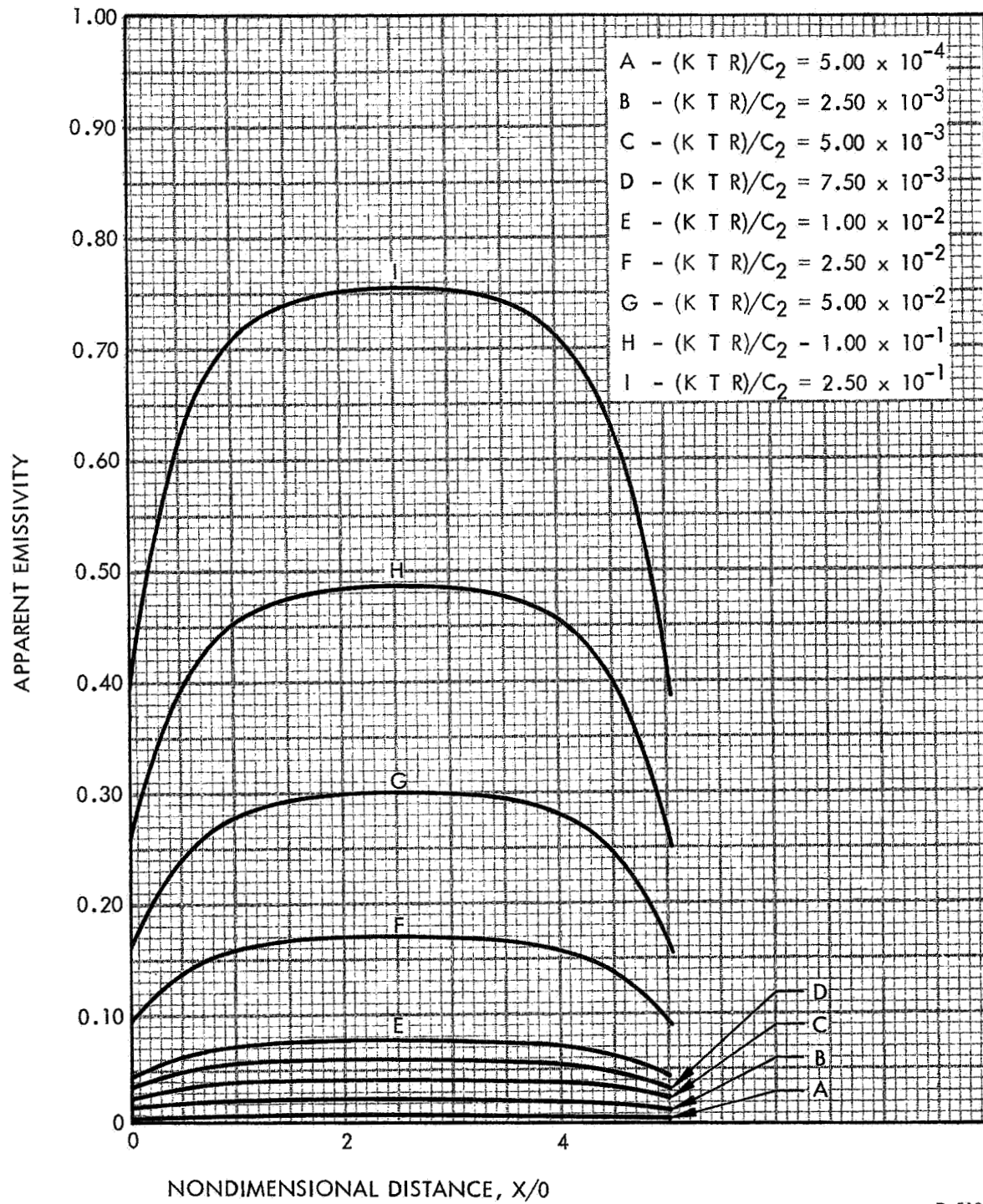
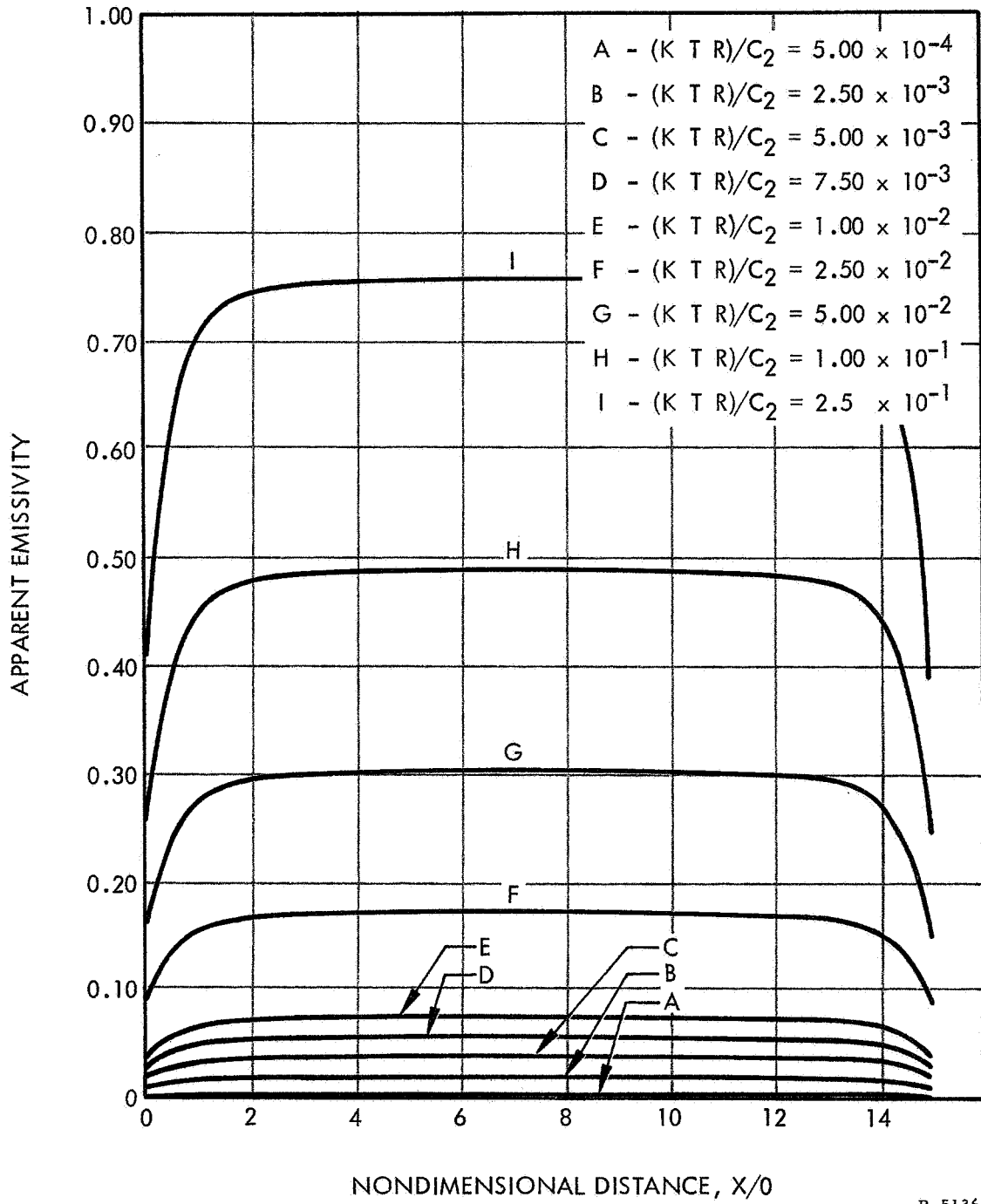Figure B-4. Apparent Emissivity for L/D = 5

Figure B-5. Apparent Emissivity for L/D = 10

R-51366

Figure B-6. Apparent Emissivity for L/D = 12

Figure B-7. Apparent Emissivity for L/D = 15

with $\quad D = 1 \text{ ft} = S$

$\quad\quad\quad p_c = 3 \text{ atm}$

$\quad\quad\quad p \cdot S = 0.3 \text{ atm-ft.}$

The emissivity of water is found in figure 4-15 of reference 2. This table only extends to $T_g = 5000°$ R. Extrapolating to $6000°$ R $\epsilon_{H_2O} \cong 0.02$ as compared to $\epsilon = 0.165$ (figure 4, $KTr = 2.5 \times 10^{-2}$). The typical concentrations of carbon dioxide are 2 to 3%. Hence, the water and carbon dioxide band emissions, although strong within their absorption bands, may be neglected when integrated over all wave lengths and compared to the continuum radiation of the particles.

The validity of the results lies mainly in the validity of the assumption that $a_\lambda = K/\lambda$. Until experimental confirmation of this is obtained, the presented results should be considered as approximate but useful in considering the relative importance of radiation to the ignition process.

Higher values of KTr, corresponding say to higher chamber pressures, are presented since such information is useful for internal insulation analysis during the steady combustion of the solid rocket.

6.0 REFERENCES

1. Love, E. S., and C. E. Grigsby, "Some Studies of Axisymmetric Free Jets Exhausting from Sonic and Supersonic Nozzles into Still Air and into Supersonic Streams," NACA RM L54L31. National Advisory Committee on Aeronautics, May 10, 1955.

2. McAdams, W. H., Heat Transmission. New York: McGraw-Hill, 1954.

3. Eckert, E. R. G., and R. M. Drake, Heat and Mass Transfer. New York: McGraw-Hill, 1959.

4. "Radiation Heat Transfer from Rocket Exhuast," Quarterly Reports No. 1 and 2, Contract NAS 8-11438. United Technology Center, 1964 and 1965.

5. "Results of a Measurement of the Emissivity and Temperature of the Combustion Products in the Throat of a TM-3 End-Burning Motor," Technical Memorandum TM-33-61-U1. United Technology Center, 9 June 1961.

APPENDIX C

MODIFICATION OF UNITED TECHNOLOGY CENTER'S
ONE-DIMENSIONAL AXISYMMETRIC HEAT CONDUCTION PROGRAM
FOR INTERACTION TO OBTAIN HEAT TRANSFER
FROM MEASURED TEMPERATURES

To obtain the transient heat flux at the surface of a conducting wall from temperature measurements a conduction analysis is required. United Technology Center has an operational heat conduction program which uses the implicit ("backward time difference") technique. The program solves the transient, one-dimensional heat conduction equation (in cylindrical coordinates) by the method of finite differences.* The modified program uses the measured temperature and an iterative process to determine the heat flux rates. This process is described below.

A. After the measured temperature versus time curve is read into the program, an initial estimate of heat flux versus time step is calculated by:

$$q = \left(\frac{p}{C_{max}}\right) \left(\frac{\Delta T}{\Delta t}\right) \rho \, C_p \, \Delta R$$

where

q = heat flux rate per unit area

p = pressure at any time t

p_{max} = maximum duct pressure during the firing

$\Delta T / \Delta t$ = maximum slope along the measured temperature-time curve

ρ = density of tube material

c_p = specific heat of tube material

ΔR = wall thickness of tube.

The ratio p/p_{max} is used only to adjust the initial approximations of q.

B. Using the heat flux rates, the program calculates a temperature profile through the wall. An insulated external surface is assumed.

---

*Kennedy, W. S., "A One-Dimensional Axisymmetric, Transient Heat Conduction Solution by Finite Differences," Technical Memorandum TM-14-62-U13. United Technology Center, April 1962.

C. The temperature "error" (ΔT) between the calculated and measured backside temperatures is determined for each time step.

D. The program then attempts to reduce the ΔT values to zero by adjusting the heat transfer rates. These adjustments involve the following procedure.

1. Figure C-1 illustrates a portion of measured and calculated temperature histories at the outside tube surface. Internal heat flux rates must be adjusted to force the temperature differences (ΔTs) towards zero. One should realize that the temperature difference, ΔT [N], is a cumulation of all temperature errors up to time t [N]. Consequently, the heat flux rate at time t [N] should be adjusted in accordance with the increase in error caused by going from time t [N-1] to t [N].
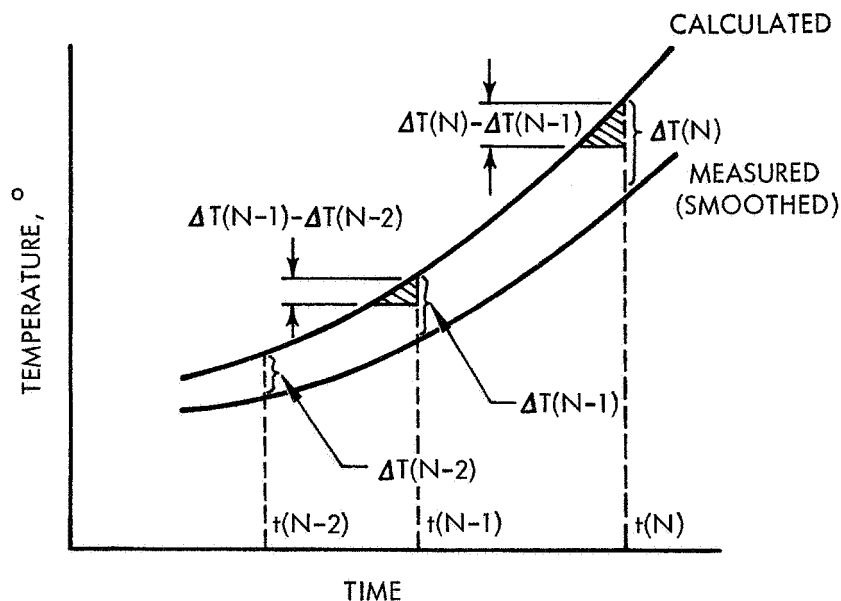
R-51361

Figure C-1. Measured and Calculated Temperature History
at the Outside Tube Surface

Consequently, the computer program adjusts q at each time step by:

$$q = q_{\text{prev. iter.}} - \rho \, c_p \, \Delta R \, \frac{\Delta T[N] - \Delta T[N-1]}{t[N] - t[N-1]} \, .$$

The term ΔT is positive for a calculated temperature at $t[N]$ greater than measured temperature. The above equation alters q to eliminate only that increase in temperature difference caused by going from time $t[N-1]$ to $t[N]$. Since the area under the curve is proportional to heat flux, each shaded area represents the adjustment on the value of q for that time step.

It should be noted that the equation uses temperature differences at the outside surface to calculate heat flux rates at the inner surface. Actually, inside surface temperature differences should be used to calculate the new q's, but this is not possible since no temperature measurements were made in this area. However, the iterative process eliminates inaccuracies caused by this equation. Section 2 contains a brief discussion on the use of the outside temperature differences.

2. Figure C-2 represents various temperature profiles through the tube wall. Even though ΔT_{1_i} and ΔT_{2_i} are somewhat greater than ΔT_{1_o} and ΔT_{2_o}, the difference between each set of profiles remains roughly constant throughout the wall. For the iterative process in the program, it is reasonable to assume that $\Delta T_i = \Delta T_o$.

E. Using the new heat transfer rates, the program calculates a new temperature profile and repeats steps C through E. Steps B through D are repeated until the difference between measured and calculated temperatures is less than $1°$ F for each time step.

The method described above was used instead of a "closed-form solution* since UTC already had the operational heat conduction program available. Only minor modifications were necessary to adapt this program to perform the aforementioned operations.

---

*Deverall, L. I., and R. S. Channapragada, "A New Integral Equation for Heat Flux in Inverse Heat Conduction."
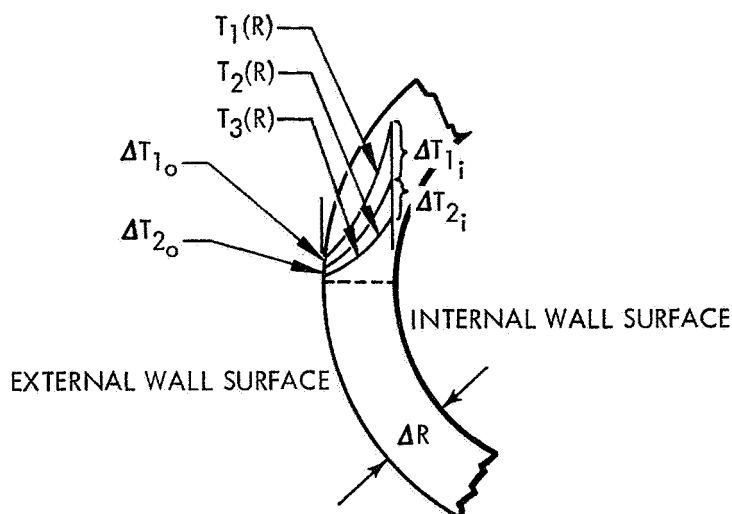
R-51362

Figure C-2. Temperature Profile in Duct Wall at Several Times

Any method of deducing the heat flux and surface temperature based on measured "backside" temperatures requires that the measured temperature curve be smooth and have a continuous derivative. The reduced temperature data were not always in such a form. Consequently, a "curve-smoothing" routine was used on the digitized data to prepare the curves for use in the heat conduction program. This routine is described in section 2.0 of appendix B. The resulting smoothed curves are a better representation of the oscillograph record than the reduced but uncorrected data.